School of Physics and Astronomy

Structure of and Light Emission in Matrix-Free Germanium Quantum Dots

William Robert Little
Supervisor: Dr. A. Sapelkin

Submitted in partial fulfilment of the requirements of the Degree of Doctor of Philosophy

Statement of Originality

I, William Little, confirm that the research included within this thesis is my own work or that where it has been carried out in collaboration with, or supported by others, that this is duly acknowledged below and my contribution indicated. Previously published material is also acknowledged below.

I attest that I have exercised reasonable care to ensure that the work is original, and does not to the best of my knowledge break any UK law, infringe any third party's copyright or other Intellectual Property Right, or contain any confidential material.

I accept that the College has the right to use plagiarism detection software to check the electronic version of the thesis.

I confirm that this thesis has not been previously submitted for the award of a degree by this or any other university.

Signature:

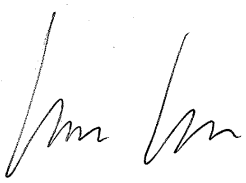

Date: 25/09/2014

Publications

1. A. Karatutlu, W. Little, A. V. Sapelkin, A. Dent, F. G. Mosselmans, G. Cibin, and R. Taylor, OD-XAS and EXAFS: Structure and Luminescence in Ge Quantum Dots, *J. Phys. Conf. Ser*, 430, 1-6, **2013**.

2. W. Little, A. Karatutlu, D. Bolmatov, K. Trachenko, A. V. Sapelkin, G. Cibin, R. Taylor, F. G. Mosselmans, A. Dent, and G. Mountjoy, Structural Origin of Light Emission in Germanium Quantum Dots, *Scientific Reports*, 4, 7372, 2014.

3. Y. Zhang, A. Karatutlu, O. Ersoy, W. Little, A. Sapelkin, G. Cibin, and A, Dent, Structure and Effects of Annealing in Colloidal Matrix-Free Ge Quantum Dots *Journal of Synchrotron Radiation*, 22:1, 105, 2015.

Abstract

The connection between light emission and structure of Germanium nanoparticles (3-10 nm) prepared by top-down (etching) and bottom-up (sol-gel and colloidal synthesis) has been investigated using Raman spectroscopy, TEM, x-ray absorption spectroscopy (XAS), x-ray diffraction (XRD), and photoluminescence (PL). It was found that TEM, Raman spectroscopy, PL, and XRD techniques all result in differing values for the nanoparticle size which don't all agree in the limit of experimental error. Several structural models have been proposed and tested by high pressure Raman measurements. It was found that a Raman peak corresponding to diamond-type Ge structure is observed well above the transition pressure of both amorphous ($\approx$ six GPa) and crystalline ($\approx$ 11 GPa) Ge. The pressure dependence of the Raman signal peak position was observed to follow an unexpected non-linear shift with a corresponding increase in peak width (FWHM). Possible structural origins of these trends have been investigated by adapting the widely used phonon confinement model to high pressure conditions and comparing experimental data with the model behaviour under assumptions of constant, and size-dependent bulk modulus. Considered collectively with the ambient structural data, the results of the analysis of the high pressure behaviour point to the phenomenon of gradual surface induced amorphisation under pressure in matrix-free Ge nanoparticles. The best structural model to describe this is a core-shell with the small crystalline core and a disordered surface layer.

The local structure of samples was investigated using XAS, while optically-detected XAS, using x-ray excited optical luminescence (XEOL), was used to link structure with optical emission. The emission was found to depend on surface termination; in oxygen terminated nanoparticles the oxide rich regions are responsi-

ble for light emission, while in their hydrogen terminated counterparts' pure Ge regions contribute to the luminescence. Furthermore, with the aid of molecular dynamics simulations it was shown that in hydrogen-terminated samples, optical emission is due to a topologically disordered (amorphous) region close to the surface of the nanoparticles. We demonstrated that OD-XAS can potentially provide sub-nanoparticle resolution due to its sensitivity to the light emitting sites in a sample. We further investigated the microscopic origins of such sensitivity and identified possible limitations.

This work clearly demonstrates that a combination of methods sensitive to short-range and long-range structure are required for comprehensive characterisation of nanoscale systems.

Acknowledgements

I would like to thank my supervisor Dr. Andrei V. Sapelkin for his help and instruction over the years. Thanks are also extended to Dr. Gavin Mountjoy, my secondary supervisor.

My appreciation goes to Ali Karatutlu, Osman Ersoy, Mingying Song, Yuanpeng Zhang, and Kemal Keseroglu, my fellow students under Dr. Sapelkin. Many experiments were performed cooperatively, along with many fruitful discussions.

I would also like to thank Giannantonio Cibin, Richard Taylor, Fred Mosselmans and Andrew Dent, from Diamond Light Source, RAL. Their involvement was instrumental in obtaining all x-ray experimental results.

This work was supported by South East Physics Network (SEPnet) PhD studentship jointly awarded to Queen Mary University of London and University of Kent

Contents

List of Figures

List of Tables

Abbreviations

EMFP	electron mean free path
eV	electron volts
EXAFS	extended absorption fine structure
FWHM	full width half maximum
Ge	germanium
LO	longitudinal optical
MES	Murnaghan equation of state
OD-EXAFS	optically detected extended absorption fine structure
OD-XAS	optically detected x-ray absorption spectroscopy
PL	photoluminescence
PLE	photoluminescence excitation
QD	quantum dot
RWL	Richter-Wang-Ley
Si	silicon
TEM	transmission electron microscopy
XANES	x-ray absorption near edge structure
XAS	x-ray absorption spectroscopy
XEOL	x-ray excited optical luminescence
XRD	x-ray diffraction

Chapter 1

Introduction

1.1 Photoluminescence in Semiconductor Nanoparticles

Potters and ceramists have been using nanoscience unwittingly for hundreds of years when making Luster, a 200 - 500 nm film to produce glazed pottery, as in figure 1.1. Luster is a silicon rich matrix containing spherical metallic crystalline nanoparticles. The matrix has a glassy outer surface layer, devoid of nanoparticles, 10 - 20 nm thick [1]. This was valued for its characteristic shine, which was a result of the optical properties of nanostructures. Nanoparticles also found extensive unwitting use in stained glass windows, such as the one pictured in figure 1.2. Gold nanoparticles are responsible for the rich ruby colour, while silver nanoparticles produce the yellow colouration. A similar effect is observed in the Lycurgus Cup, a cup made of dichroic glass in the 4th century. The glass contains gold and silver nanoparticles dispersed throughout it, and appears red when lit from behind and green when lit from the

Figure 1.1: A cup with lustre decoration dating from 11-12th century Egypt. Metallic nanoparticles are responsible for the characteristic shine [8].

front [2].

However, until recently the origin of these optical properties has not been studied in detail. In the last several decades nanoscale materials with particular and peculiar optical properties have been used and investigated much more deliberately and systematically. Studying the optical and electronic properties of nanoscale materials presents an opportunity not only to develop understanding in terms of fundamental physics, but promises to result in incredibly useful and unprecedented real word applications. Nanoscale materials have the potential to be applied to technologies as diverse as nanowire field effect transistors [3], lasers [4], light emitting diodes [5], chemical sensors, [6], and logic gate circuits [7], among others.

Many of these potentialities lie with nanoscale semiconductor quantum dots, and as such a great deal of interest has been focused on them in recent years. Nanoscale semiconductors have the potential to be applied to technologies as diverse as optical computing or imaging and diagnostic devices in biomedicine. For

Figure 1.2: A stained glass window in All Saints' Church in Daresbury, featuring characters from Alice in Wonderland. Gold nanoparticles suspended in the glass create the ruby colour, while silver nanoparticles are responsible for the yellow [9].

instance, their electrical properties lend themselves towards improving and augmenting lithium batteries [10] and solar cells [11]. The mechanical properties of nanomaterials also hold promise for applications such as cutting tools, wear-resistant coatings, and structural nanocomposites [12]. Additionally their reactivity shows promise for implementation in nanosensors [13] and catalysts [14].

The use of nanoparticles in biological imaging, where they have several clear advantages over other standard techniques, is a particularly promising application. Most common fluorescent imaging techniques rely on photoluminescent dyes [15, 16]. These dyes can be targeted by using chemical labels, but they have a limited lifespan of seconds to minutes before degrading and ceasing to luminescence, thus limiting the types of phenomena that can be studied [17]. Dyes rely on structural changes as part of the mechanism for their optical activity and as a result suffer from photobleaching, which is what limits their applications primarily to short term experiments [17]. Semiconductor quantum dots do not suffer from photobleaching as

their photoluminescent activity is completely due to electronic transitions and does not involve a change in structure. A further advantage of nanoparticles over dyes is the versatility of their emission wavelength. Dyes emit at a single wavelength and so for each required colour, a new dye is needed. Different colour dyes are completely different molecules and as such will have different properties, such as stability, efficiency, toxicity, lifetime, etc.

The emission wavelength in nanoparticles, however, can be controlled by size alone. This is due to the relationship between the nanoparticle size and its band gap, as nanoparticle size is reduced the band gap widens, as shown in figure 1.3. This extends to a simple relationship between size and emission wavelength, the smaller the particle the shorter the wavelength, as illustrated in figure 1.4. This relationship has already been very useful in the preparation of CdSe nanoparticles [18, 19, 20].

For semiconductors the size dependence of the band gap can generally be understood in terms of the quantum confinement effect - a condition where the geometric size decisively affects a variety of physical parameters [23, 24, 25]. The concept is elegant, but not easy to probe directly in many cases due to the difficulties in observing quantum dots (QDs) in an idealised state that can be readily compared with a corresponding theoretical or a computational model. A good example of this is porous nanocrystalline silicon (Si), the unusual optical properties of which were discovered in 1990 by Canham [26, 27]. The intense visible photoluminescence (PL) they observed was originally attributed to the quantum confinement effect, but almost immediately an alternative explanation was presented [28, 29, 30, 31] suggesting the PL was due to surface states, recombination at the surface, or Si compounds of a molecular nature on the surface. Over two decades of intense

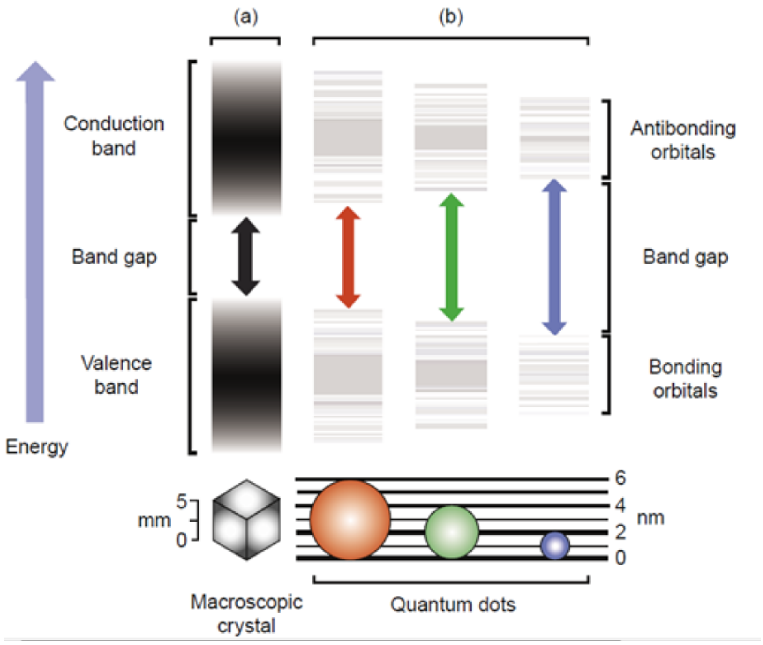

Figure 1.3: Nanoparticles band gap is dependent on its size. a) For bulk scale materials the band gap remains unchanged. b) For nanoscale materials as size is reduced the band gap widens, shifting the emission wavelength to higher energies. [21]

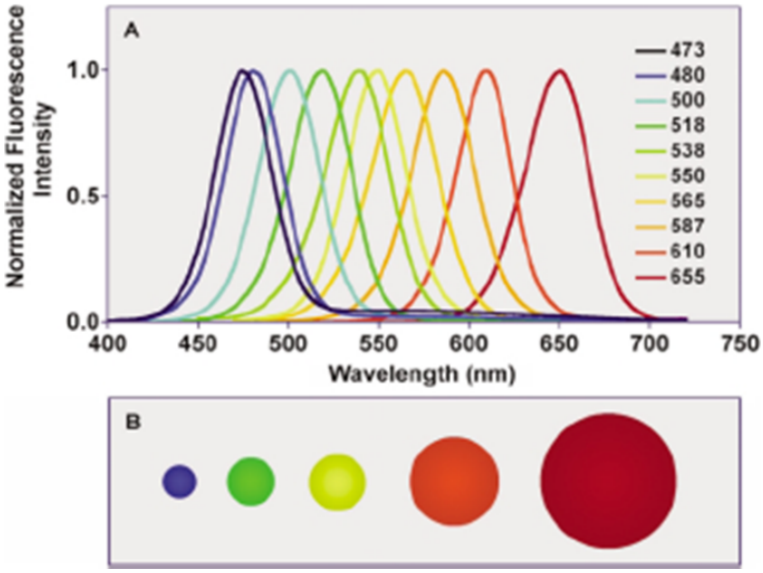

Figure 1.4: The emission wavelength of nanoparticles is dependent on their size. The smaller the nanoparticle the shorter the wavelength and higher the energy. From left to right, the particle diameters are 2.1 nm, 2.5 nm, 2.9 nm, 4.7 nm, and 7.5 nm. [22].

research that followed could not provide unequivocal evidence and eventually led to the development of a model of Si QDs that includes core, surface, and interfacial regions [32]. The recent contributions to the discussion includes rather complex PL measurements on single Si QDs in a silicon oxide environment [31], in magnetic fields [33] and under pressure [34]. Crucially, none of the approaches so far have been able to provide *direct* evidence of a connection between the light emission and the underlying atomic structure. It seems that the research into germanium (Ge) QDs is suffering from a similar fate. Several preparation routes for Ge QDs have been reported [35, 36, 37, 38] and PL was observed in the region between 400 nm and 1000 nm. The exact origins of the observed PL are yet to be established with some reports suggesting significant influence of surface effects [39].

Ge is a close structural and electronic analogue to Si and there has been significant interest in understanding the optical properties of Ge QDs [40, 41, 42]. The vast majority of early studies looked at embedded Ge QDs due to limited success in preparing free-standing samples with controlled surface termination. It has been established [42, 43] that in most cases, PL observed in embedded Ge QDs can be attributed to oxide related species, rather than pure Ge. The presence of oxides is mostly related to the preparation techniques (e.g. implantation into an oxide [44], using Ge oxides as a precursor [45], etc.). Recently, a comprehensive x-ray absorption spectroscopy (XAS) study has been conducted [46] of nano-size effect on the structural properties of Ge QDs embedded in a silica matrix which suggests the formation of a disordered region between a nano-crystalline core and silica matrix. Again, the role of the matrix in the formation of these regions and the effect of the matrix on the optical properties of embedded Ge QDs is unclear. Only recent advances in colloidal synthesis [47] have provided access to free-standing Ge QDs.

However, the main challenge in establishing a *direct* link between the atomic structure and optical emission still remains. The work conducted by our group over the last several years [48] has resulted in samples which do not show significant evidence of Ge-based oxides as characterised by Raman spectroscopy and energy dispersive x-ray spectroscopy (EDX) analysis while Fourier transform infrared (FTIR)/Raman data [49] show the presence of Ge hydroxide/hydride species. These synthesis methods provide access to matrix-free Ge QDs with hydrogen and oxygen terminated surfaces and are very promising model systems to study the complex nature of size effects.

Given the unusual nature and complex behaviour of these nanoparticles, and the sensitivity of the electronic (and therefore optical) properties to small changes in structure and morphology, it is difficult to characterise any particular sample of nanoparticles using a single technique. This has been demonstrated in the study of Si nanoparticles outlined above [26, 27, 28, 29, 30, 31, 32], where a good understanding of the sample was not obtained until all the data had been combined. Here we aim to perform a variety of investigative techniques to determine the nature of our samples, and demonstrate which techniques are required to achieve that goal. The particular suite of techniques adopted for this thesis were chosen to target the key structural information (i.e. long and short range order) and link it to the electronic and optical properties.

When studying nanoparticles transmission electron microscopy (TEM) is a necessity as the direct nature of the technique gives definitive proof of the scale of the nanoparticles, and determines the upper limit which can be used to check the validity of other techniques which provide size information. High resolution TEM and electron diffraction could hypothetically extract detailed structural information,

but these techniques are known to damage samples via annealing, particularly in nanoparticles, and so cannot be relied upon. However, x-ray diffraction (XRD) is a non-invasive technique which results in no damage to the sample. It is sensitive to long range order and can be used to determine the extent of crystalline structures within the nanoparticles. XRD does have a lower limit for identifying nanoparticles as below 0.8 nm the width of the peak will be equivalent to one of an amorphous sample (10° [50]). XAS is also a non invasive technique which probes the short range structure by examining the local structure around a particular species. Optically detected x-ray absorption spectroscopy (OD-XAS), a variant of XAS, can be used to probe the local environment of the photoluminescent species. What qualifies as the local environment is hard to define, but is usually considered to be the first few nearest neighbours. Raman spectroscopy is also an obvious candidate as it is a quick and easy way of probing the structure to determine if a sample is crystalline or amorphous. Further, a model describing how the Raman spectrum is affected by particle size at such small scales has already been developed and is readily implemented [5]. This method also has a lower size limit, generally taken to be 2.2 nm [51]. This limit comes from assumptions made during the formulation of the model. Finally, high pressure Raman spectroscopy can be used to reveal the contributions from different structural subsections as they undergo phase transitions at different pressures.

Thus in this thesis experimental techniques sensitive to short and long range order were combined to determine the structure of matrix-free Ge nanoparticles. We demonstrate that the most appropriate model for Ge nanoparticles is a core-shell structure, with a crystalline core and disordered surface layer. We show that the light emission from matrix-free Ge nanoparticles is crucially dependent on surface

termination; disordered Ge regions are responsible for the light emission in hydrogen terminated samples, while Ge oxide regions contribute to the light emission in oxide terminated samples.

Before the origin of light emission from oxygen and hydrogen terminated Ge nanoparticles can be demonstrated it is necessary to understand the fundamental properties of the material in question. The next section contains details of the structural and electronic properties of Ge which will lay the basis for the work that follows.

1.2 Structural and Electronic Properties of Ge

Ge atoms, like C and Si, have four valence electrons available for bonding. Under ambient conditions the crystal structure formed by such elements is a face centred cubic (FCC) diamond type structure. The unit cell of the diamond cubic crystal structure is shown in figure 1.5. Each atom has four nearest neighbours and is tetrahedrally coordinated [52]. Selected physical properties of Ge are given in table 1.1.

Physical Property	Value in Crystalline Ge
Band Gap (electron volts (eV))	0.664
Bond Length (Å)	2.45
Bulk Modulus (GPa)	74
Lattice Constant (Å)	5.658

Table 1.1: Physical parameters for bulk crystalline Ge.

In Ge the cubic diamond structure and the interatomic interactions (namely covalent bonding) leads to a phonon dispersion as in figure 1.6. The presence of optical phonons with a non-zero frequency for a zero value wave vector is what

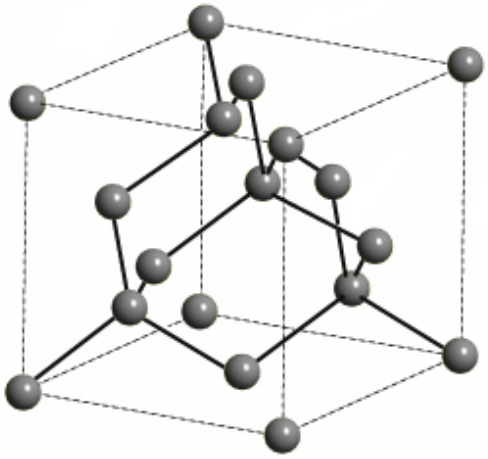

Figure 1.5: The unit cell of a diamond type crystal cubic structure. This is the structure of diamond, as well as crystalline Si and Ge, which are structural analogues. Modified from [53]

allows Raman spectroscopy to be performed. Another consequence of the diamond like structure and covalent bonding is the electronic band structure depicted in figure 1.7. The lowest point in the upper band and the highest point in the lower band (their difference of 0.66 eV is labelled E_g) lie at different values of the wave vector. Thus Ge, like Si, is said to have an indirect band gap. The indirect band gap is a potential problem for any applications which involve light absorption or emission. For radiative recombination in an indirect band gap material a phonon is required to be either absorbed or emitted to satisfy conservation of momentum, making the process significantly less likely to occur than with a material that has a direct band gap, and limits their light emission efficiency. However there is evidence that this electronic structure is liable to change with size for small particles [54]. Further, there is evidence of $L \rightarrow X$ crossing for sufficiently small particles, such that the narrowest transition is from the X to Γ, rather than L to Γ [55]. Consequently, for particles where $L \rightarrow X$ crossing occurs the direct character of the band gap is increased, above even that of Si.

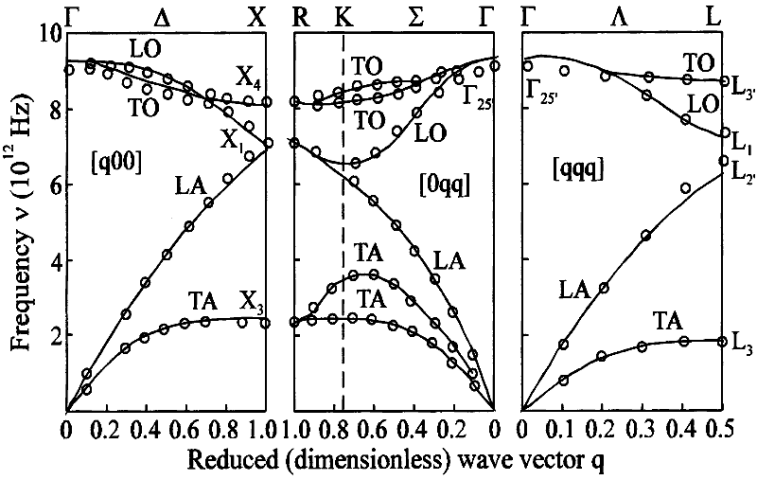

Figure 1.6: The phonon dispersion curve for diamond crystalline cubic structured bulk Ge. The optical phonon modes (LO and TO) with a non-zero frequency for a zero value of wave vector allow the sample to be probed with Raman spectroscopy [56].

However, discussing the direct character of the band structure becomes problematic in nanoparticles. While there are well developed theories for the electronic structure in both periodic crystal structures and in molecules, nanoparticles lie in a no-mans-land, being too small to be treated as a fully periodic crystal structure, and too large for a molecule. The lack of full periodicity also leads to the concept of the Brillouin zone no longer being applicable and the k vector is no longer a good quantum number, leading to a breakdown in the k-selection rules. Ultimately there is as yet no analytical theory that can accurately describe the electronic structure of these nanoparticles and so approximations become a necessity. One such approximation involves the well-known concept of effective mass. The concept of the effective mass is a key approximation used in the quantum confinement model (discussed in section 3.1).

Besides the effect on the electronic properties, the size reduction may also affect the structural stability of nanoparticles resulting in the formation of metastable

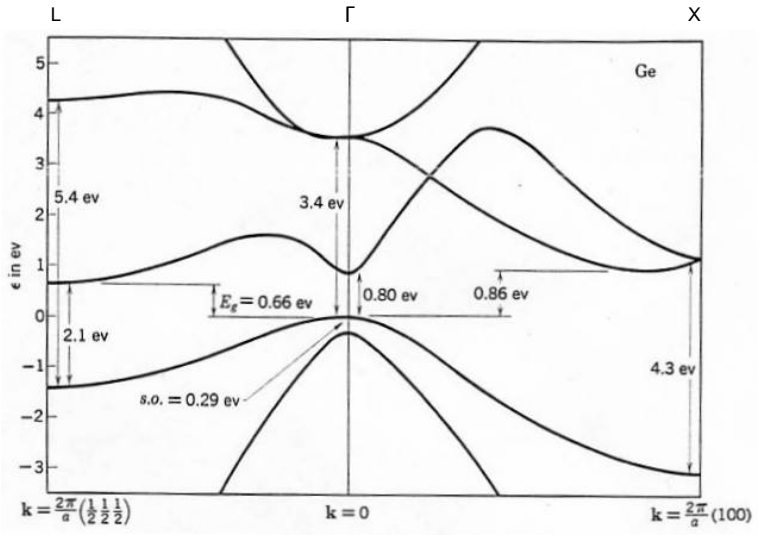

Figure 1.7: The electronic band structure of diamond crystalline cubic structured bulk Ge. The lowest point of the valence band and the highest point in the conduction band lie at different wave vectors resulting in an indirect band gap. Modified from [57].

phases [58, 59, 60, 61] . While Ge can form diamond type crystalline structures, and a glassy amorphous structure, a variety of metastable phases have also been observed during nanoindentation experiments [62] or have been predicted by modelling [63]. A variety of allotropes of Ge can be formed via the application of pressure and temperature ($\sim$ 10 GPa and $\sim$470 K respectively) which have dramatically different electronic properties from one another. For instance, a body centred cubic structure known as BC-8 is formed when pressure is released rapidly, while a tetragonal structure known as ST-12 is formed under slow depressurisation. ST12 Ge has a band gap of approximately 1.47 eV [60], while BC-8 has a semi-metallic band structure, with the conduction band penetrating below the valence band [64].

The bulk modulus characterises the volume change of a sample when subjected to hydrostatic pressure. This is appropriate for the initial structure of the sample, but is no longer applicable once the applied pressure is high enough to have

caused a first-order phase transition. These transitions cause dramatic changes in the electronic, optical, and vibrational properties of the material. For example Ge undergoes a transition from a diamond type structure to β-tin at 10-11 GPa, at which point both Raman and PL signals are lost. This effect has recently been used to study the origin of light emission in Si nanoparticles by determining if the emission was from surface layers or the core, exploiting the fact that the surface layer has different transition pressures to the core [34].

A transition from semiconductor phase to a metallic phase will change the PL and Raman properties to be almost unrecognisable. Different structural phases of the same material often have different transition pressures, for instance the amorphous phase and crystalline phase will transform at different pressures.

Recent work seems to suggest that the bulk modulus also changes when the scale of the sample is reduced to the nanometre range. Computer simulations have found the bulk modulus of 1.5 nm particles to be 84 GPa [65], and experiments found a value as high as 112 GPa for 13 nm nanoparticles [66]. A key difficulty in getting reliable values for the bulk modulus for a range of sizes is the lack of experimental data for very small matrix-free nanoparticles that can be compared to simulations. The discrepancy between these two results means that any fitting of data performed with pressure effects in mind will have to be performed for a range of values of the bulk modulus to investigate if a value of the bulk modulus different to that of the bulk is responsible for any observed behaviour.

As previously mentioned the electronic structure is liable to change with size for small particles. In the next section the effect of reduced size on the electronic properties of semiconductors will be briefly examined.

1.3 Quantum Confinement in Small Structures

Nanoscale semiconductors can be grouped according to the number of dimensions that are restricted to the nanoscale. Having two dimensions unrestricted results in thin films. There is one unrestricted dimension in nanorods and nanowires, and zero unrestricted dimensions in nanoparticles, or quantum dots. This restriction results in varying effects on the electronic structure and optical properties compared to the bulk. The exact details of the effects are dependent on the size of the confined region and the number of restricted dimensions. In this thesis we are principally interested in investigating relationships between the optical and structural properties of the quantum dots. The optical properties are dependent on the electronic properties and the effect these have on electronic excitations and de-excitations. In turn, the electronic properties will depend on the structure, the nature of the bonding, the systems morphology, and its size. Thus the key parameter of interest is the exciton and how it is affected by the restriction of the physical size and therefore confinement. The size of an exciton in a semiconductor is given by

$$a_{ex} = \frac{a_B \epsilon}{m^*/m_e}, \tag{1.1}$$

where ϵ is the dielectric constant, m_e is the electron rest mass, and m^* is the reduced mass of the exciton given by $m^* = \frac{m_e^* \cdot m_h^*}{m_e^* + m_h^*}$ and m_e^* and m_h^* are the effective mass of the electron and hole respectively. The parameter a_B is the Bohr radius and is given by

$$a_B = \frac{4\pi\hbar^2\epsilon_0}{m_e e^2}, \tag{1.2}$$

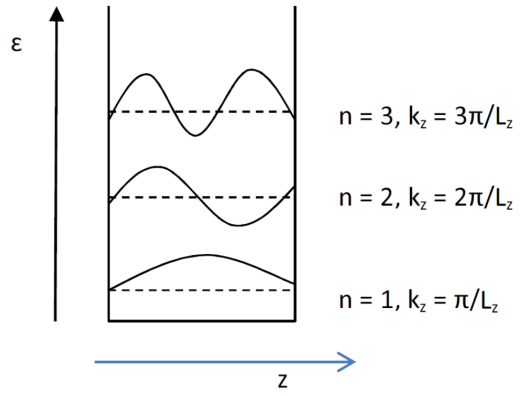

Figure 1.8: A particle in a box. Infinite potential walls result in a well within which only an integer number of half wavelengths are allowed, with the wavefuntion pinned to zero at the edges. L_z is the size of the structure in the restricted dimension.

where ϵ_0 is the permittivity of free space, $\hbar$ is the reduced Planck's constant, and e is the elementary charge. Once one or more of the dimensions of the sample is of the order of the exciton Bohr radius, the sample is said to be subject to quantum confinement. This behaviour is referred to as quantum confinement because the dimensional restrictions drives the exciton to exhibit quantised characteristics. This can be qualitatively understood when the exciton is considered to be a particle in a box. To a first approximation the edges of the sample are an infinite potential barrier and so the structure is effectively a potential well, as in figure 1.8. This also makes the simplifying assumption that the exciton moves within a constant potential within the structure.

As can be seen in figure 1.8, the infinite potential barrier at the edges of the structure impose a boundary condition that the electron wavefunction must be zero at the edges. Consequently there must be an integer number of half wavelengths of the wavefunction within the structure. This limits the possible wave vectors in the restricted dimension to

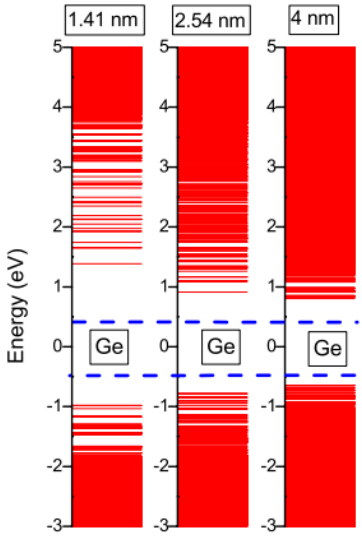

Figure 1.9: The size dependence of the band gap in Ge nanoparticles. As the size is reduced the band gap widens. The blue dotted lines indicate the band gap in bulk Ge [67]

$$k_z = \frac{n\pi}{L_z}, \tag{1.3}$$

where n is an integer and L_z is the length of that dimension. For a nanoparticle where all three dimensions are restricted the kinetic energy is given by

$$E_{nlm} = \frac{(\hbar\pi)^2}{2m^*}\left(\frac{n^2}{L_z^2} + \frac{l^2}{L_y^2} + \frac{m^2}{L_x^2}\right), \tag{1.4}$$

where n, l, and m are integers. This size dependence is what causes the increase in the band gap seen in figure 1.9 for Ge. As the particle gets smaller, the well gets narrower, the energy levels get higher and spread further apart. Figure 1.10 shows how features of the bulk band structure are related to the electronic structure of nanoparticles (therein referred to as clusters).

Figure 1.11 shows the consequences of the confinement effect in real nanopar-

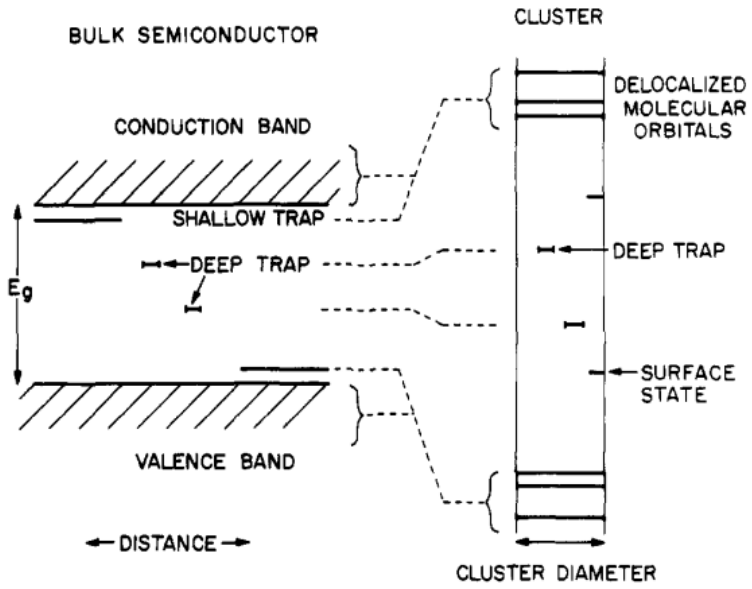

Figure 1.10: Correlating features of the bulk band gap to that of nanoparticles [68].

ticles. The black lines showing Ge and the dotted line Si. For both materials the reduction in size of the nanoparticles leads to a non-linear shift in the band gap. The interesting feature of the graph in figure 1.11 is that the lines for Si and Ge cross, showing that the rate of change of the band gap in terms of size is greater for Ge than Si. The difference in the rate of change of band gap energies with respect to size is a result of their differing exciton Bohr radii. While quantum confinement effects are only observed when the dimensions of the structure is comparable to the exciton Bohr radius, the degree of confinement is greater the further the particle size descends beyond this limit. For Si the exciton Bohr radius is 4.9 nm and for Ge it is 24.3 nm, so for particles between $1 - 3.5$ nm Ge experiences a much stronger confinement effect.

The effect of quantum confinement can result in an increase in the efficiency of light emission in nanoparticles. This is particularly true for indirect band gap semiconductors such as Si and Ge. For Si the bulk has a quantum yield of a few

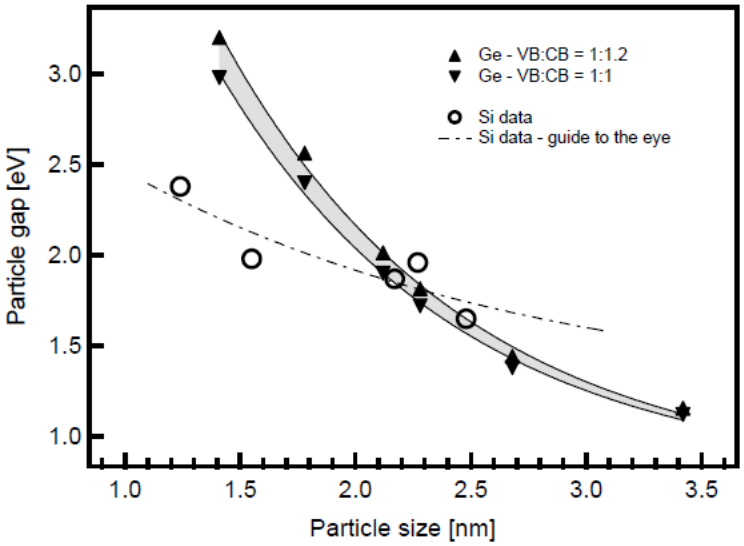

Figure 1.11: The particle size dependence of the band gap for Si and Ge. Figure reproduced from [70], where the Ge data is reported. The Si data is from [71].

fractions of a percent, but the nanoscale equivalent routinely has an efficiency in the tens of percent, and recently as high as 60% [69]. To the author's knowledge an equivalent study for Ge does not exist. However, considering the structural and electronic similarities it has with Si and the visually observed PL intensity, it is reasonable to conclude that there is indeed a similar phenomena for Ge.

Due to the relatively large exciton Bohr radius of Ge the behaviour of strongly confined nanoparticles can be probed without requiring the production of nanoparticles on the scale of angstroms.

The following chapter details the techniques used to analyse the samples. A combination of direct and indirect methods are used to get a thorough knowledge of the the samples' structure and properties.

Chapter 2

Experimental Methods

2.1 Raman Spectroscopy

The mechanism for the inelastic scattering of light was predicted in 1923 by Adolf Smekal [72]. The phenomenon was later observed in practice in 1928 by Sir C. V. Raman and K. S. Krishnan, and independently by G. Landsberg and L. Mandelstam [73]. While the phenomenon is named after Sir C. V. Raman, Landsberg and Mandelstam made their observations a week before Raman and Krishnan, but did not publish their findings until some months after Raman. Raman made his observations using a narrow band photographic filter to create monochromatic light from sunlight. Then, using a "crossed filter" to block the monochromatic light, he found that a small amount of light had changed frequency and so was able to pass through the filter, demonstrating that it had indeed been inelastically scattered. Raman won the Nobel Prize in Physics for this discovery in 1930. The advent of laser technology in the 1960's greatly simplified the technique and significantly improved its

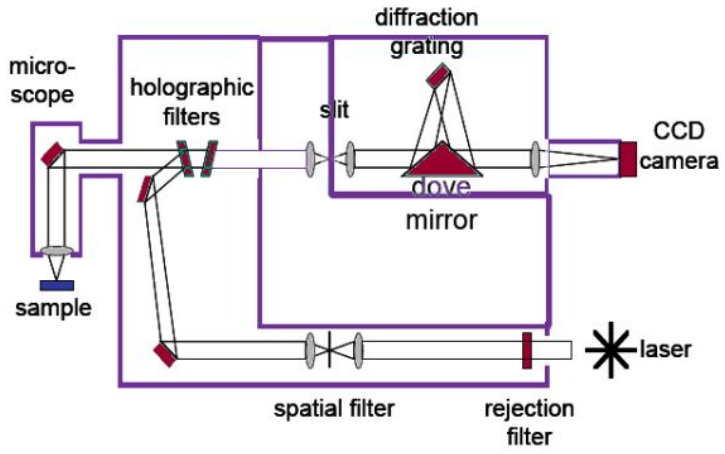

Figure 2.1: A schematic of a Raman set up. Columnated laser light is directed to the sample via a microscope. Light scattered from the sample is then directed through the optics of the system and recorded on a CCD. [74].

sensitivity and output, turning it into the standard method it is today.

Raman spectroscopy is widely used to study the atomic structure of materials. It is based on inelastic scattering of light in a sample, the energy of the probing photons is transferred to (or from) a phonon. The phonon spectrum of a sample depends on the details of its atomic structure and interatomic interactions. Hence the Raman technique provides a quick and easy indirect method to test the structure of samples. A schematic of a Raman experimental set up is shown in figure 2.1. In the work of this thesis Raman experiments were conducted with a Renishaw spectroscopy system equipped with a 20× magnification long working distance objective and a 785 nm (1.58 eV) laser as the excitation source.

In the classical interpretation the Raman effect is viewed as the interaction of electromagnetic radiation ($E_0 \sin(2\pi\nu t)$, where ν is the frequency) with the electrons in the sample by creating dipoles [75]. The degree to which this occurs is dependent on the materials polarisability. The dipole oscillates with the incident

electromagnetic radiation and in turn emits its own. If the polarisability, α, of the sample varies with vibration then it can be expressed as

$$\alpha = \alpha_0 + \frac{d\alpha}{dq} \tag{2.1}$$

where α_0 is the polarisability in absence of vibrations, and q is a coordinate describing the molecular vibration [75]. The coordinate can be expressed as

$$q = q_0 \sin(2\pi\nu_m t), \tag{2.2}$$

where q_0 is the amplitude of the molecular vibration, and ν_m is the frequency [75]. By considering the oscillations induced by the incident electromagnetic radiation and the change in polarisability from oscillation, the dipole moment $P = \alpha E$ [75] can be written as

$$P = \alpha_0 E_0 \sin(2\pi\nu t) + \frac{1}{2}\frac{d\alpha}{dq} q_0 E_0 [\cos(2\pi(\nu - \nu_m)t) - cos(2\pi(\nu + \nu_m)t)]. \tag{2.3}$$

The emission has three distinct components, one at the frequency of the incident radiation, and two which vary from it by $\pm\nu_m$. These two signals constitute the observed Stokes and anti-Stokes scattering. The Raman cross section, σ_R, is inversely proportional to the incident wavelength, λ, [75] according to

$$\sigma_R \propto \frac{1}{\lambda^4}. \tag{2.4}$$

The Raman intensity is therefore very weak so a laser is required to maximise the

output.

While useful for understanding, the classical interpretation is not without its limits. For instance it includes no concept of phonon statistics and so cannot account for the difference in intensities of Stokes and anti-Stokes scattering. For a fuller understanding we turn to the quantum mechanical interpretation. This approach considers an incident photon to excite an atom in the sample to a virtual energy state which quickly decays resulting in the re-emission of a photon. The change in energy of the outgoing photon relative to the incident photon is a result of the creation or destruction of a phonon in the sample.

As shown in figure 2.2 there are two mechanisms by which a Raman signal is generated. One is by transfer of energy from the photon to the sample (Stokes scattering), and the other is by transfer of energy from the sample to the photon (anti-Stokes scattering). Stokes scattering generates the stronger signal, where the scattered photons are observed to shift to a lower wavenumber (longer wavelength) relative to the input beam, corresponding to their lowered energy. Anti-Stokes scattering is the weaker of the two, where the scattered photons being observed have a higher wavenumber than the input beam, corresponding to a higher energy. Anti-Stokes scattering is a weaker signal because it requires a phonon for the interaction, whereas Stokes scattering has no such requirement and so is more likely to occur. The intensity of the anti-Stokes signal is observed to increase with the temperature of the sample [76]. This is to be expected as an increased temperature means that there are an increased number of phonons in the lattice so the interaction becomes more likely.

A key factor in determining the details of the Raman signal is the dispersion

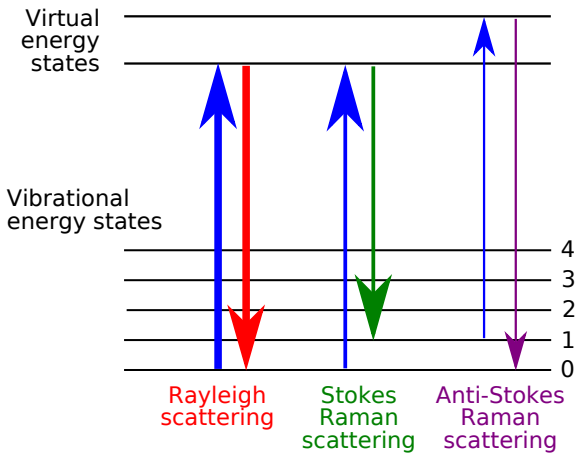

Figure 2.2: An energy level diagram showing the transitions and states involved in the Raman scattering process. In Stokes scattering energy is transferred to the lattice, creating a phonon. In anti-Stokes scattering energy is transferred from the lattice, destroying a phonon. The arrow thickness is approximately proportional to the signal strength. Modified from [77]

of phonons that can exist within the sample. Phonon dispersion is uniquely defined by atomic structure (symmetry) and by the nature of interatomic interactions. For instance bulk Si has a characteristic peak at 520 cm^{-1} whereas in bulk Ge the peak lies at 301 cm^{-1}, as shown in figure 2.3. Since the crystalline structure of Si and Ge are identical this difference is due to differences in bonding. The bond strength, bond length, and frequency of oscillation all have an effect on the observed wavenumber shift. This is what makes Raman spectroscopy a very useful tool for analysing materials as the spectrum is dependent on the species present and their state.

This can prove to be very useful for nanoparticles, as each type of structure has a characteristic peak that can be used like a fingerprint to identify a species. A typical example of this would be Ge nanoparticles that have a surface layer of hydrogen will display a stretching band at 1900-2000 cm^{-1} [43]. This can be useful to determine whether nanoparticles have been successfully passivated or have reacted

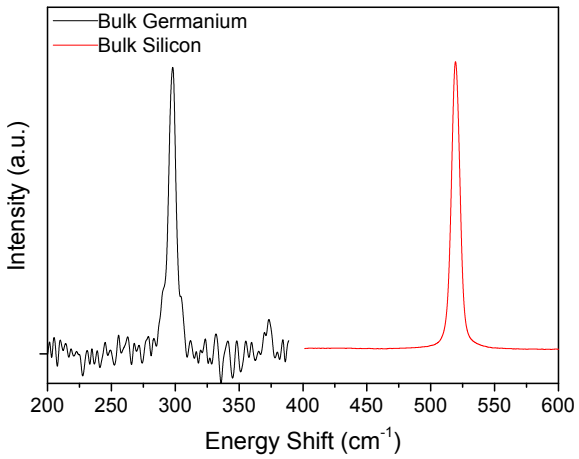

Figure 2.3: Raman spectra for bulk Ge (black) and bulk Si (red), with peaks at approximately 300 cm^{-1} and 520 cm^{-1}. The peak shape is a characteristic Voigt function, the convolution of the natural Lorentzian line broadening and the Gaussian broadening of the optics.

in some alternative or undesirable way.

Due to phonons having a comparatively low energy and high momentum, and photons having the reverse, phonons with a momentum and wave vector of approximately zero are probed. Phonons can have a wide range of momenta, given by

$$\hbar k = \frac{2\pi n}{Na}, \tag{2.5}$$

where N is the number of atoms in the system, a is the lattice spacing, and $n = 0, \pm 1, \pm 2, ..., \pm\frac{N}{2}$ (the upper bound is due to the minimum wavelength of $2a$). Photons, however, being immaterial, have a very low momentum, p, given by

$$p = \frac{h}{\lambda}, \tag{2.6}$$

where λ is the wavelength. As the outgoing photon must also have this momen-

tum, the momentum that can be transferred to the lattice is restricted to almost zero. Consequently only phonons with a momentum of almost zero can be probed. Conversely, energy suffers no such restriction. The energy of a photon, E_p, is given by

$$E_p = h\nu_p, \tag{2.7}$$

where ν_p, the photon frequency, is greater than the energy of a phonon, E_n given by

$$E_n = \left(\frac{1}{2} + n\right) h\nu_k, \tag{2.8}$$

where ν_k is the phonon frequency. This means that experiments aren't limited to probing the acoustic modes. Figure 2.4 shows an example of the phonon branches present in a crystalline lattice, the region of probed phonons indicated by the red oval. In this application of Raman spectroscopy it is the longitudinal optical (LO) branch that is probed.

The observed peak signal is not a delta function as might be expected given the phonons probed. The Raman peak is subject to a fundamental broadening effect as a result of the phonon lifetime giving it the natural lineshape of a Lorentzian. This signal undergoes further broadening due to the spectrometer collecting it which has a Gaussian transfer function. The observed Raman signal is a result of the convolution of both of these functions resulting in the characteristic shape of a Voigt function [7]. A typical Raman spectra is modelled in [79] by

$$I(\omega) = I_0 \int \frac{\mathrm{d}^3 q}{[\omega - \omega(q)]^2 + (\Gamma_0/2)^2}, \tag{2.9}$$

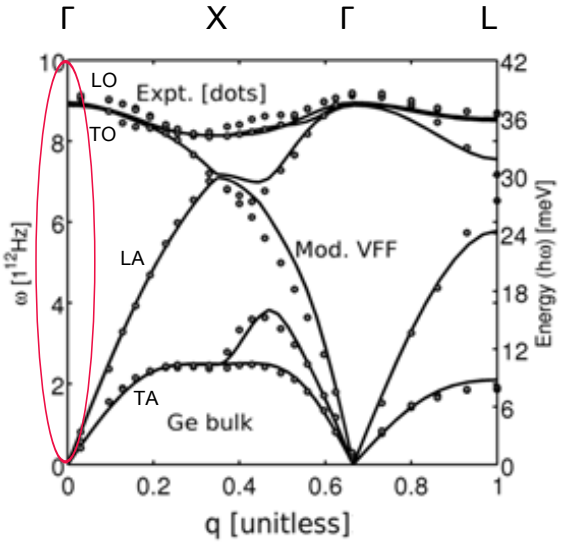

Figure 2.4: The various phonon branches that exist within a crystal lattice. In this application of Raman spectroscopy the LO branch is probed around the origin, i.e. where the wave vector and the momentum are approximately zero, indicated by the red oval. Modified from [78].

where I_0 is an amplitude weighting constant, q is the phonon wave vector, ω is the photon wavenumber, $\omega(q)$ is the dispersion branch to which the mode belongs, and Γ_0 is the natural half-width of the Raman line.

Equation 2.9 is a resonance equation. In the region where ω and $\omega(q)$ are of a similar scale the denominator reduces and the intensity increases resulting in a peak. The Γ_0 term ensures that the peak has the same linewidth as is observed experimentally, as seen in figure 2.3 of Raman spectra of both Si and Ge.

This model assumes that the $k = 0$ condition is held without exception and makes no allowances for when it breaks down. The condition breaks down most obviously for structurally disordered (amorphous) materials. When the periodicity of the lattice is lost and there is no long range order, phonons with a non-zero k can contribute to the signal. This results in a broadening of the Raman signal as an effective density of phonon states is being probed rather than a specific phonon, an

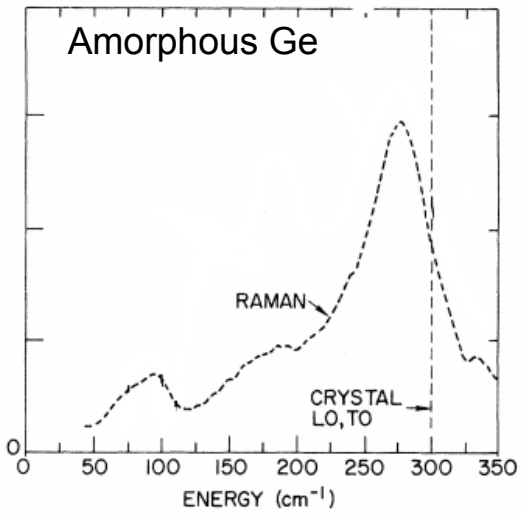

Figure 2.5: The Raman spectrum recorded from amorphous Ge. The peak is shifted and broadened, a consequence of the absence of the long range order found in crystalline samples. Adapted from [80].

example of which can be seen in figure 2.5. In addition to the change in line shape a shoulder is also present at ~ 175 cm^{-1}, and a second peak at ~ 90 cm^{-1}. These features are also characteristic of a sample of amorphous Ge.

Thus the disruption of the periodicity of the system affects the Raman lineshape. In nanoscale materials, whether crystalline or not, long range periodicity is lost due to the fact that there is no long range over which the system can be periodic, and this is expected to be reflected in the Raman signal. This will be addressed in detail in Chapter 3 where the effects of phonon confinement on the Raman signal will be considered.

2.2 Transmission Electron Microscopy (TEM)

Transmission Electron Microscopy is capable of determining the size and shape of nanoparticles to the order of an Angström and as such is a highly useful investigative tool in nanoscience. This small resolution is a result of the short de Broglie wavelength of the high energy electrons used in the imaging process [81]. As the electron beam passes through the sample, electrons are scattered and subsequently focused to form an image, as shown in figure 2.6. The image is then projected onto a luminescent screen or recorded with a CCD. Individual nanoparticles can be observed in the resulting image and so, provided the scale of the image is known, it is possible to assess the average sizes of the nanoparticles in the sample by measuring them directly.

The TEM images were obtained using a JEOL JEM 2010 (200 keV) electron microscope. All samples were mounted on carbon-coated copper grids to facilitate image acquisition. While looking at the nanoparticles essentially directly is an excellent and accurate measure of their size, in the absence of high resolution TEM it is not possible to use this method to gain any insight into the structure of the sample. However, this microscope is equipped with the capacity to perform selective area electron diffraction (SAED, made possible by the 0.15 nm beam diameter), a technique which can probe the structure. Electron diffraction (ED) provides a clear-cut way to investigate the crystallinity of a sample, producing concentric rings and bright dots for a crystalline sample, and broader bands for an amorphous one.

However, both high resolution TEM and ED are known to damage samples via annealing, particularly in nanoparticles [82, 83, 84]. A non-invasive technique that can accomplish structural measurements without annealing, while having other

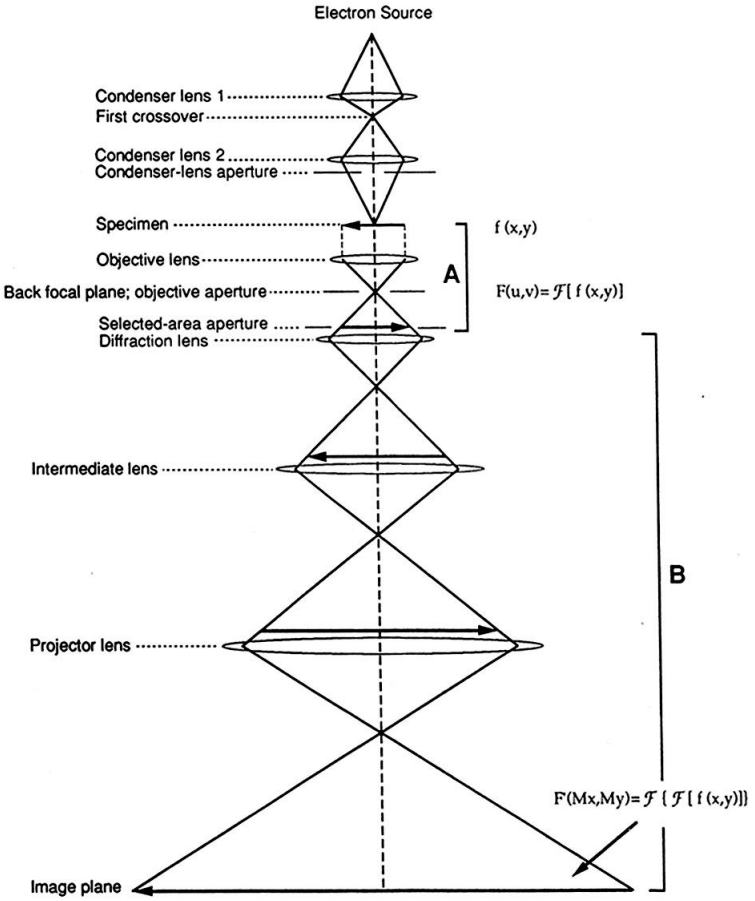

Figure 2.6: A ray-diagram of a TEM. The sample and its images are indicated with horizontal arrows which increase as the image is magnified. In region "A" the sample scatters the electron beam and the first diffraction image is formed. In region "B" the image is magnified and projected onto an image plane, typically a luminescent screen or a CCD camera. Figure reproduced from [70].

qualities particularly useful for nanoparticles, is x-ray diffraction (XRD), outlined in the next section.

2.3 X-ray Diffraction (XRD)

XRD is an experimental technique which excels at probing the long range atomic structure of samples, and is particularly useful for determining the details of crystalline structures. Due to beam size and x-ray penetration length XRD, unlike TEM, provides structural information averaged over a large number of nanoparticles. XRD is advantageous over ED as it doesn't use charged particles and has a significantly reduced beam intensity combined with larger beam size, resulting in less energy being deposited into the sample. Hence the damage or annealing effect this process has on the sample is negligible.

An example of the diffraction process is depicted in figure 2.7. Incident x-rays are reflected from the lattice planes of a crystal. The reflected x-rays will then interfere constructively or destructively, forming an XRD pattern. When the difference in path lengths of subsequent reflections (shown in figure 2.7) is equal to an integer number of wavelengths there will be constructive interference. This is described by Bragg's law, which is given by

$$n\lambda = 2d\sin\theta, \tag{2.10}$$

where n is an integer, λ is the x-ray wavelength, d is the separation of the planes in the lattice, and θ is the angle of incidence of the x-ray beam as shown in figure 2.7.

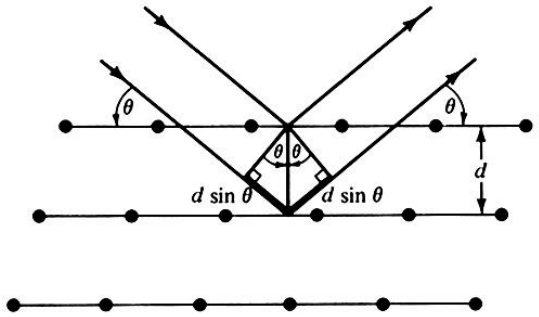

Figure 2.7: Bragg reflection in a crystalline solid. X-rays incident at angle θ reflect from various lattice planes with spacing d and produce a characteristic interference pattern for the sample. The schematic has been reproduced from [85].

XRD can be particularly useful when applied to nanoscale objects. The small scale has a predictable and repeatable broadening affect on the observed peaks in the spectrum. This can be understood by analogy with a diffraction grating. The reduction in the number of layers in the crystal is equivalent to reducing the number of lines on a grating, as the crystal acts as a diffraction grating for x-rays. The more layers that are removed, the broader the peak becomes. Consequently, this broadening has a size dependency and so it is possible to determine the average size of a sample of nanoparticles from its XRD spectrum by using the Scherrer equation [86].

$$\tau = \frac{K\lambda}{\beta \cos\theta} \tag{2.11}$$

where τ is the average particle size, K is the shape factor of the particles (assuming spherical particles $K = 0.9$), λ is the x-ray wavelength, β is the peak width, and θ is the peak position.

XRD was performed at Diamond Light Source at the Rutherford Appleton Laboratory. The experiments were conducted on beamline B18 at room temperature with an x-ray energy of 9500 eV (λ = 1.305 Å) and 8047 eV (λ = 1.541 Å). The system was calibrated using a Si standard that was also utilised to obtain instrumental broadening later used in size analysis through the Scherrer equation.

A sample was inserted into a quartz tube which was then sealed. The sealed tube was then fixed on a rapidly rotating mount. The tube was then aligned using an alignment laser such that while spinning the sample never left the path of the x-rays. The purpose of the rotation of the sample was to avoid any artefacts due to directional dependencies or a non-uniform distribution within the tube. The XRD spectrum was collected with a curved multi-channel detector.

Applying such a technique to nanoscale materials does have some problems. XRD measures long range order and particles on the scale of 3-10 nm can be argued to have no long range across which to be ordered. This means that it will be necessary to employ other techniques alongside XRD in order to better understand local atomic arrangements. X-ray absorption spectroscopy (XAS) is one technique that can provide local structural information, detailed in the following section.

2.4 X-ray Absorption Spectroscopy

2.4.1 EXAFS

XAS is a experimental technique used to study the short range structure around a specific element in a sample. The element specificity of XAS combined with the fact

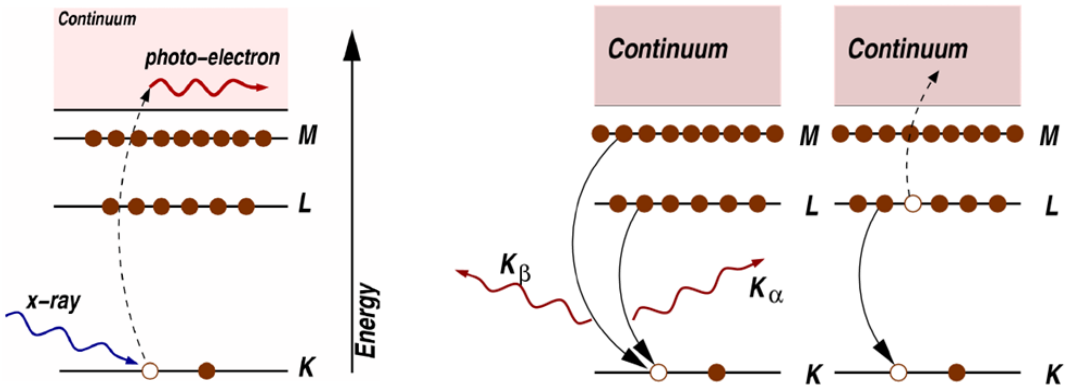

Figure 2.8: The excitation and de-excitation processes in XAS. An incident x-ray excites a core electron to the continuum. Outer shell electrons then descend to fill the hole, either emitting x-rays themselves or ejecting an electron.

that it can be applied equally effectively to both crystalline and amorphous samples, from glasses to solutions and even molecular gases, makes it a useful tool in many areas, including physics, chemistry, medicine, and engineering.

In XAS the absorption coefficient of the species of interest, $\mu(E)$, is measured as a function of the incident x-ray energy. The measurements are taken around x-ray energies which correspond to binding energies of inner core electrons, resulting in an absorption edge, as the signal intensity decays rapidly the further the energy is from the edge. The ability to probe the environment of a single element at a time is the consequence of each element having a different set of absorption edges.

There are several ways the absorption coefficient can be measured. Most commonly it is done by measuring the transmission intensity while monitoring the incident intensity and taking the log of the ratio. Excitation and relaxation events are shown in figure 2.8. The emission of visible light from the sample presents an alternative collection method, detailed in 2.5.

Beyond the absorption edge the excited photoelectrons are considered to travel

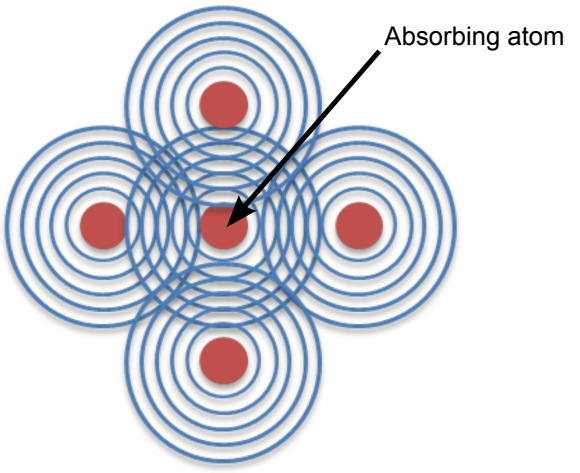

Figure 2.9: When a photoelectron backscatters the wavefunctions superimpose creating an interference pattern which alters the absorption coefficient.

like a wave originating from the atom which then scatters off of neighbouring atoms back to its origin. As this photoelectron wave backscatters it interacts with the outgoing waves and results in an interference pattern which works to alter the absorption coefficient of the material (figure 2.9). The photoelectron wavefuntion, and therefore the interference pattern, is dependent on the energy of the liberated electron and therefore the energy of the incident x-ray.

An XAS spectrum can be subdivided into two main regions, as indicated in figure 2.10, which extends more than 1000 eV into a typical spectrum. This example spectrum has been normalised, eliminating the rapid decay of the signal after the absorption edge. The x-ray absorption near edge structure (XANES) region is typically considered to extend from $\sim$ 30 eV before the edge to $\sim$ 30 eV after the edge. The edge itself has a non-zero width and it is generally considered to be located where the derivative of the rising edge is a maximum. The extended absorption fine structure (EXAFS) extends from the edge of the XANES region to the end of the spectrum. The area before the XANES region is known as the pre-

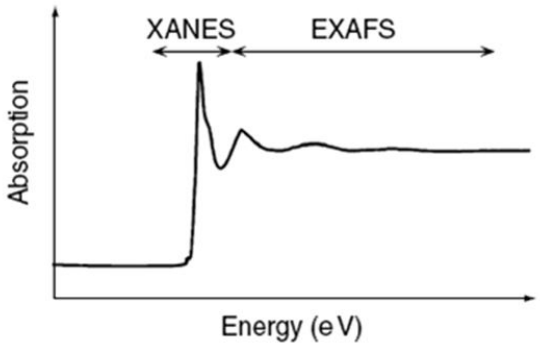

Figure 2.10: An example normalised XAS spectrum. The XANES region is considered to extend $\sim$ 30 eV either side of the absorption edge, and the EXAFS region covers from the end of the XANES region to the end of the spectrum. Reproduced from [87].

edge region, and is essential in background subtraction and normalisation (for details see Appendix C.1). The fine structure refers to the fluctuations in the absorption coefficient after the absorption edge, which are the result of the interference pattern of the photoelectrons.

For the purposes of analysis the EXAFS function $\chi(k)$ is defined as

$$\chi(k) = \frac{\mu - \mu_0}{\mu_0}, \tag{2.12}$$

where μ is the effective observed absorption coefficient, and μ_0 is the ideal monoatomic absorption coefficient (that is, its value in the absence of any backscattering effects). The value of μ_0 is often approximated using a smooth spline function as it is often not possible to measure it experimentally.

The Standard EXAFS Equation was derived in 1975 by Stern *et al* [88] and is used to fit XAS spectra in order to extract relevant structural parameters from them. The Standard Equation describes $\chi(k)$ as

$$\chi(k) = \sum_i \frac{N_i A_i(k) S_0^2}{k R_i^2} \exp\left[\frac{-2R_i}{\lambda(k)}\right] \exp\left[-2k^2\sigma_i^2\right] \sin\left[2kR_i + \phi_i(k)\right], \qquad (2.13)$$

where N_i is the coordination number, $A_i(k)$ is the amplitude, S_0^2 is the scattering amplitude attenuation, R_i is the absorber-scatterer distance, $\lambda(k)$ is the electron mean free path (EMFP), σ_i^2 is the root mean square deviation (RMSD) value from R_i, and $\phi(k)$ is the phase difference between the outgoing and backscattered photoelectron. This standard equation does not account for multiple scattering.

For the purposes of analysis the EXAFS spectra are fitted using the *FEFF* code [89] via a package of user interfaces known as *Demeter* [90, 91], containing *Athena* and *Artemis*. *Athena* is used first for background subtraction and normalisation. The algorithm *Autobk* performs the background subtraction using some initial parameters (see Appendix C). The normalisation process is to correct for variations due to the sample thickness and sample preparation, among others. Once these preparatory steps are performed *Artemis* may be used to fit the data after it has been Fourier transformed giving a pseudo radial distribution function. Once a structural model is loaded in to the software the expected scattering paths of the electron are generated. Inputting some relevant structural parameters then allows *Artemis* to refine them and find how well the data agrees with the expectations of the model. This can be performed repeatedly for different structural models to find the best fit.

XAS experiments were conducted at beamline B18 at Diamond Light Source. All data were collected at the Ge K-edge ($\sim$ 11 keV) with samples prepared to utilise the advantages of the thin limit [92] to ensure consistency between transmission and

optically-detected signals (detailed in section 2.5). Ion chambers were used to record XAS data in transmission mode. XAS data collected for a reference bulk Ge was used to obtain the value of the scattering amplitude, S_0^2 (see equation 2.13), which was then used in fitting sample data.

XAS is a general technique applicable to almost all materials. When a sample is photoluminescent the x-ray excited optical luminescence (XEOL) signal can be collected to determine the local structure around the luminescent species. The following section describes this technique.

2.5 Optically Detected EXAFS (OD-EXAFS)

One technique that is capable of directly linking light emission with the structure is OD-XAS. First shown to directly correlate with data collected by XAS by Bianconi *et al* in 1978 [93], OD-XAS enables structural data to be obtained directly from XEOL and has already been used to address the origins of PL in porous silicon (pSi) [31, 94, 95, 96, 97]. OD-XAS utilises the fact that the XEOL signal is sensitive to the photoelectron generation in the x-ray absorption process near and above the x-ray absorption edge of an element.

An example of an OD-XAS spectrum for CaF_2 can be seen in figure 2.11. Part (a) is the XAS type, and (b) , (c), and (d) OD-XAS type, (b) (powder) being closest to our case of nanoparticles. The signals from part (a) and (b) are clearly equivalent in terms of fine structure, while OD-XAS tends to be noisier. Parts (c) and (d), a pellet and single crystal respectively, clearly demonstrate that the quality of the signal depends on the sample preparation [92]. The inverted edge jump is observed

in (c) and (d) because the increased thickness of the sample leads to reabsorption and scattering of the measured signal.

The XEOL-related x-ray absorption signal is measured by recording the integral PL yield within a selected wavelength range. Therefore OD-XAS is sensitive to a subset of sites related to the light emission. Despite its capabilities, OD-XAS can not provide an unambiguous answer as to the origins of PL in pSi. One of the main reasons for the ambiguity is the sensitivity of the OD-XAS method to the sample preparation [40] which precluded wider use of the technique. Another difficulty is in assessing spatial sensitivity of OD-XAS on the scale of a few nm [94, 95].

As alluded to previously, the PL of the samples in question allows an alternative collection method to be used. While PL is usually driven by a laser in the nanometre wavelength range, x-ray bombardment results in XEOL. Electrons are excited in the same manner as in EXAFS, and eventually decay to the bottom of the conduction band. Once at the bottom of the conduction band they can further decay across the band gap and contribute to a XEOL signal, as in figure 2.12. XEOL allows one to extract a spectrum with a similar basic structure to EXAFS as in figure 2.10.

By collecting the optical luminescence as a function of the incident x-ray energy it is possible to analyse the intensity of the XEOL in a similar way to a XAS spectrum. This allows further discrimination by reducing the signal collected from every atom of a particular element, to a subset of those which are luminescent. Thus the signal can offer insight into what environment the luminescent atoms are in and so what type of environment is conducive to this behaviour.

The XEOL signal can be expressed in terms of the EXAFS function, equation

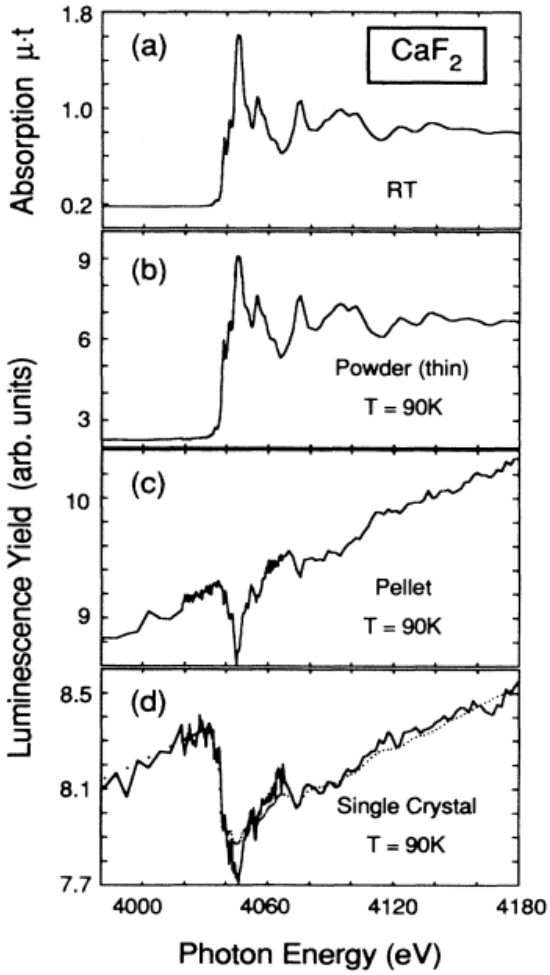

Figure 2.11: Example OD-XAS signals compared to a XAS signal, (a). Signals (b), (c), and (d) are the OD-XAS for a powder, pellet, and single crystal respectively. Key features of the XAS signal are reproduced in the OD-XAS, particularly for a powder in the thin limit, which is almost interchangeable. The inverted edge jump is observed in (c) and (d) because the increased thickness of the sample leads to reabsorption and scattering of the measured signal. The OD-XAS signal tends to be noisier than the XAS signal [92].

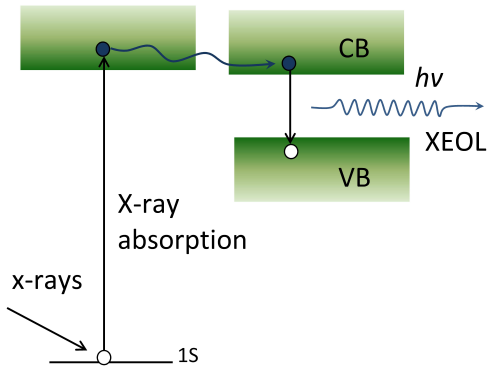

Figure 2.12: Electrons that are excited from the core shells by the incident x-rays can ascend to the conduction band and cross the band gap, contributing to XEOL signal. The conduction band is labelled CB, the valence band VB.

2.12. As shown in [92] and [98] the XEOL signal intensity is given by

$$\mathrm{d}I_{XEOL}(x) = \mu\eta I(x)\mathrm{d}x, \tag{2.14}$$

where μ is the absorption coefficient, η is the light emission coefficient, $I(x)$ is the intensity of the incident x-rays at depth x in the sample. Substituting $I(x) = I_0 \exp(-x\mu)$ and integrating over x for a sample thickness d gives

$$I_{XEOL} = I_0\mu\eta[1 - \exp(-d\mu)] \tag{2.15}$$

where I_0 is the intensity of the incident x-ray beam. As the sample of interest is comprised of nanoparticles the exponential term may be expanded in the limit of small d, giving

$$I_{XEOL} = I_0\mu_0\eta d(1 - \chi), \tag{2.16}$$

where μ has been expanded in terms of the EXAFS function as in 2.12.

While in principle the optically detected extended absorption fine structure (OD-EXAFS) spectrum can be analysed by the same process as described for EXAFS, in practice the increased level of noise often prevents this. The restriction due to noise could be ameliorated with a sufficiently long collection, but this is often prohibitively time consuming. As the magnitude of the fine structure perturbations diminishes rapidly with energy it reaches the level of the noise at a lower energy than for EXAFS. The shorter extent of the spectrum means a less accurate Fourier transform, often to the point where the smaller differences that this technique would be used to illuminate would be lost entirely. This may not necessarily be disastrous, however, as the normalised, background-subtracted signal can be used to gain insight by comparing it to other OD-EXAFS spectra.

OD-XAS experiments using the XEOL signal were conducted at beamline B18 at Diamond Light Source. All data were collected at the Ge K-edge ($\sim$ 11 keV) with samples prepared to utilise the advantages of the thin limit [92] to ensure consistency between transmission and optically-detected signals. The thin limit removes the possibility of any thickness based effects such as negative edge jumps, positive jumps with an inverted oscillation, and overtone oscillation in OD-XAS. Consequently standard analysis is always applicable which simplifies data interpretation. The detection system consisted of a Triax 190 spectrometer equipped with a Synapse CCD and a Newport VIS Femtowatt photoreceiver. A Hamamatsu R3809U-50 MCP photomultiplier was used for low signal conditions. The light was delivered to the spectrometer using an optical fibre. All experiments have been conducted at T = 100 K using a cryojet system.

The following section details high pressure Raman spectroscopy using a diamond anvil cell, which was used to alter the structure of nanoparticles.

2.6 High Pressure Raman Experiments Using the Diamond Anvil Cell

Raman experiments under high pressure are performed in essentially the same way as as the ambient pressure Raman experiments described in section 2.1 with the addition that the sample is now housed in a diamond anvil cell (DAC). This allows a variable pressure to be applied to the sample and so adds an extra dimension to the investigative capabilities as high pressure can be used to alter the atomic structure of samples. The standard Bridgman type DAC used is shown in figure 2.13. It is capable of operating over the range of 1 - 500 GPa, and so will be more than adequate for investigating Ge nanoparticles as amorphous Ge has a transition pressure of $\sim$ six GPa [99] and crystalline Ge has a transition pressure of $\sim$ 11 GPa [100].

The Bridgman DAC has three main components. Firstly are the two diamonds (shown in blue in figure 2.13), typically of about one third of a carat, which have their narrow, parallel faces opposing each other. The culet where the diamond faces make contact is typically $\sim$ 0.6 mm in diameter. It is this narrow diameter and therefore small surface area coupled with the diamonds relative incompressibility that allows such high pressures to be achieved. Second is the force exerting device (grey in figure 2.13) which holds the diamonds in place and, by tightening the screws (labelled), can be used to press the diamonds together from either side. Screws, or sometimes a lever arm, are ideal as they allow the pressure to be incremented gradually, allowing for a plethora of data points. Thirdly is the gasket (labelled). This is comprised of a hard metal foil which prevents the diamond faces from coming in to contact. The gasket has a cavity in which the sample and a hydrostatic medium are contained so

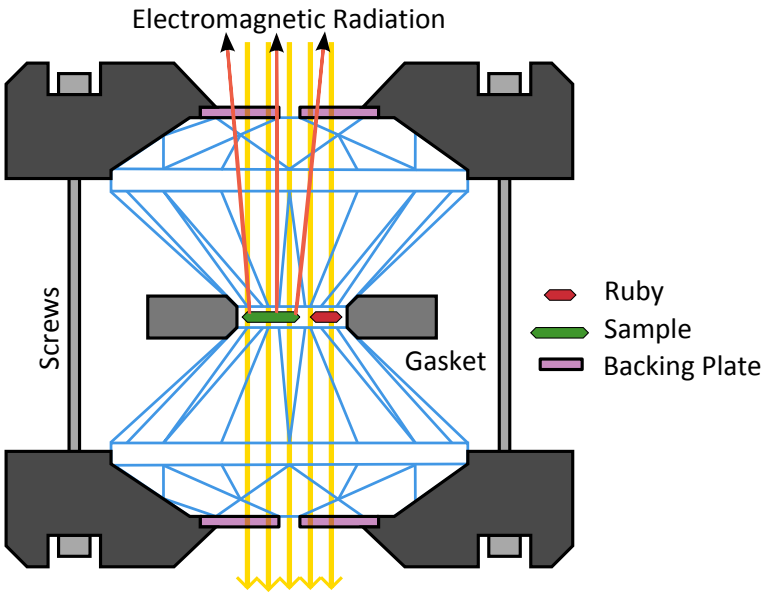

Figure 2.13: A Bridgman type Diamond Anvil Cell shown in cross section. Applied pressure is increased by tightening the screws. The ruby is present for pressure calibration purposes. Modified from [102].

that they may be compressed [101].

The samples were mounted in the DAC and the same Raman equipment as used for ambient pressure experiments was used. The samples were loaded in to a hole drilled in a pre-indented gasket together with small amounts of ruby and a pressure transmitting medium (in this case a methanol-ethanol mix). Once mounted, the Raman spectra was acquired at various pressures up to $\sim$ 17 GPa where the signal approached the level of the noise. The pressure was calibrated by observing the change in the PL of the included ruby as its high pressure behaviour is well characterised over the range of pressures that were observed [103, 104].

The next section briefly describes the production methods of the samples analysed using the above techniques.

2.7 Sample Preparation

The samples detailed below along with their production methods were the focus of the study. They represent a good cross-section of the Ge nanoparticle family. The sample preparation includes techniques which start with a bulk phase sample and reduce the size to the nanoscale, known as a top-down method. They also include methods which begin with molecular compounds of Ge which are then reduced and grown to the nanoscale, known as a bottom-up method. This variety allows the investigation of whether some, all, or any of the observed characteristics are affected by the particulars of the formation of the nanoparticle or if they are essentially irrelevant. The sample set also contains samples which have been produced with different surface termination. This allows some investigation into the sensitivity of the particles characteristics to the species bonded to its surface, if any. The samples were produced by Dr. Ali Karatutlu, and extensive information on the below synthesis techniques can be found in [105].

Chemical etching is a fundamental top-down method. Hydrofluoric acid (HF) is added to crystalline particles of Ge that are of the order of microns in size and the acid corrodes them down to the nanoscale [106, 107]. While this is one of the simpler methods (despite the inherent risks when using HF) it is necessary to be very exact with the mixture and timings, otherwise it is possible to miss the nanoscale window and completely destroy the particle's. Alternatively, the nanoscale window may not be reached at all and this may not apparent until further analysis of the sample (TEM, Raman, PL, etc.) by which time it is too late to reduce the size further without repeating the experiment completely. The chemically etched samples are terminated with hydrogen. Oxygen terminated samples were produced by allowing

them to oxidise in air for several weeks.

Sol-gel synthesis is a technique used to produce materials from smaller molecular compounds [108, 109]. The "sol" part of the name comes from the colloidal solution that is produced by the conversion of monomers. This then evolves towards a multi-phase gel containing both solid and liquid phase material. After a drying process and thermal treatment the end result is either a polymer network or a set of independent particles, as in the present case.

Colloidal synthesis is another bottom up method. A colloidal solution contains three basic constituents: solvents, surfactants (typically organic), and precursors. The solution is heated which results in the precursors transforming to monomers. The monomers will eventually supersaturate the solution. Once a sufficient level of supersaturation has been achieved nanoparticles will begin to grow via a process of nucleation [36, 37, 38, 110]. Two samples were produced via colloidal synthesis using two different precursors. The first used GeO_2 as a precursor and is denoted with Ca1, the second used $GeCl_4$ and is denoted as Cs1.

This concludes the detailing of the experimental techniques and the samples they will be used to probe. In the next chapter the mathematical model of Raman spectroscopy will be discussed, and how phonon confinement effects are integrated into it.

Chapter 3

Mathematical Modeling of Phonon Confinement in Quantum Structures

3.1 Phonon Confinement

Given the right conditions, Raman spectra can display sensitivity to the size of the system. The sensitivity can be observed experimentally when the size of the nanoparticles decreases, as the Raman peak position gets down-shifted and asymmetrically broadened. This can be seen in figure 3.1. The changes happen in a predictable way and as such can be used to determine the average size of the nanoparticles in the sample to a level of accuracy (typically around 0.5 nm [111]) determined by the resolution of the spectrometer (typically ≈ 1 cm^{-1}). The shift and broadening is a consequence of phonon confinement and the Heisenberg uncertainty principle.

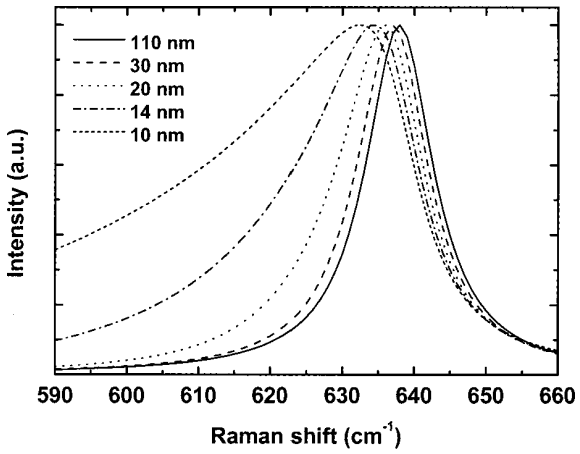

Figure 3.1: Reducing the size of the nanoparticles leads to the Raman line shape becoming down-shifted, broadened and asymmetric. In this case the material was SnO_2 [4].

For a finite sized domain which is smaller than the mean free path of a phonon the requirement that $k \approx 0$ is relaxed for the Raman signal. The uncertainty in the phonons position is reduced under the assumption that the phonons are confined to the nanoparticle, and so the uncertainty in k can increase. This means that phonons with non-zero k vector can participate in the Raman scattering [4]. The contribution of these additional phonons means that effectively the phonon density of states is being measured rather than the single point at $k = 0$. The asymmetry is a result of the shape of the phonon dispersion curve seen in figure 2.4. The LO phonon dispersion curve has a negative gradient. As the nanoparticle gets smaller the relaxation of the $k \approx 0$ selection rule increases, allowing phonons with increasing momentum (and therefore decreasing energy) to become increasingly involved and consequently the lower energy side of the peak broadens more rapidly than the higher energy side leading to the characteristic asymmetry seen in figure 3.1 [79].

A fundamental part of the phonon confinement model is that it relies on an expression for a phonon dispersion curve. This presents a problem when the

nanoparticles are smaller than a critical size, generally taken to be around 2.2 nm [51]. Below this limit the nature of the vibrations in the lattice are no longer well described by the bulk phonon dispersion curves. For sizes lower than this boundary an alternative system called the elastic sphere model can be used [79]. The elastic sphere model quantises vibrational modes perpendicular and parallel to the surface of the sphere, where the sphere is the nanoparticle (this model assumes spherical nanoparticles). In the majority of cases considered from the literature the phonon confinement model is sufficient and so the elastic sphere model will not be elaborated upon further.

The behaviours described above are accounted for in the phonon confinement model. The following section details the mathematics behind the phonon confinement model, and some of the discussion surrounding it.

3.2 The Phonon Confinement Model

In order for Raman spectroscopy to be of any practical use in particle size analysis it is necessary to have a model that reliably reproduces phonon confinement. Richter *et al* [5] proposed a very intuitive model based on phonon confinement which was later refined by Campbell and Fauchet [112]. The model is largely empirical, but is ultimately quantum mechanical as it relies on the phonon wave vector q. Richter *et al* start by describing the wavefunction for a phonon in an infinite crystal as

$$\Phi(q_0, r) = u(q_0, r)e^{-iq_0 \cdot r}, \tag{3.1}$$

where q_0 is the wavevector of the phonon. When $u(q_0, r)$ has the periodicity of the lattice then a phonon in a spherical nanoparticle of diameter L becomes

$$\Psi(q_0, r) = W(r, L)\Phi(q_0, r) = \Psi'(q_0, r)u(q_0, r), \tag{3.2}$$

where $W(r, L)$ is the phonon weighting function and L is the particle size, and the phonon is localised to $r < L$.

Richter *et al* used the Gaussian $e^{-(2r^2)/L^2}$ for the $W(r, L)$ term, and a set the amplitude of the phonons to be $1/e$ at the edge of the nanoparticle. Campbell and Fauchet note that this choice is not grounded in any theory, stating that there is no physical reason to assume this form of confinement or its particular value at this boundary [112]. Campbell and Fauchet go on to expand the Ψ' term in a Fourier series as

$$\Psi'(q_0, r) = \int \mathrm{d}^3 q C(q_0, q) e^{iq \cdot r}, \tag{3.3}$$

where $C(q_0, q)$ are Fourier coefficients determined by

$$C(q_0, q) = \frac{1}{(2\pi)^3} \int \mathrm{d}^3 r \Psi'(q_0, r) e^{-iq \cdot r}. \tag{3.4}$$

A superposition of eigenfunctions with q wavevector centred at q_0 make up the phonon wavefunction. The modified first order Raman spectrum is then given by

$$I(\omega) = I_0 \int \frac{\mathrm{d}^3 q |C(0, q)|^2}{[\omega - \omega(q)]^2 + (\Gamma_0/2)^2}. \tag{3.5}$$

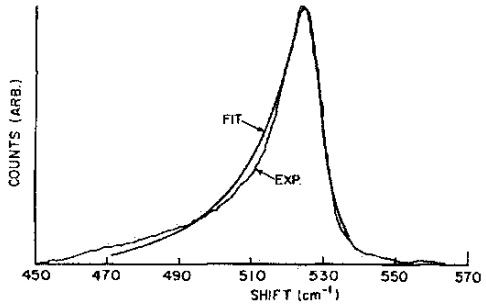

Figure 3.2: Campbell and Fauchet's model for Raman peak shift (FIT) shows good agreement with experimental data (EXP). Reproduced from [5].

To simplify the calculation Campbell and Fauchet consider the phonon dispersion curves to be isotropic and use a spherical Brillouin zone. The selection rule $k \approx 0$ means that this assumption is justified as in such a small region close to the origin the approximation is effectively identical to its more complex counterpart. Campbell and Fauchet then go on to criticise Richter's choice of weighting function, and therefore Fourier coefficients. They conclude that the Fourier coefficients that provide the best fit for the data for spherical nanoparticles are given by

$$|C(0,q)|^2 = \frac{1}{(16\pi^4 - q^2L^2)^4}, \tag{3.6}$$

as opposed to Richter's coefficients, which are described by

$$|C(0,q)|^2 = e^{-q^2L^2/4}. \tag{3.7}$$

The Campbell and Fauchet model fits the data well, as can be seen in figure 3.2.

A key part of the phonon confinement model is the phonon dispersion curve,

which is different for each material. Having a good mathematical description for this is vital to the validity and usefulness of the model. The following section details the phonon dispersion curve used in our implementation of the model.

3.3 The Phonon Dispersion Curve

In most of the earlier Raman studies of nanoparticles the expression for the phonon dispersion curve for the calculation of the intensity was empirical and selected to be that which was most easily presented or fit to the smoother curves. An example of a dispersion curve used by Faraci *et al* [113] for Si is

$$[\omega(q)]^2 = 522^2 - \frac{126100q^2}{q + 0.53}. \tag{3.8}$$

This method has been criticised by Gupta *et al* [6, 114] who present an alternative (see figure 3.3). By taking the phonon dispersion curve in the Γ-X direction of the Brillouin zone they use the analytical form

$$\omega(q) = \sqrt{A + B\cos(qa/2.6)}, \tag{3.9}$$

where a is the lattice constant. Gupta *et al* claim that this dispersion curve improves the fit over Faraci *et al* Their evidence for this can be seen in figure 3.3 which is an example with Si.

The quality of the phonon dispersion curve is not the only limitation of the model. The following section discusses other limitations of the model and their potential consequences.

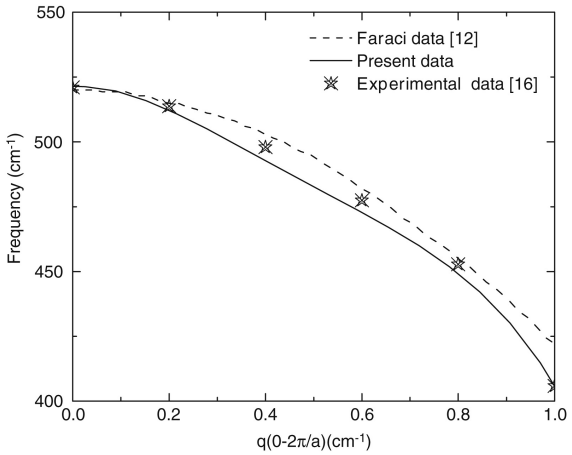

Figure 3.3: Faraci *et al*'s and Gupta *et al*'s (listed in the legend as "Present data") fit for the LO phonon dispersion curve in Si and the experimental data for same. Reproduced from [6].

3.4 Limitations of the Phonon Confinement Model

3.4.1 Intrinsic Limitations of the Model

It is important to note at this point that the accuracy of the size determined from Raman measurements is only as accurate as the model is. Further, it may not necessarily correspond to the actual nanoparticle size, it can be a measure of any spatially limiting factor that the phonons may encounter. This can include, but is not limited to, twins, stacking faults, inclusions, vacancies, boundaries and pores [79]. Thus, it is more rigorous to describe the result as a coherence length defined as $2\pi/\Delta k$, where Δk is the change in wave vector between $q_0(=0)$ and q. It has been shown that this coherence length can be the size of the nanoparticle by Li *et al* [115], while Du *et al* [116] demonstrate that it can be representative of the spacing between defects or impurities. The various potential definitions of the coherence length show that great care must be taken when using Raman measurements to estimate particle size. This is exemplified by Weber *et al* [117] who found an order

of magnitude difference to the results found with electron microscopy. A most interesting and useful result is that of Carles *et al* [118] who showed that the meaning of the coherence length can change, it corresponds to the grain size for larger grains, but represents the domain size in smaller grains that have undergone alloying.

3.4.2 Size and Shape Effects

Another potential issue is that the phonon confinement model assumes uniform size and shape. As presented in equation 3.5 there is no allowance for particle size away from the average, and the $|C(0,q)|^2$ term is chosen for a given shape with no latitude for deviation (spheres, rods, wires etc.). This is not representative of real samples, as there will always be particles deviating from the average. Gupta *et al* [6] have made some progress in allowing for a range of sizes by introducing another term to equation 3.5 so that it becomes

$$I(\omega) = \int \rho(L)\mathrm{d}L I_0 \int \frac{\mathrm{d}^3 q |C(0,q)|^2}{[\omega - \omega(q)]^2 + (\Gamma_0/2)^2}, \tag{3.10}$$

where $\rho(L)$ is the log-normal size distribution which corresponds to the density of vibrational states as each particle vibrates with a frequency that is inversely proportional to its size. The log-normal distribution has the form

$$\rho(L) = A \exp\left(\frac{-\log(L/L_0)^2}{2\sigma^2}\right), \tag{3.11}$$

where σ is a measure of the distribution width, L_0 is the size that corresponds to the maximum of the distribution and A is a constant. The effect that the inclusion of a size distribution can have on the fitting has been shown by Adu *et al* [7], as

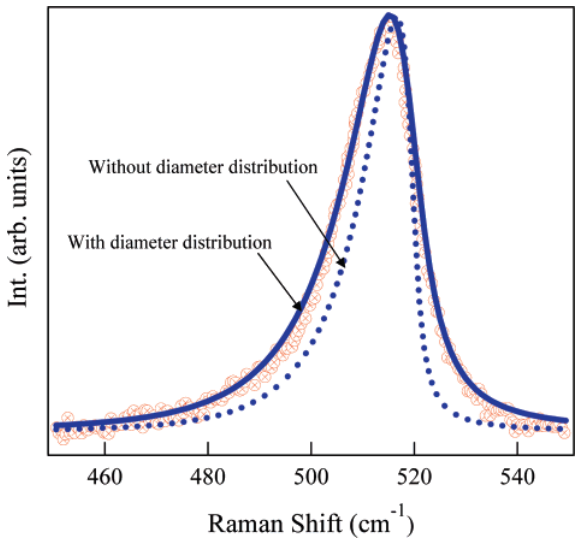

Figure 3.4: The Raman spectrum for Si nanoparticles from Adu *et al* [7]. The red circles represent the data. The blue circles represent the fit calculated when assuming no size distribution, while the solid blue line represents the fit calculated when a log-normal particle size distribution is included. Both fits use the phonon confinement model. Reproduced from.

seen in figure 3.4. The size distribution used is log-normal, which they show in the same paper to be the most appropriate for their sample. This goes some way to dealing with the variation in particle size within a sample, but the issue of variation of shape remains unaddressed.

3.4.3 Surface Phonons

As discussed in section 1.1, a nanoparticle can be formally subdivided into two regions, the inner core and the outer surface. These two regions differ in coordination numbers and in the average bond length. This is due to the difference in forces experienced by the atoms in each region. All the atoms in the core are bonded uniformly to neighbours of like atoms so it resembles the bulk in structure. However, in the surface the nanoparticle is either passivated by being capped with atoms of

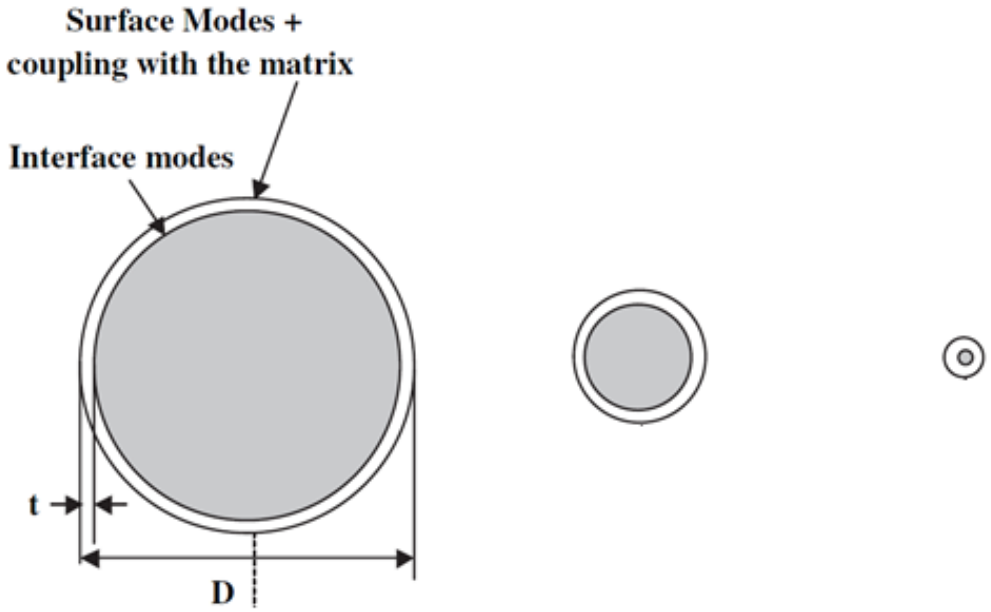

Figure 3.5: The thickness of the surface layer, t, is largely independent of nanoparticle size, D. [79].

some other element (e.g. hydrogen or oxygen) or there are dangling bonds leading to surface reconstruction. This changes the forces experienced by the atoms in the surface layer. If the forces are not isotropic then the atoms will shift from where they would be expected to be located in a bulk lattice to a new position of equilibrium resulting in surface relaxation. This change in bond strength and length influences phonon behaviour and so changes in these parameters will change the observed Raman spectra.

The thickness of the surface layer is generally unaffected by the size of the nanoparticle as illustrated in figure 3.5 and so as the size is reduced the significance of the effects of the surface increases.

The work of Liu *et al* [119] has shown that the effect of nanoparticle/substrate interfaces may work to mitigate the effect of ignoring surface phonons. By dropping

Si nanoparticles into porous Si they found that three new peaks became apparent which had never been observed in amorphous, crystalline, nano, or porous Si. Due to the similarity to the work reported by Duval *et al* [120], Liu *et al* concluded that these peaks are from surface modes, and that they are usually eliminated by extensive interfaces. The position of the peaks correspond very closely to those predicted by their model which assumes that the surface of the nanoparticles is free. If these surface phonons are suppressed when the nanoparticles are not quasi-free, it is possible that any contribution to the LO peak, which is typically the phonon branch of interest, is suppressed as well. While this means that there is no particular issue for the majority of cases examined that are on a substrate, it has the potential to pose problems for some nanoparticle applications, such as anything biological. This is because the nanoparticles will no longer be confined to a substrate and aggregated together, but will be free floating and diluted. However, it is also possible that this effect could lead to benefits, as the three new peaks appear to be dependent on nanoparticle diameter as well, and so could potentially be used in conjunction with the typically used LO peak to determine the character of the nanoparticles to a greater level of accuracy.

3.4.4 Assumption of Isotropy

The phonon confinement model contains the assumption that the nanoparticles are isotropic. It is probable that this is acceptable for most, if not almost all, materials in the limit of q close to the Brillouin zone centre [121]. However, a more effective method is to integrate equation 3.5 along the main directions of the Brillouin zone [122].

The integral in equation 3.5 is one dimensional and so assumes that the phonon dispersion is isotropic. Recent work by Korepanov *et al* [123] details a method for allowing for anisotropy in the phonon dispersion. The anisotropy they address can be seen in figure 3.6. While their work is looking specifically at diamond nanoparticles, this approach would be equally as valid for Ge as the structure is the same, and the apparent anisotropy of the phonon dispersion in Ge is shown in figure 1.6. A further important change made in [123] is to integrate from $-\infty$ to $+\infty$ rather than from zero to one, which is necessary as the lattice periodicity is broken. Their version of the integral thus becomes

$$I(\omega) \cong \int\int\int_{-\infty}^{\infty} \frac{\exp\left(-q^2\sigma^2/12\right)}{(\omega-\omega(q))^2+(\Gamma_0(\sigma)/2)^2} \mathrm{d}q_x \mathrm{d}q_y \mathrm{d}q_z. \tag{3.12}$$

The current usefulness of Korepanov *et al*'s method is limited by the reliability of the available experimental data for nano scale particles [123]. Combining this with the requirement for pressure dependent phonon dispersion curves for each $\mathrm{d}q_x$, $\mathrm{d}q_y$, and $\mathrm{d}q_z$, it will probably be some time before this method could be implemented effectively for our purposes.

The following chapter details and discusses the results of the experimental procedures. Specifically, PL, TEM, XRD, and Raman Spectroscopy.

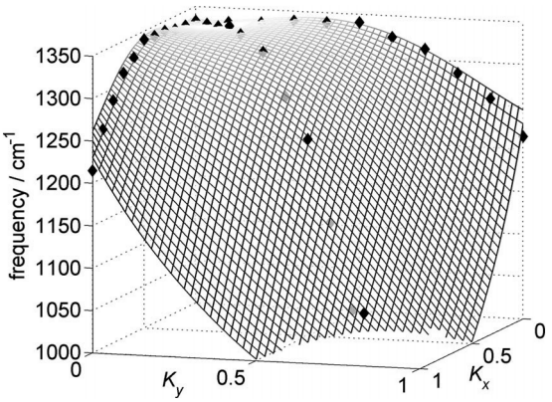

Figure 3.6: The phonon dispersion sheet in the (100) and (110) directions for LO phonons in the first Brillouin zone. The points are experimental results used for fitting [123].

Chapter 4

Structural Characterisation Results and Discussion

4.1 Photoluminescence Results

PL measurements were collected with a He-Cd laser (442 nm) coupled to a TRIAX 320 spectrometer equipped with a photomultiplier, via optical fibre. The experimental resolution was one nm [124]. PL measurements were performed to ensure that the samples were indeed photoluminescent. The change in light emission was as it is expected to be if the band gap had changed in accordance with the quantum confinement model. Light emission is very important for potential applications and is also important as it is a prerequisite for OD-XAS studies.

The difference in colour between nanoscale samples and bulk is shown in figure 4.1 and is a clear indicator that there is a change in the band gap when a sample is reduced to nanoscale. This change is continuous and results in a shift in the PL

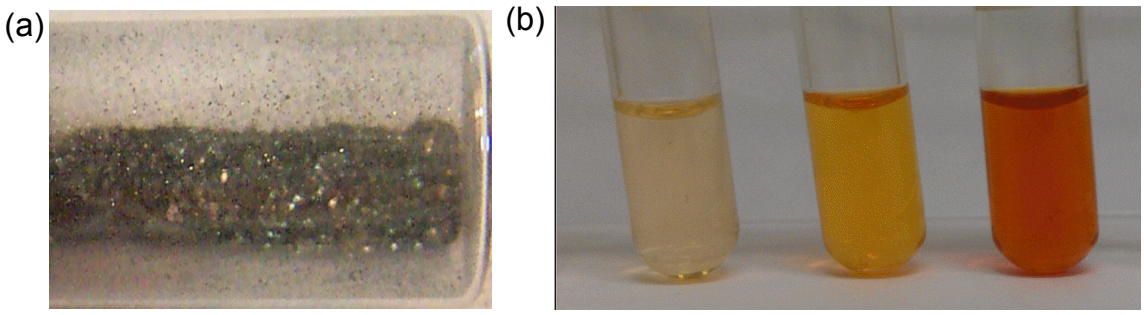

Figure 4.1: Panel (a) shows powdered bulk Ge. Panel (b) shows Ge nanoparticles, whose colour is markedly different from that of bulk Ge. Shown here are increasing concentrations of colloidally produced nanoparticles achieved by centrifugation. Image of bulk Ge from [125].

peak which is dependent on the particle size as shown by Brus [68]. Consequently the PL peak position can be used to infer details of the nanoparticles size [126] using

$$R = \left(\frac{\pi^2 \hbar^2}{2\mu(E_\Delta - E_g)} \right)^{1/2}, \tag{4.1}$$

where R is the nanoparticle size, $\mu(0.028m_0)$ is the reduced mass of the exciton (electron-hole pair), E_Δ is the energy of the emitted photon, and E_g is the bulk band gap. Equation 4.1 assumes that the emission is from electrons relaxing across the band gap. Consequently PL can be used to probe whether this is the source of emission in the samples by comparing the result to that obtained by other techniques. The photoluminescence can be seen in figure 4.2.

Figure 4.3 shows the PL spectra for the samples produced via chemical etching (oxygen and hydrogen terminated), and sol-gel synthesis. The hydrogen terminated etched sample has a peak at around 773 nm, which corresponds to a particle size of 4.2 ± 0.1 nm. The oxygen terminated etched sample has been fitted using MagicPlot [127]. The best fit was determined by maximising the value of Q, the quality of fit. The best fit had a Q value of 0.9985 and was found to consist of three Gaussian

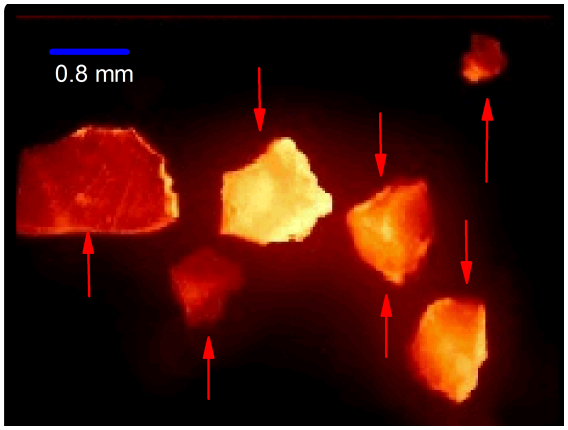

Figure 4.2: The photoluminescence (442 nm excitation) exhibited by nanocrystalline Ge embedded in silica is clearly visible to the naked eye.

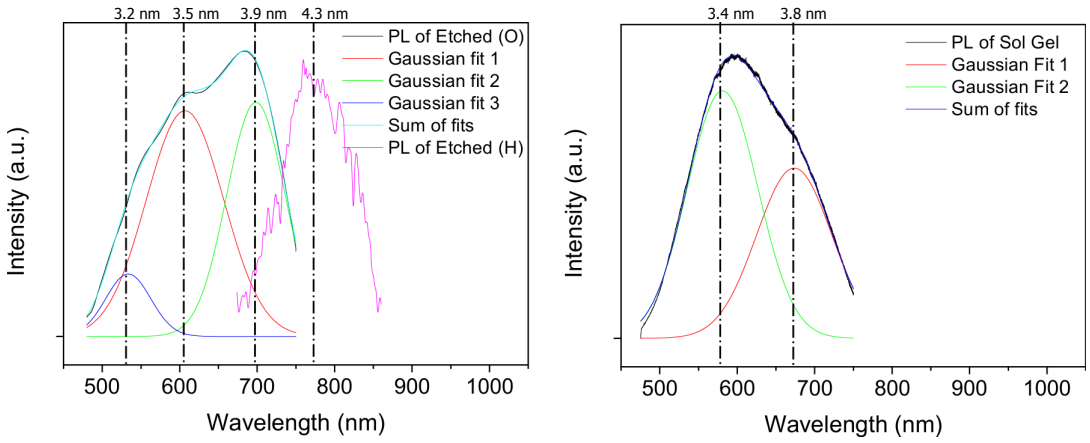

Figure 4.3: The photoluminescence spectra etched (left) and sol-gel (right) samples (442 nm excitation). The oxygen terminated etched sample and sol-gel sample consisted of multiple peaks and have been fitted with MagicPlot. The peaks in the oxygen terminated etched sample correspond to sizes of 3.9 $\pm$ 0.1 nm, 3.5 $\pm$ 0.1 nm, and 3.2 $\pm$ 0.1 nm. The hydrogen terminated etched sample peak corresponds to a size of 4.3 $\pm$ 0.1 nm. The sol-gel sample peaks correspond to sizes of 3.8 $\pm$ 0.1 nm and 3.4 $\pm$ 0.1 nm.

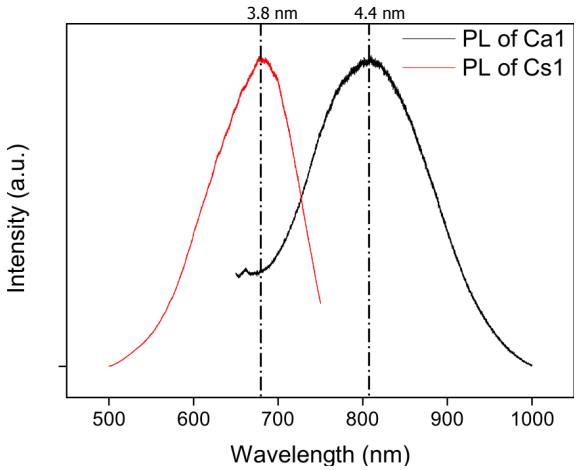

Figure 4.4: The photoluminescence spectra of the colloidal samples (Ca1 and Cs1, 442 nm excitation). The peak positions of Ca1 and Cs1 were found to have peaks that correspond to particle sizes of 4.4 ± 0.1 nm and 3.8 ± 0.1 nm respectively.

peaks, centred at 698 nm, 605 nm, and 532 nm. These would correspond to particle sizes of 3.9 ± 0.1 nm, 3.5 ± 0.1 nm, and 3.2 ± 0.1 nm respectively. However, it is typical that oxidation leads to a shift of the PL peak towards shorter wavelengths [128], and as such it is likely that the PL spectrum collected from the oxygen terminated particles is shifted not only as a result of their reduced size, but also as a consequence of their oxidised state. This renders their size estimation less useful than that of the hydrogen terminated particles, but may offer insight as to where the optical emission is originating, as is investigated later. As the oxygen terminated etched particles have three peaks it is of course possible that there is emission from multiple substructures. For instance, from the nanocrystalline Ge, or from the oxidised surface layer.

The peak for the sol-gel sample was fitted with two Gaussian curves. The best fit (with an Q value of 0.9991) was found to have peaks at 673 nm and 581 nm, which would correspond to particle sizes of 3.8 ± 0.1 nm and 3.4 ± 0.1 nm. Once again, these different peaks may correspond to different structures within the

sample. It is unlikely that they are a consequence of a size distribution as this would not be expected to result in multiple peaks as the effect should be continuous.

The peak of Ca1 is at approximately 810 nm and Cs1 at approximately 680 nm, corresponding to respective sizes of 4.4 ± 0.1 nm and 3.8 ± 0.1 nm. The peak for Cs1 lies at a lower wavelength than that of Ca1, but considering the methods of fabrication it is Ca1 that has the potential to have the highest oxygen content. This suggests that the shift in this case is largely, if not entirely, due to the nanoscale of the structures, and potentially lends credence to the idea that the three peaks displayed by the oxygen terminated etched sample are due to different emission environments.

Clearly, any interpretations drawn from PL are necessarily tenuous because PL is indicative of the lowest energy level which results in radiative emission, while providing no indication whether this level corresponds to the bottom of the conduction band, surface states or is a result of oxidation. The following section details the results of TEM, which provides reliable size measurements as it allows direct observation of the sample.

4.2 TEM Results

Figures 4.5, 4.6, and 4.7 show TEM images of the etched, sol-gel, and colloidal (Ca1 and Cs1) samples, along with histograms of the particle sizes. The TEM of the etched sample corresponds to both oxygen and hydrogen terminated samples, as the oxygen terminated sample is a portion of the hydrogen terminated sample that was oxidised by exposure to air for two weeks.

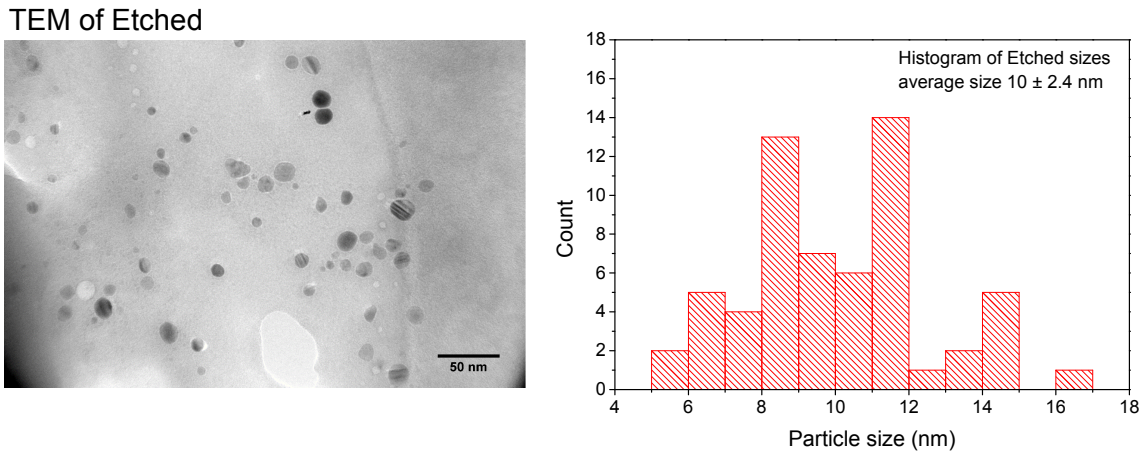

Figure 4.5: TEM image and corresponding histogram for the sample produced by chemical etching. The average particle size was determined to be 10 ± 2.4 nm from a random sampling of 60 nanoparticles.

Nanoparticles visible in the TEM micrographs were analysed, resulting in size values for 60 randomly selected nanoparticles for the etched, sol-gel, and colloidal samples. These values were compiled into the corresponding histograms, shown in the figures with the respective TEM micrographs. As can be seen in the figures this analysis found that the nanoparticles in the etched, sol-gel, Ca1, and Cs1 had average sizes of 10 ± 2.4 nm, 8 ±1.6 nm, 3.8 ± 0.8 nm, and 3.7 ± 0.6 nm respectively. The uncertainty quoted is the standard deviation of the particles measured.

TEM essentially allows one to see the nanoparticles directly and so is considered to be the most accurate method available to measure the nanoparticles size. Moreover, high resolution TEM can, in principle, provide direct structural information. However, we have been unable to obtain TEM data of sufficiently high resolution using an in-house TEM. Furthermore, high resolution TEM measurements are known to affect the structure of samples, especially in the case of nanoparticles [129]. Hence we use XRD to probe the structure in a non-invasive way, the results of which are detailed in the following section.

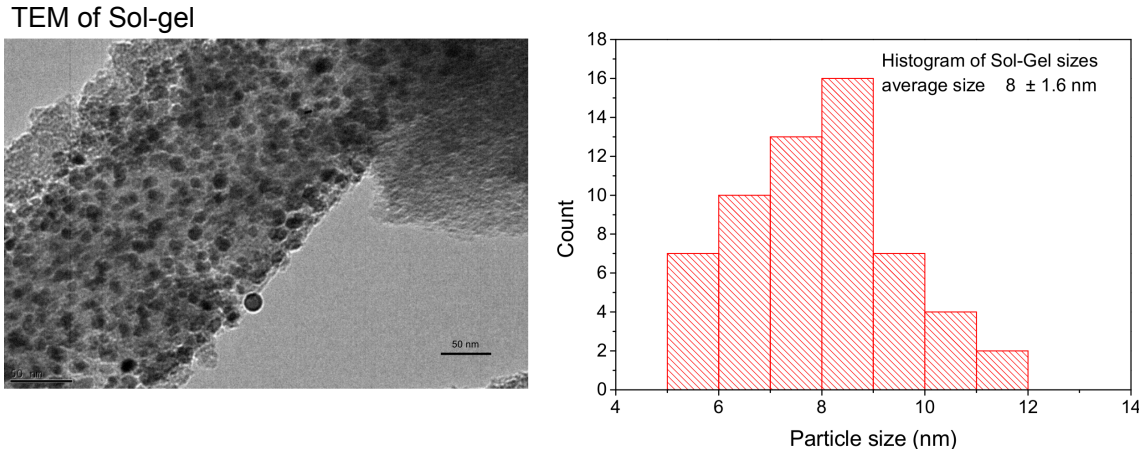

Figure 4.6: TEM image and corresponding histogram for the sample produced by sol-gel synthesis. The average particle size was determined to be 8 ± 1.6 nm from a random sampling of 60 nanoparticles

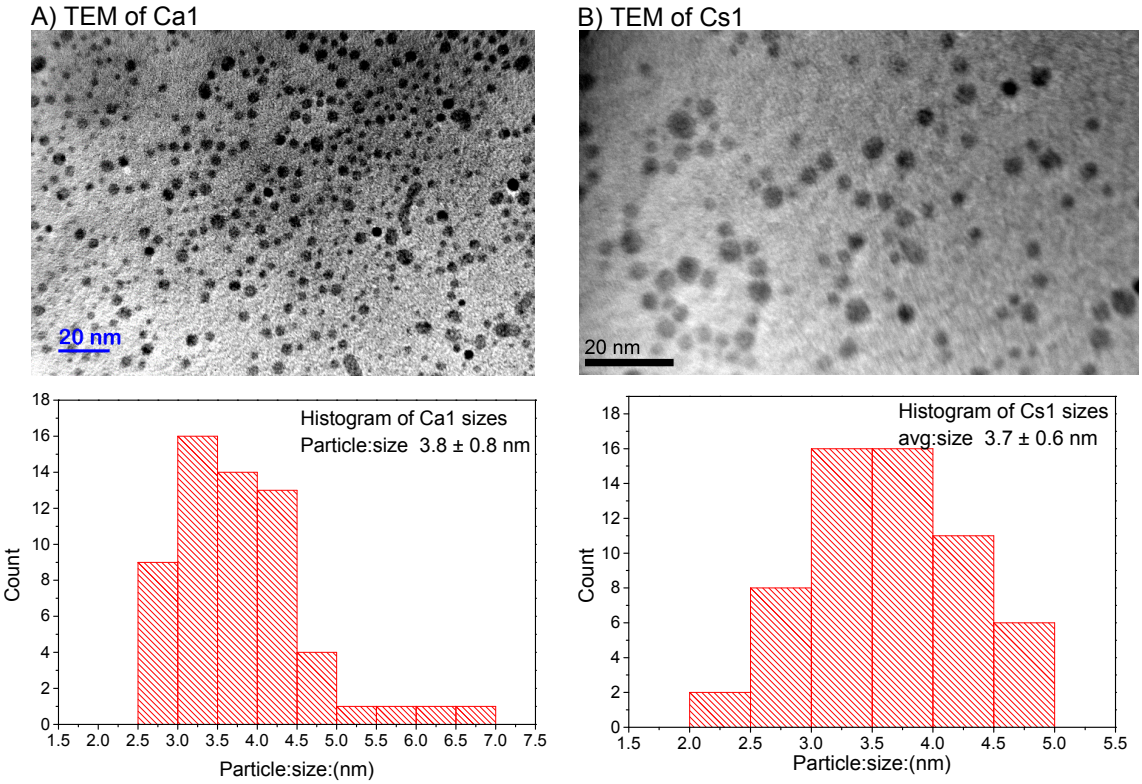

Figure 4.7: TEM images and corresponding histograms for the colloidally produced samples. Ca1 and Cs1 were found to have particle sizes of 3.8 ± 0.8 nm and 3.7 ± 0.6 nm respectively.

4.3 X-ray Diffraction Results

XRD data have only been collected for samples prepared by the colloidal synthesis routes due to limited beam time availability. At that point the colloidal synthesis route had shown itself to be the most effective method of producing Ge nanoparticles. The background-subtracted XRD spectra of the colloidally produced samples are shown in figure 4.8, with the spectrum for crystalline bulk Ge for comparison. Both Ca1 and Cs1 have a single broad peak centred slightly above and slightly below a 2θ value of 20°. The variation between the two peak positions is a result of not only differences in the samples (although this does play a part, as discussed below), but because different x-ray energies were used for each sample. As indicated on the graphs, 9500 eV was used for Ca1 and 8047 eV for Cs1.

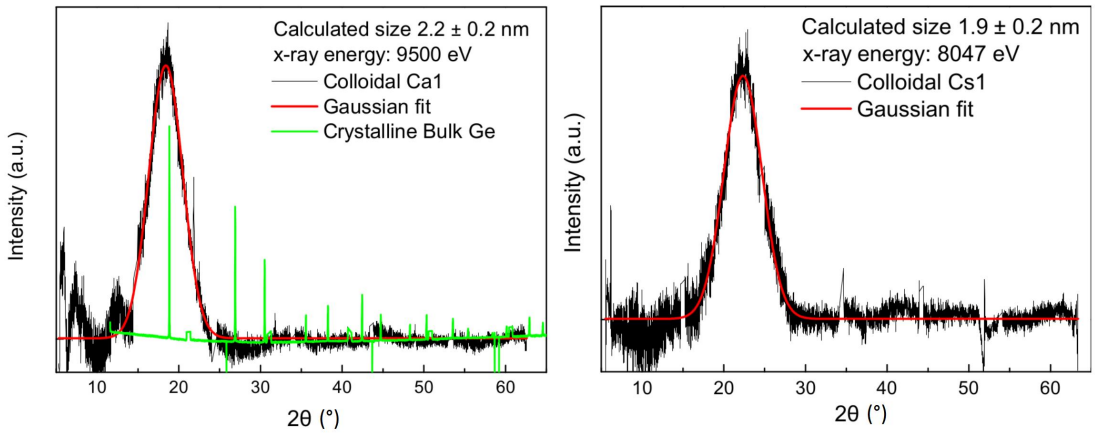

Figure 4.8: Background-subtracted x-ray diffraction spectra for the colloidally produced samples, Ca1 and Cs1. Using the Scherrer equation the particle sizes were found to be 1.6 ± 0.2 nm and 1.7 ± 0.2 nm respectively. The single broad peak is indicative of an amorphous sample. The XRD spectrum of bulk crystalline Ge is shown in green.

The single broad peak suggests that the colloidally produced samples may be amorphous. However, an amorphously broadened peak in Ge is expected to have a width of approximately 10-15°, given how little instrumental and temperature

broadening is present, as illustrated by the spectrum of crystalline bulk Ge spectrum in figure 4.8 [50, 130]. The peaks observed in figure 4.8 are only about 5°, half of what would be expected in amorphous Ge. XRD is a measure of long range order (correlations), and given the scale of the nanoparticles it is a distinct possibility that the observed broadening of the signal may be due to the small particle size, while the structure within them may indeed be crystalline (or partially crystalline). Size dependent broadening is described by the Scherrer equation [86], given in equation 2.11.

Figure 4.8 is the XRD spectra for the colloidally produced samples. The anomalies at 2θ values of approximately 15, 25, 35, 44, and 52 degrees correspond to gaps in the sensor array and are not indicative of actual peaks or a potentially problematic systematic error. The red lines in figure 4.8 are Gaussian peaks used to fit the data, the details of which are given in table 4.1.

	Ca1	Cs1
Centre (°)	22.351 ± 0.009	18.434 ± 0.007
FWHM (°)	4.66 ± 0.02	4.16 ± 0.02

Table 4.1: The parameters of the Gaussian fits of Ca1 and Cs1 in figure 4.8.

Using the Scherrer formula (equation 2.11), XRD determined the particle size in Ca1 to be 1.6 ± 0.2 nm, and in Cs1 to be 1.7 ± 0.2 nm. These results are larger than the lower size limit for this technique of 0.8 nm. The following section details the results of Raman spectroscopy experiments on the samples.

4.4 Raman Spectroscopy

Ambient pressure Raman spectroscopy, as described in section 2.1, was performed for the etched, sol-gel, and colloidally produced samples. The samples in figure 4.1 show a change in colour from the bulk Ge. This change in colour is the first evidence of possible size effects that result in changes of their optical properties making the colloidal samples suitable candidates for further investigation.

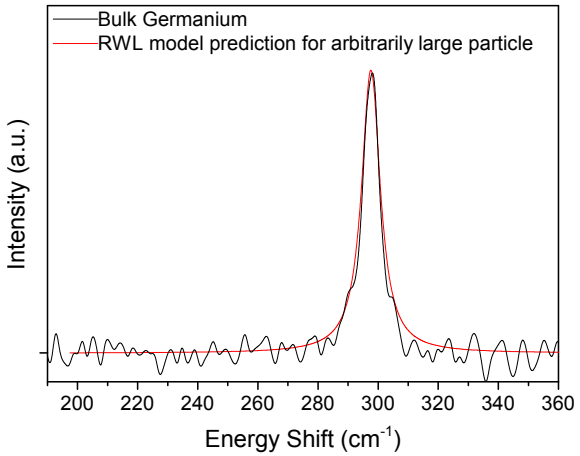

Figure 4.9: The Raman spectrum of bulk Ge at ambient pressure, exhibiting the characteristic narrow peak just below 300 cm^{-1}. The red line is fit to the peak based on the RWL model, discussed in chapter 3, for an arbitrarily large nanoparticle, here 300 nm.

The resultant spectra for the ambient Raman of the etched, sol-gel, and colloidally produced samples are shown in figures 4.10 and 4.11. The best fit of the Raman spectrum using the Richter-Wang-Ley (RWL) model is also shown on the graphs in red. Details of how the fit was performed can be found in Appendix A. The fit is based on matching the full width half maximum (FWHM) and the peak position of the data to the model. The average sizes of the nanoparticles obtained from the fits are shown in table 4.2. The Raman spectrum of bulk Ge fitted with the RWL model is shown in figure 4.9.

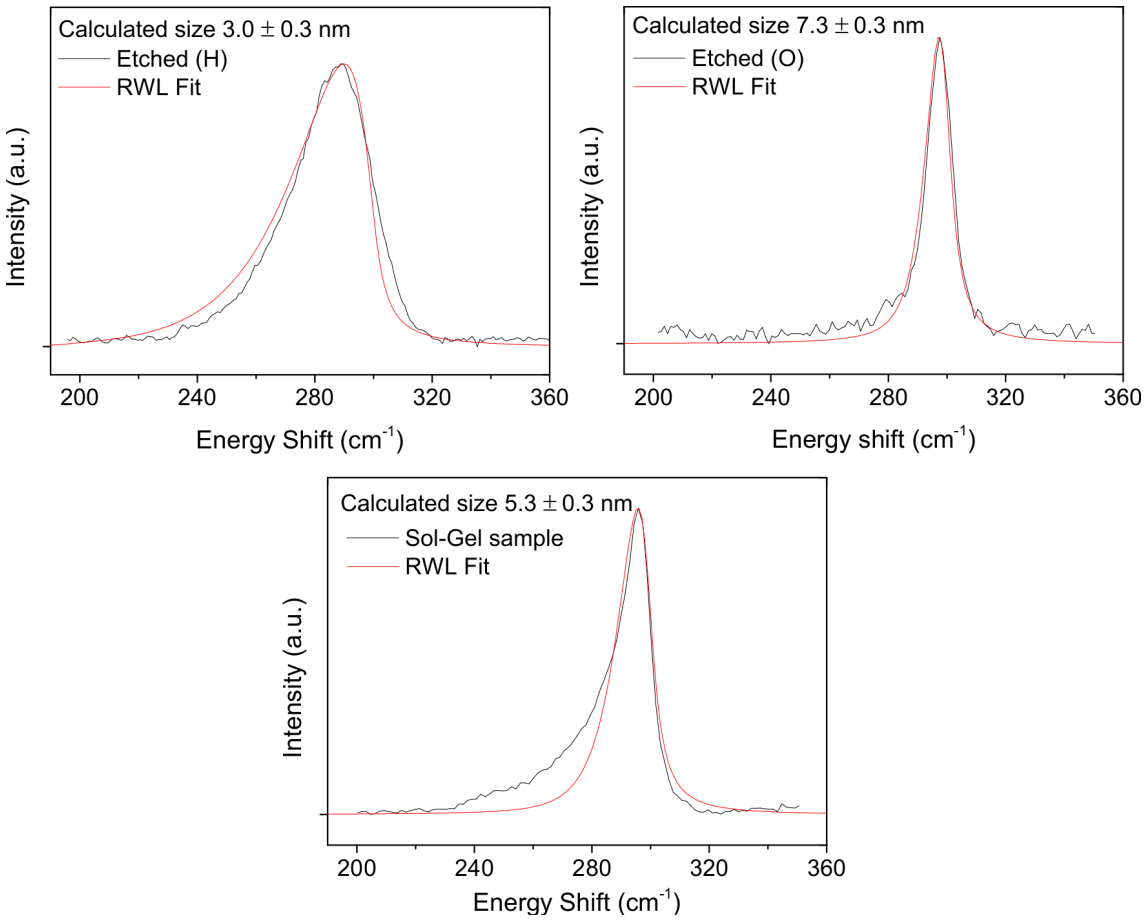

Figure 4.10: The Raman spectra for the etched and sol-gel samples fitted with the RWL model. Particle sizes of 3.0 ± 0.3 nm, 7.3 ± 0.3 nm, and 5.3 ± 0.3 nm were found to produce the best fit peaks for the hydrogen terminated etched sample, oxygen terminated etched sample, and sol-gel sample respectively.

Sample	Size (nm)
Etched H	3.0 ± 0.3
Etched O	7.3 ± 0.3
Sol-Gel	5.3 ± 0.3
Ca1	2.6 ± 0.3
Cs1	3.0 ± 0.3

Table 4.2: The average size of the nanoparticles in each sample as determined by the RWL model.

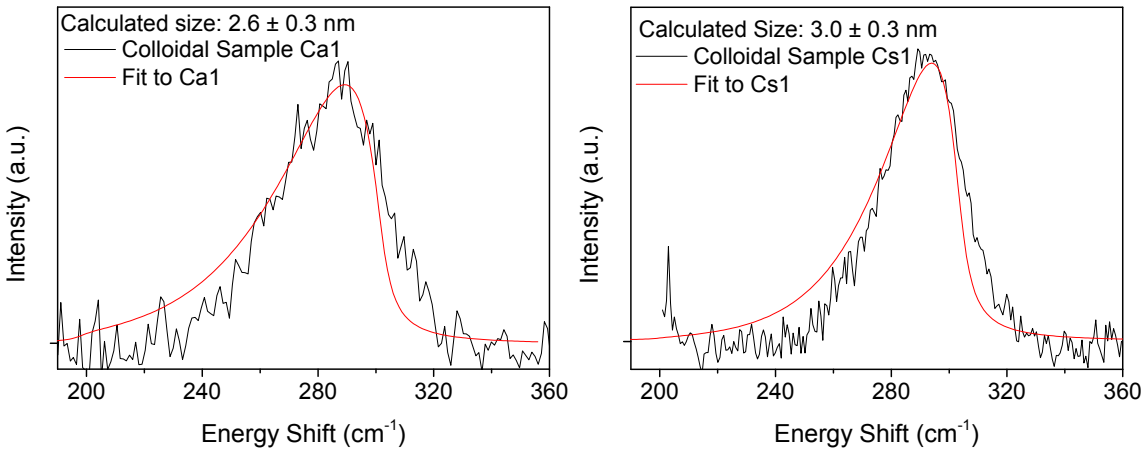

Figure 4.11: The Raman spectra for the colloidally produced samples fitted with the RWL model. Particle sizes of 2.6 ± 0.3 nm and 3.0 ± 0.3 were found to produce the best fit peaks for Ca1 and Cs1 respectively.

The spectra themselves show all the hallmarks of being from nanoscale materials; the peak is shifted to lower wavenumbers relative to the bulk value of 301 cm^{-1} [131], and the peaks have become clearly asymmetric. These two characteristic changes to the lineshape in the Raman spectra are a good indication for a sample to be of nanoscale size. Care must be taken, however, as asymmetric broadening can also be seen in amorphous samples [80].

The fits performed using the RWL model (described in chapter 3) appear to overestimate peak intensity at lower wavenumbers and underestimate it at higher wavenumbers (the obvious exception being the fit of the sol-gel sample). For the etched sample and for the high wavenumber side of the sol-gel sample these discrep-

ancies are small. They might even be considered to be on the order of experimental error considering the possibility of imperfect calibration and uncertainties in instrumental broadening. However the discrepancies of the lower wave number side of the sol-gel sample and both colloidal samples are too large to be written off as such. The small mismatch between the data and the model for most of the samples can be accounted for by the three dimensional dispersion model, as this is the most obvious omission from the adapted model (that is, the assumption of isotropy, detailed in section 3.4.4). However, while the three dimensional dispersion model does provide a clear improvement in fitting the Raman peak shape [123], it would probably not result in a significant improvement in size evaluation within the limits of our experimental error as the peak position and FWHM will be minimally affected.

Another possible explanation for the discrepancy is that we did not account for size distribution in our calculations. Nanoparticles produced via most routes are observed to have a log-normal distribution [132, 133, 134] and so tend to have a greater number of larger particles in the sample, if only for the reason that there is no upper limit to the size, while there will always be a lower limit for particle size. We tested the effect of particle size distribution and found that it does not result in a better description of the peak shape. It does, however, lead to increased correlation between parameters during the fitting, and thus increased errors in size evaluation. Consequently this may lead to a systematic underestimation of the size of the particles in the sample.

The sol-gel sample fit has the opposite discrepancies, underestimating at lower wavenumbers and slightly over estimating for higher wavenumbers. Considering the size distribution from TEM for this sample, it is highly unlikely that the low wavenumber discrepancy is due to a contribution from small particles as particles

small enough to contribute significantly at those wavenumbers are absent from the sample. The signal from the amorphous component is another possibility for the discrepancy. The possibility of the presence of an amorphous component in embedded nanoparticles has been previously reported [46], where it was shown using EXAFS analysis that an amorphous layer was formed between the Ge nanoparticles and the SiO_2 matrix.

The average particle sizes determined by each technique are summarised in table 4.3. There are clearly some discrepancies in the sizes calculated by different techniques for the same sample, in many cases beyond the range of experimental error. This can be attributed to the specific natures of the techniques and the different properties of samples that they probe as discussed earlier. Consequently these discrepancies are indicative of possible complex morphology of the samples and can be used to obtain details about the structure of the nanoparticles themselves. Uncertainties in TEM measurements are from the half width half maximum of the corresponding size distributions. Uncertainties in PL and XRD measurements come from uncertainties in the PL and XRD peak positions. Uncertainties in Raman measurements come from uncertainties in the fitting of the Raman peaks.

	Determined size (nm) for				
Technique	Etched-H	Etched-O	Sol-Gel	Ca1	Cs1
	4.3 ± 0.1	3.9 ± 0.1	3.8 ± 0.1	4.4 ± 0.1	3.8 ± 0.1
PL		3.5 ± 0.1	3.4± 0.1		
		3.2 ± 0.1			
TEM	10 ± 2.4	10 ± 2.4	8 ± 1.6	3.8 ± 0.8	3.7 ± 0.6
XRD				1.6 ± 0.2	1.7 ± 0.2
Raman	3.0 ± 0.3	7.3 ± 0.3	5.3 ± 0.3	2.6 ± 0.3	3.0 ± 0.3

Table 4.3: A summary of the average sizes of the nanoparticles in the samples as determined by the experimental techniques outlined in this section. There are discrepancies between the direct measurement of TEM, the less direct XRD, and indirect Raman.

For the hydrogen terminated etched sample TEM gives a size of 10 nm while Raman gives a size of three nm, which is clearly a discrepancy. If the nanoparticle were entirely crystalline then the size from Raman would be expected to be the same as that from TEM. The fact that Raman measurements suggest a smaller size than TEM indicates that the particles may not be wholly crystalline. The difference between these techniques is that Raman is sensitive to atomic structure while TEM performed at the resolution reported here can only provide an accurate measure of the nanoparticle size. This discrepancy suggests that there is a crystalline component to the nanoparticles, but it is small. This could be a result of either a small crystalline component in each nanoparticle, or the presence of small crystalline and larger amorphous nanoparticles. There is also the possibility that the objects seen in the TEM images are themselves porous structures containing smaller nanoparticles. However, we have not been able to identify such smaller substructures in our TEM measurements.

The oxygen terminated etched sample also shows discrepancies in size analysis from various techniques, though to a lesser degree. The size from TEM is 10 nm while the size from Raman is 7.3 nm. A smaller discrepancy may be a result of recrystallisation of the amorphous component during the oxidation process.

The sol-gel sample once again shows similar discrepancies. The size from TEM is eight nm, larger than the size from Raman which is 5.3 nm. This again indicates that the nanoparticles may be amorphous with a smaller crystalline component. Also, the possibility of a porous structure for this sample is far less likely than for that of the etched sample. Firstly their appearance is very regular, all the particles are essentially spherical. Secondly, their method of production effectively precludes it. The nanoparticles were produced by growing them from a nucleus through diffusion

and so it is a bottom-up method (unlike etched which is top-down). The result of this is that there is much more likely to be amorphous content within the particle than for it to be a porous structure.

The colloidally produced sample Ca1 is significantly smaller under TEM than both the etched and sol-gel samples. The size from TEM for Ca1 was 3.8 nm with the size from Raman being 2.6 nm. This represents the smallest discrepancy between TEM and Raman seen so far. However, the measurements still don't agree within experimental error and the implication now is that the sample is mainly crystalline with a smaller amorphous content. This sample is almost certainly not a porous structure considering both the similarity in the calculated sizes and the production method which, as sol-gel, is bottom-up. Unlike the previously discussed samples, XRD was performed for Ca1. XRD data give a smaller size than Raman, and is good evidence that there is a crystalline component to the sample as diffraction is highly structurally dependent. The conclusion for this sample is that the nanoparticles consist of both crystalline and amorphous structures.

The colloidally produced Cs1 exhibits largely the same characteristics as Ca1, though by different magnitudes. There is a smaller discrepancy between sizes from TEM and Raman, and a larger one between Raman and XRD. Hence the conclusion is the same, that these nanoparticles are crystalline with amorphous content, and not porous structures.

The general tendency for all samples is thus similar, as TEM measurements result in larger particle sizes than any other method. The most direct technique employed was the TEM as it allows direct visual observation of the nanoparticles, without relying on any assumptions. As such it is an excellent benchmark to use

as a comparison for the other measurements. The TEM measurement is essentially an upper limit, and anything exceeding it must indicative of an inadequacy in an underlying model of structure and/or morphology of the nanoparticles.

The second most reliable technique is XRD, as it is a direct probe of the atomic structure of samples. However, the size analysis is based on the Scherrer equation and provides an "effective" size assuming a crystalline region and does not take into account broadening due to structural disorder. The size obtained from this technique is indicative of the size of the crystalline portion of the nanoparticle. For both colloidal samples on which XRD was performed, the size was found to be about half that of the value found by TEM. This suggests that while the nanoparticles may not be completely crystalline, they are not wholly amorphous either. If the particles were completely crystalline then the calculations of size from the Scherrer equation would be expected to be consistent with the observed size from TEM. If the particles were completely amorphous the Raman peak would be expected to have an energy shift of 275 cm^{-1} at most (as in figure 2.5), and more likely lower due to nanoscale effects, but all Raman peaks have energy shifts greater than 280 cm^{-1}.

The size determined by PL is based on a model and so it is an indirect method and can only ever be as accurate or applicable as the model itself. Using PL to evaluate particle size is based on the quantum confinement effect and the related theory described in section 1.3 and on the assumption that PL is due to recombination across the band gap of a corresponding crystalline structure. The nanoparticle size calculated from the PL for both colloidal samples is significantly larger than the size of the crystalline region determined by XRD. It is also larger than the size found by TEM, though they agree within experimental error. This is indicative of the fact that PL is the least reliable method for size determination as it relies on an

assumption of precise knowledge of the nature of the light emission. For the larger etched and sol-gel nanoparticles the size from PL is within the expected range, in the absence of any XRD data. It is possible then that the emission in the larger particles is representative of size, but considering that this cannot be the case in the smaller colloidal nanoparticles, this is deemed unlikely. However, it can be said with confidence that the peaks from 550 nm to around 650 nm in figure 4.3 are a result of emission from oxidised Ge. The other peaks could be from a crystalline or amorphous region in the particles, or from interface states of the nanoparticles between the nanoparticle proper and the oxide layer on the surface. This can only be speculative as without a good model and further experimental work (e.g. a combination of PL, absorption, and photoluminescence excitation (PLE)) it is difficult to determine anything more specific. This combination allows the correlation of features in the absorption spectrum with the information on the energy levels directly contributing to PL and thus to link indirectly (e.g. through modelling) the light emission and atomic structure responsible [135, 136, 137].

The size from Raman is also based on a model and so it is also an indirect method. The peak corresponds to a broadened and shifted bulk crystalline Raman peak. This is supported by the fact that XRD indicates that there is a crystalline component to the structure. The fact that the size from Raman is greater than that from XRD is due to the Raman method measuring more than just the crystalline part of the structure. This reflects the nature of the technique in that it is a probe of vibrational character and in small or disordered samples can also probe the vibrational density of states. However, it is also possible that there are amorphous regions within the sample, whose contribution to the Raman spectrum could further broaden the spectrum independently of size effects, purely as a consequence of

structural effects. This could lead to the size determined by the RWL model to be overestimated compared to XRD.

This uncertainty between amorphous particles and a crystalline-amorphous mix model can be resolved by studying the Raman spectrum when the samples are subjected to high hydrostatic pressure. The differences in the transition pressures of the two phases of Ge (amorphous Ge has a phase transition at $\sim$ 6 GPa [99] and crystalline Ge at $\sim$ 11 GPa [100], under hydrostatic compression) make this an ideal technique for distinguishing between phases. The pressure induced phase transition results in the Ge sample transforming into a metallic phase, resulting in the loss of Raman signal. Thus one can hope to distinguish between amorphous and crystalline samples by noting at which pressure the Raman signal is lost. In nanoparticles consisting of both amorphous and crystalline components the Raman signal would be expected to be persistent at significantly higher pressures than if the nanoparticles were purely amorphous. However, one would expect a narrowing of the Raman peak with pressure increase above the value for transition in an amorphous phase due to an increase in sample crystallinity. The results of high pressure Raman spectroscopy are discussed in the following chapter.

Chapter 5

High Pressure Raman Spectroscopy Results and Analysis

5.1 High Pressure Raman Experimental Results

High pressure Raman experiments were conducted as described in section 2.6. The sol-gel sample was not studied under pressure due to the presence of the SiO_2 matrix, which excludes the possibility of hydrostatic compression. The visual appearance of Cs1 under various pressures is shown in figure 5.1 and is typical of the visual behaviour of all samples studied. As pressure is increased a black spot develops in the middle of the sample. The spot contains nanoparticles that have undergone a transition to an opaque phase at around 14 GPa. The appearance of the black spot approximately at the centre and its outward growth with pressure is expected as this follows the pressure profile of DACs, where the highest pressure in the middle, decreasing towards the edges [138, 139]. Ruby photoluminescence and Ge Raman

measurements were taken midway between the centre and the edge, approximately where the left edge of the dark circle is in the 24 GPa image in figure 5.1. Both [138] and [139] show that the pressure in the centre can be 30-40% higher than at the midpoint by compressing a piece of metal between diamonds. This, of course, is not the case under hydrostatic compression. However, above around seven GPa the methanol-ethanol mixture used as a pressure transmitting medium is a solid and is no longer trully hydrostatic [140]. Therefore, one would expect a pressure profile to develop with the pressure being slightly higher in the middle of the DAC. It is clear that nanoparticles in the centre transform first, and this is because of the pressure profile of the cell. This demonstrates how important it is to take Raman measurements from the same area of the cell as the ruby fluorescence in order to ensure accurate pressure values.

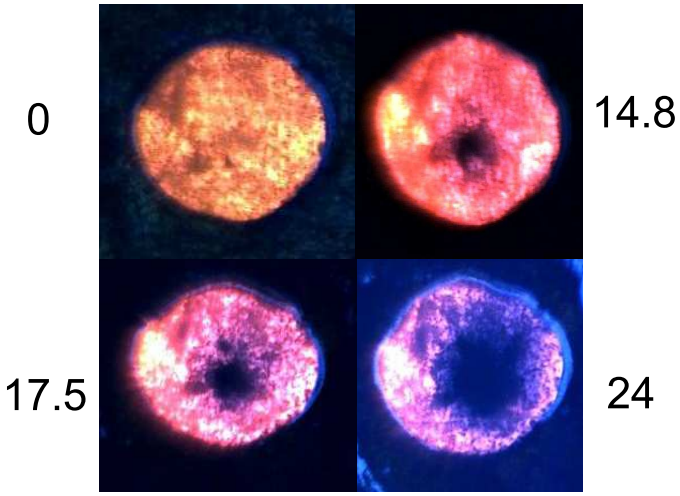

Figure 5.1: The visual appearance of Cs1 nanoparticles under a microscope at the indicated pressures in GPa. The dark spot in the centre present at higher pressures is the area of the nanoparticles that have transformed to an opaque phase. Given the pressure profile of a DAC this pattern is expected as the pressure in the centre is highest.

The experimental results can be seen in figure 5.2. Figure 5.2(a) shows the Ra-

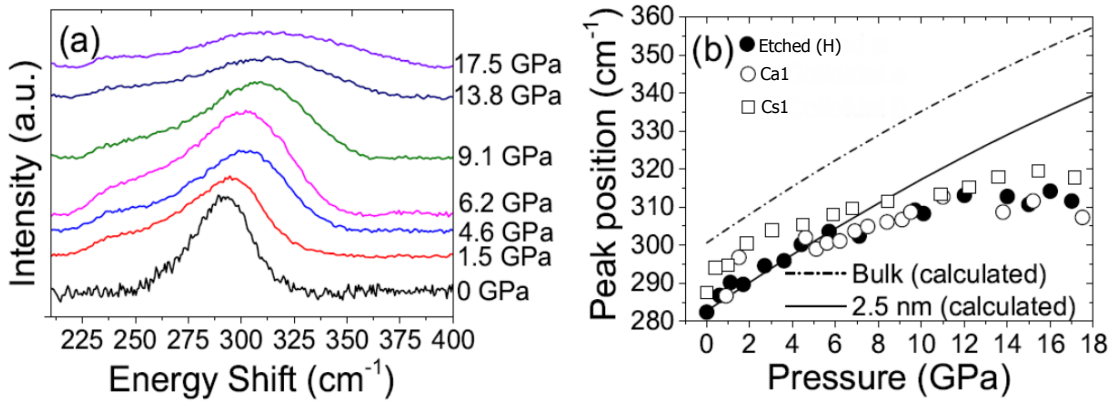

Figure 5.2: Experimental results of high pressure Raman experiments, starting at ambient pressure and rising to 17.5 GPa. (a) shows stacked Raman spectra for Cs1, (b) shows the peak position against pressure, with the bulk expectation (extended as a guide to the eye). The shift calculated by the modified RWL model for a 2.5 nm nanoparticle is included for comparison.

man spectra collected at the pressures indicated for sample Cs1. Most conspicuously, the signal is still present not only well above the amorphous transition pressure ($\approx$ six GPa), but also well above the bulk transition pressure ($\approx$ 11 GPa). The signal can still be distinguished up to $\sim$ 18 GPa. As the pressure is increased the Raman spectrum is seen to shift to higher wavenumbers, broaden, and reduce in intensity. This is the observed behaviour for all samples subjected to high hydrostatic pressure. Both the shift to higher wavenumbers and the broadening are observed behaviours for bulk crystalline Ge. These effects are sufficiently well understood that they may be incorporated into the RWL model to allow for them. This is demonstrated in section 5.2.

Figure 5.2(b) shows the peak position of the Raman spectra against the applied pressure for the etched and colloidal samples, and what is expected from the bulk. While the peak shift to higher wavenumbers was expected, the rate of change of the peak position at high pressures observed in both the etched and colloidal samples is significantly different from that of the bulk.

In an effort to better understand these results the RWL model has been adapted to include pressure dependencies, detailed in the next section.

5.2 Model of Raman Spectroscopy Under High Pressure

To facilitate a more thorough analysis of the results of Raman measurements taken under pressure a theoretical model has been developed which calculates the expected Raman spectrum for a sample with a given average size and a given applied pressure. The model is based on the RWL phonon confinement model described in chapter 3, the Murnaghan equation of state has been used in conjunction with fits to empirical data of the bulk pressure response to incorporate the expected effects of pressure on the nanoparticles. Details of how these were used to modify the expression and the expected effects are detailed in the following sections.

The Murnaghan Equation of State

The Murnaghan equation of state (MES) is typically written as

$$P(V) = \frac{B_0}{B_0'}\left[\left(\frac{V}{V_0}\right)^{-B_0'} - 1\right], \tag{5.1}$$

where P is the applied pressure, V is the material volume, B_0 is the bulk modulus, and B_0' is the pressure derivative of the bulk modulus. The MES describes the relationship between the volume of a material under a given pressure in terms of the bulk modulus [141]. For the purposes of this work, assuming spherical nanoparticles,

the MES can be rewritten in terms of the nanoparticle size and the lattice parameter as follows:

$$d(P) = d_0 \left(PB_0'/B_0 + 1\right)^{-1/3B_0'}, \tag{5.2a}$$

$$a(P) = a_0 \left(PB_0'/B_0 + 1\right)^{-1/3B_0'} \tag{5.2b}$$

where $d(P)$ and $a(P)$ are the particle size and lattice parameter under applied pressure, a_0 is the lattice parameter at ambient pressure, and d_0 is the particle size at ambient pressure. The lattice parameter in the expression for the phonon dispersion curve and the particle size enters the RWL expression via the confinement function.

Equation 5.2a shows that applied pressure will result in the size of the particle being reduced. As seen previously a smaller particle results in a greater shift of the Raman peak. However this considered the nanoparticle to get smaller by reducing the number of atoms within it. The Grüneisen parameter, γ, correlates the change in phonon frequency to a change in size for a constant number of atoms. The Grüneisen parameter is given by

$$\gamma_i = -\frac{V}{\omega_i}\frac{\partial \omega_i}{\partial V}, \tag{5.3}$$

where V is the volume and ω_i is the phonon frequency. Bulk Ge has a Grüneisen parameter of 0.96 ± 0.05 for the LO phonon at the Γ point [142]. The positive value implies that as the volume is reduced the phonon frequency is expected to increase. Indeed, as shown in figure 5.2, the Raman peak moves to higher energy shifts.

Equation 5.2b shows that applied pressure will result in a reduction in the lattice parameter. This essentially makes bonds shorter and stiffer. The basic principles of Raman spectroscopy lead to the conclusion that this will result in the peak becoming narrower and shifting to higher frequencies. The result of this is that a reduction in the lattice parameter (and therefore bond length) and volume (and thus the effect of the size) have an opposite effect on the Raman frequency, but essentially cancel each other out (see Appendix B).

Pressure Dependent Phonon Dispersion Curve

The second amendment made to the RWL model was to incorporate a pressure dependence into the expression for the phonon dispersion curve. The fit to the dispersion curve found in Das [143] is a sufficiently close match for our purposes. Das *et al* find the phonon dispersion ω_q to be described by

$$\omega_q = [\omega_0 - 104(qa/2\pi)]^2. \tag{5.4}$$

This expression is dependent on the lattice parameter and so can be rewritten in terms of pressure using the MES, like so:

$$\omega_q(P) = \left\{ \omega_0(P) - 104 \left[\frac{q}{2\pi} a_0 \left(\frac{B_0'}{B_0} P + 1 \right)^{-1/3B_0'} \right] \right\}^2 . \tag{5.5}$$

Incorporating The Bulk Pressure Dependence

Another key aspect that needs to be included is the bulk response to increased pressure. This has been measured empirically by Olego *et al* in [144]. They found

that the peak position of the Raman spectrum for the TO mode in bulk Ge to be dependent on the applied pressure according to

$$\omega_q = (300 \pm 0.5) + (1027 \pm 10)\frac{-\Delta a}{a_0}\,\mathrm{cm}^{-1}, \tag{5.6}$$

where Δa is the change in the lattice parameter as a result of the applied pressure. From figure 5.2 it is clear that the Raman peak position for bulk Ge increases with pressure up to at least 11 GPa. Bulk Ge undergoes a phase transition at around this pressure and no longer exhibits this particular phonon peak so measuring beyond it is impossible. However, for the sake of comparison, calculations based on it can be extended beyond the value of the bulk transition pressure.

While being useful, this expression is not as flexible as the previous two modifications (the MES and the pressure dependent phonon dispersion curve) as it is only stated in terms of the change to the lattice parameter. By recognising that $\Delta a = a_0 - a$ and using the MES, ω_q can be rewritten as a function of pressure and the bulk modulus as

$$\omega_q = (300 \pm 0.5) + (1027 \pm 10)\left(1 - \left[\frac{B_0'}{B_0}P + 1\right]^{-1/3B_0'}\right)\,\mathrm{cm}^{-1}. \tag{5.7}$$

Incorporating this into the RWL model is expected to lead to the Raman peak shifting to higher wavenumbers as the applied pressure increases, following the same pattern as is observed in the bulk pressure dependence. The alternative fit made by

Olego *et al* in terms of pressure rather than lattice parameter as

$$\omega_0 = (300.6 \pm 0.5) + (3.85 \pm 0.05)P - (3.9 \pm 0.6)10^{-2}P^2\,\mathrm{cm}^{-1} \tag{5.8}$$

shows clearly that there is a strong positive linear component and a weakly negative quadratic component. This will lead to the peak position shifting to higher wavenumbers with pressure.

The Pressure Dependent Phonon Confinement Model

Using equations 5.2, 5.5, and 5.7, the original RWL model can be rewritten to include a pressure dependency

$$I(\omega, P, B_0) = \int_0^{2\pi/a(P)} \frac{\exp[-(qd(P,B_0)/4\pi)^2]a(P,B_0)\pi q^2}{(\omega - \omega_q(P))^2 + (\Gamma_0/2)^2}\mathrm{d}q. \tag{5.9}$$

With the exception of the lattice parameter and size effects, these processes are expected to operate on the signal independently. In the following section the results of this adapted model are compared with the experimental results to gain a greater understanding of the unusual exhibited behaviour.

5.3 Comparing Experimental Results to The Adapted Model.

The experimental results plotted alongside results calculated from the adapted RWL model are presented in figure 5.3. Figure 5.3(a) shows the experimental Raman

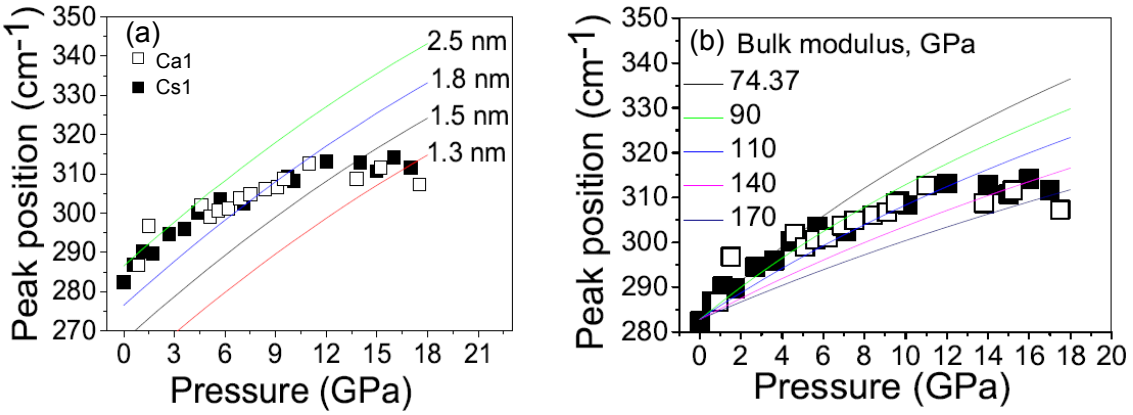

Figure 5.3: Panel (a) shows the experimental Raman peak positions plotted against pressure compared to that calculated for various size nanoparticles. Panel (b) shows the experimental Raman peak positions plotted against pressure compared to that calculated for a 2.5 nm particle with various stated bulk moduli.

peak positions plotted against pressure with the peak positions for nanoparticles of various sizes, indicated on the graph. Figure 5.3(b) shows the same data plotted with the calculated peak positions for 2.5 nm nanoparticles with various bulk moduli (indicated on the graph) to account for the possibility of a size dependence of the bulk modulus [65, 66].

Figure 5.3 shows that the samples exhibit a strongly nonlinear pressure dependence of the Raman peak position as compared to both bulk data [144] and our calculations. Moreover, the deviation of the Raman signal from the bulk behaviour can be observed well below the expected structural transition ($\sim$ 11 GPa) for bulk Ge. Therefore the observed dependence of the peak position on applied pressure cannot be simply related to a structural evolution in diamond-type Ge QDs with the bulk modulus corresponding to bulk Ge.

One possibility for the deviation from the bulk dependence could be due to a size-dependent increase in bulk modulus. There is currently an ambiguity regarding the size effect (on the nanoscale range) on the bulk modulus of materials in general.

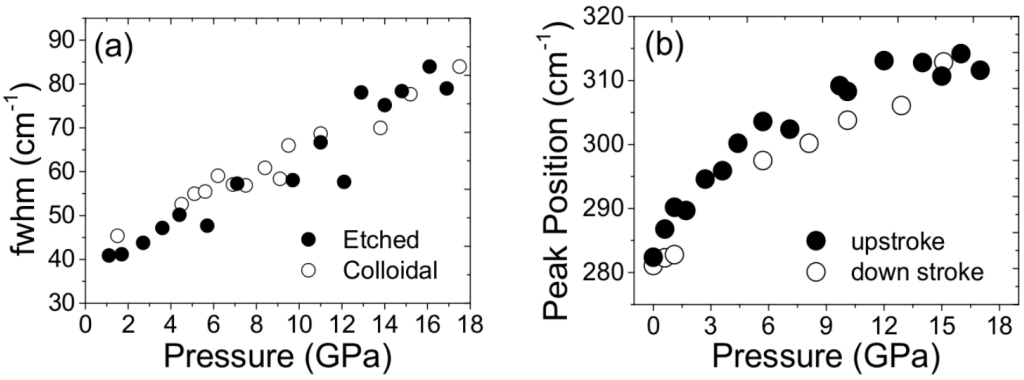

Figure 5.4: (a) the FWHM vs. pressure shows a consistently linear trend, in contrast to that of the bulk which barely changes. (b) The peak position vs. pressure for increasing and decreasing pressure on Cs1. The lack of hysteresis suggests there is no sudden structural change.

For Ge, computer simulations indicate a bulk modulus of 84 GPa for 1.5 nm particles [65], while XRD experimental data suggests a value as high as 112 GPa for 13 nm particles [66]. We used a variety of bulk modulus values to find the most appropriate for our system. We used equation 5.5 to calculate the effect of the value of the bulk modulus on pressure induced Raman shift for 2.5 nm QDs. One can see in figure 5.3(b) that none of the curves fit the full data range satisfactorily, with the best fit range lying between 90 GPa and 110 GPa.

Figure 5.3(b) shows that none of the curves generated by varying the bulk modulus adequately fit the data. The discrepancy could be intrinsic to the samples or related to the specifics of the application of single wavelength Raman to the nanoparticles. It's possible that in an amorphous sample under compression above six GPa larger particles start to transform and the particle distribution shifts towards smaller sizes and hence the Raman peak shifts towards lower wavenumbers. However, we do not observe any visual changes to the sample (or see any other

Raman signal) up until 14.8 GPa that would indicate an onset of such a transformation. Another possibility is that there is a change in the nature of the sample as pressure is raised. Clearly, the peak corresponding to the diamond-type structure is preserved, so the changes must take place within that structure. Figure 5.4(b) shows the peak position against pressure as the pressure is ramped up and down again. The lack of any significant hysteresis indicates that there is no sudden phase change during the process. From this it is clear that there is no phase transition occurring that could account for the observed non-linearity. We also do not expect any laser absorption resonance effects to be significant, as the laser excitation energy is smaller than, and energetically separated from the observed and theoretical band gap. Thus any change in the electronic structure cannot drive the larger (or smaller) sized particles into resonance and not others, and rules out electronic origins of this effect. In order to examine this further we looked at the FWHM of the Raman peak as a function of pressure.

Figure 5.4(a) shows the pressure evolution of the FWHM of the Raman peaks for etched and colloidal samples. The significant change in peak width as a result of increased pressure can be interpreted within the phonon confinement model as a significant decrease in particle size. This could be achieved in two ways, either the pressure is compressing the particles, or the relative contribution from smaller particles increases with pressure. The FWHM is useful in addressing the first possibility as compression of the particles is predicted to be less strongly coupled to increasing pressure. This is a consequence of the interaction of the pressure effects on the lattice parameter and size, further explained in Appendix B.

A reduction in particle size as a result of hydrostatic pressure dramatic enough to see such a significant change in the FWHM is inconsistent with the data for bulk

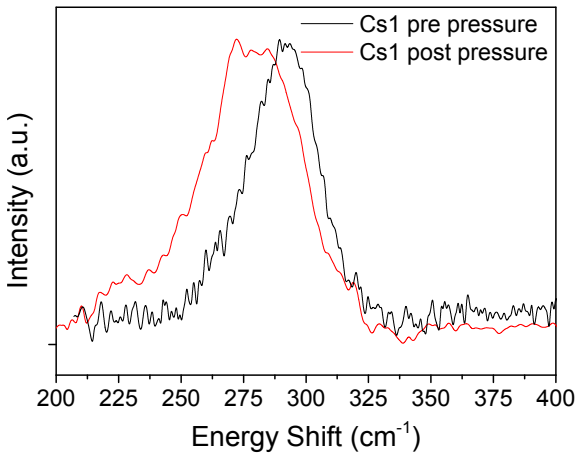

Figure 5.5: The ambient pressure Raman spectra of Cs1 before (black) and after (red) the application of pressure. The shifting and broadening of the peak suggests has undergone pressure induced amorphisation and not fully recovered.

Ge. Bulk Ge is observed to have a FWHM broadening of less than 0.5 cm^{-1} from 0 to 10 GPa [145]. Figure 5.3(a) shows that a diameter change of almost 50% would be necessary if this was the mechanism responsible for the observed behaviour. Such a dramatic size change is impossible, as the size change for the bulk at 17 GPa would not exceed 5%.

The observed FWHM pressure dependence is consistent with an increase in the degree of structural disorder in the samples. Amorphisation would lead to increased peak width and is also expected to lower the Raman frequency (as in figure 2.5 in section 2.1). If the degree of disorder should increase under pressure this would further lower the Raman frequency, leading to a non-linearity, which is consistent with the Raman data in figure 5.3. This suggests that the sample may not be entirely amorphous initially. This interpretation is further supported by the onset of a shoulder (between 225 and 250 cm^{-1}) in the Raman spectrum when pressure is applied, and its relative increase in intensity with increasing pressure as seen in figure 5.2(a). This behaviour is consistent with an amorphous contribution. The

observation that the shoulder height increases relative to the main peak supports the idea of an increasing amorphous component. This conclusion is further corroborated by figure 5.5, which shows a comparison of the Raman spectra for colloidal sample Cs1 before and after the application of hydrostatic pressure. After pressure is applied and removed the spectrum is shifted to a lower wavenumber, has a broader FWHM, and has a shoulder at ~ 225 cm^{-1}. These are all hallmarks of an amorphous sample, suggesting that the sample undergoes amorphisation under pressure and does not fully recover once the pressure is removed.

Based on the amorphisation hypothesis, a scenario that fits the data is one that involves amorphisation driven by the surface disorder as pressure is increased. This scenario is exactly what has been observed in density functional theory (DFT) simulations of pressure effects in small Si QDs [146]. This model of structural evolution suggests that two regions can be identified in the pressure dependence of the Raman frequency in figure 5.3. The first region extends up to around $12 - 14$ GPa and involves gradual amorphisation of the nanoparticles. This is followed by an onset of a transition to possibly a metallic state as evidenced by the optical transmission data and loss of Raman signal above $\sim$18 GPa.

Thus with the aid of high pressure measurements we suggest that the most adequate structural model for our samples is that of the core-shell, with a crystalline core and a disordered outer shell. In order to further understand the structure of the samples and the origins of the light emission we conducted transmission XAS and OD-XAS measurements. The results of this work are presented in the next chapter.

Chapter 6

XAS and OD-XAS Results and Analysis

The XEOL signals at 11 keV for all samples are shown in figure 6.1. One can see that XEOL emission spectra are quite different from their corresponding PL spectra given in section 4.1. Most obviously, emission below 450 nm can be clearly observed due to high energy (short wavelength) x-ray excitation. The signal below 450 nm is due to light emission from the silica and glass capillaries all samples were loaded into (except for the hydrogen terminated etched sample which was deposited onto kapton tape). The signal profiles above 450 nm are also different in all cases except perhaps the hydrogen terminated etched sample. However, even in the latter case the PL peak is located at around 690 nm (vs 773 nm in the PL spectrum). The shift in the peak position is not unexpected [147] and is due to the low temperature (T = 100 K) used in the XEOL experiments. Furthermore, the rate of temperature-dependent PL shift is different for Ge and GeO_2 (as demonstrated in [148]) which results in the change of the overall signal shape.

Since we are interested in the origins of emission due to pure Ge, the XEOL window at around 700 nm (shaded area) was chosen for OD-XAS measurements. As was the case with PL, the signal at and around 530 nm most likely corresponds to light emitted by GeO_2, and the signal at around 700 nm to pure Ge and is the result of quantum confinement. This is backed up by table 1.11 which shows that PL is expected to be in the NIR range. The only peak observed in the NIR range is in the etched H sample at 700 nm. Consequently the OD-EXAFS measurements have been carried out around 700 nm (as indicated by the red box in figure 6.1) so that the signal will be from the region we are principally interested in, the site where pure Ge is thought to contribute to the light emission.

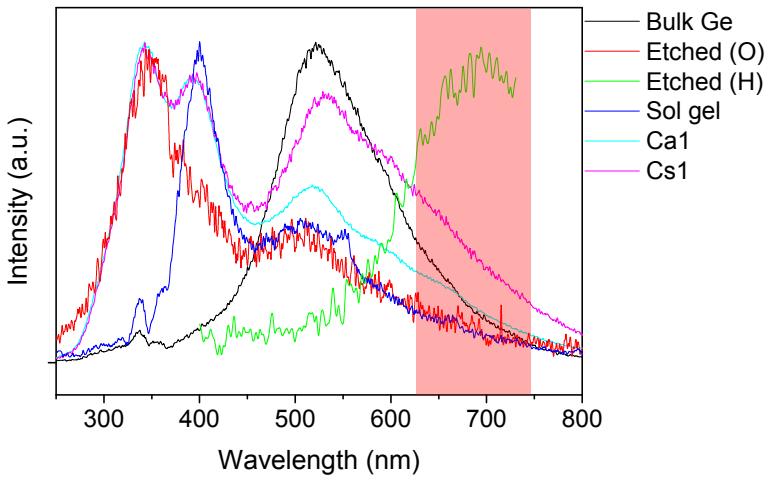

Figure 6.1: The XEOL spectra of all samples. OD-EXAFS collection was centred on 700 nm as indicated by the red bar.

XAS and OD-XAS data were collected at the Ge K-edge ($\sim$ 11 keV). The magnitude of the Fourier transform of the XAS spectra for etched, sol-gel, and colloidal nanoparticles are shown in figure 6.5. The magnitude of the Fourier transform of the OD-XAS spectra for etched and sol-gel samples are shown in figure 6.6. The OD-XAS spectra and their derivatives for both colloidal samples are shown in figure 6.7 with the spectra and derivatives of the XAS for comparison. The magnitude of

the Fourier transform for the colloidal samples is not shown as the spectra could only be collected up to $\sim$ 11.3 keV because of an inadequate signal to noise ratio due to low XEOL output. The reduction in the extent of the spectra results in a Fourier transform with uncertainties so large that they cease to be useful for further structural analysis. However, the near edge fine structure can still be useful as we shall see later. The corresponding EXAFS functions and theoretical model fits are shown in figures 6.2, 6.3, and 6.4. We used bulk Ge as a reference to fit the amplitude factor (equation 2.13). We also used bulk Ge to fit θ_D within the Debye model to calculate and set values of RSMD of the atoms. Diamond type Ge was used as a model structure for calculating theoretical EXAFS spectra. Thus only interatomic distances were refined, which are given in table 6.1

The unfitted ODXAS spectra are shown in Appendix E.

Sample	Peak Position (Å)		
Bulk	2.446 ± 0.003	3.989 ± 0.005	4.696 ± 0.007
Etched-H	2.445 ± 0.010		
Etched-O	1.748 ± 0.029	2.472 ± 0.022	
Sol-Gel	1.729 ± 0.010	2.478 ± 0.035	
Ca1	1.763 ± 0.005	2.467 ± 0.006	
Cs1	2.437 ± 0.011		

Table 6.1: A summary of the interatomic distances of the nanoparticles in the samples as determined by EXAFS. Peaks at $\sim$ 1.8 Å correspond to germanium oxide, while peaks at $\sim$ 2.4 Å correspond to Ge.

The interatomic distances of the magnitude of the Fourier transform for the EXAFS data are shown in table 6.1. Details of the fitting and refinement used to find the interatomic distances can be found in Appendix D. Error values were obtained from the results of the refinement procedure. One can clearly observe the difference in the position of the major peak in the Fourier transform of the XAS

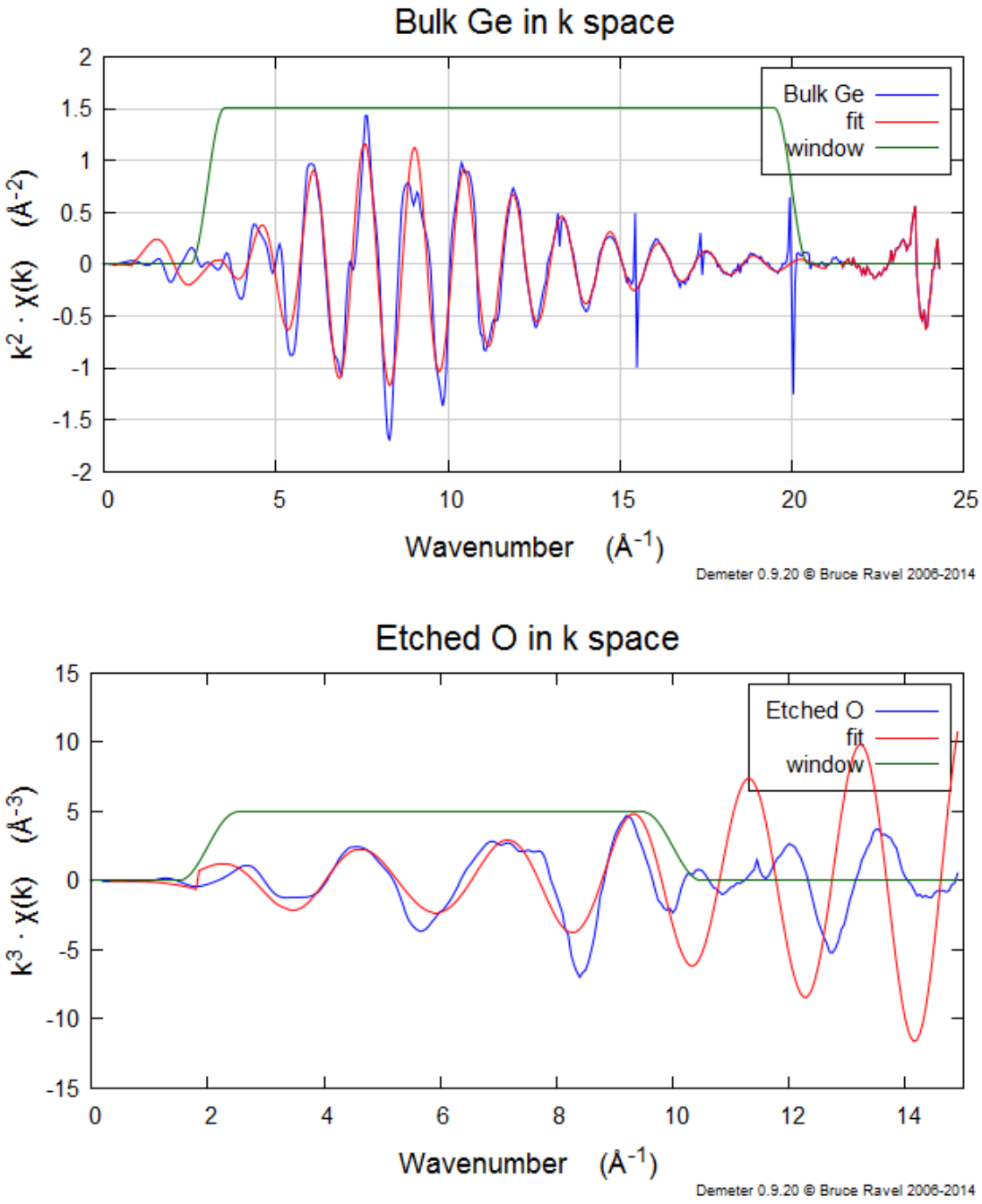

Figure 6.2: The background subtracted and fitted EXAFS spectra for Bulk Ge and the oxygen terminated etched sample.

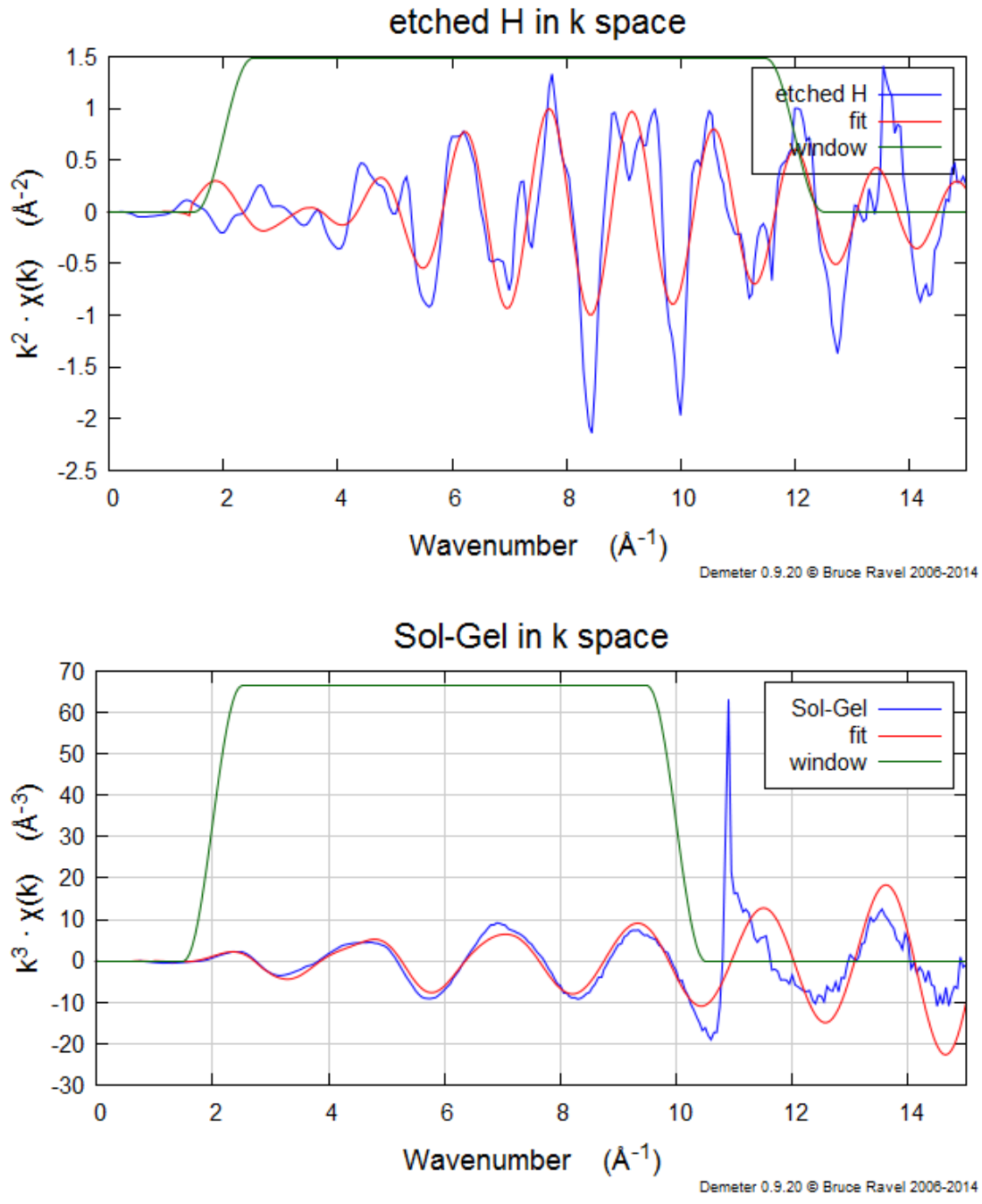

Figure 6.3: The background subtracted and fitted EXAFS spectra for the hydrogen terminated etched and Sol-gel samples.

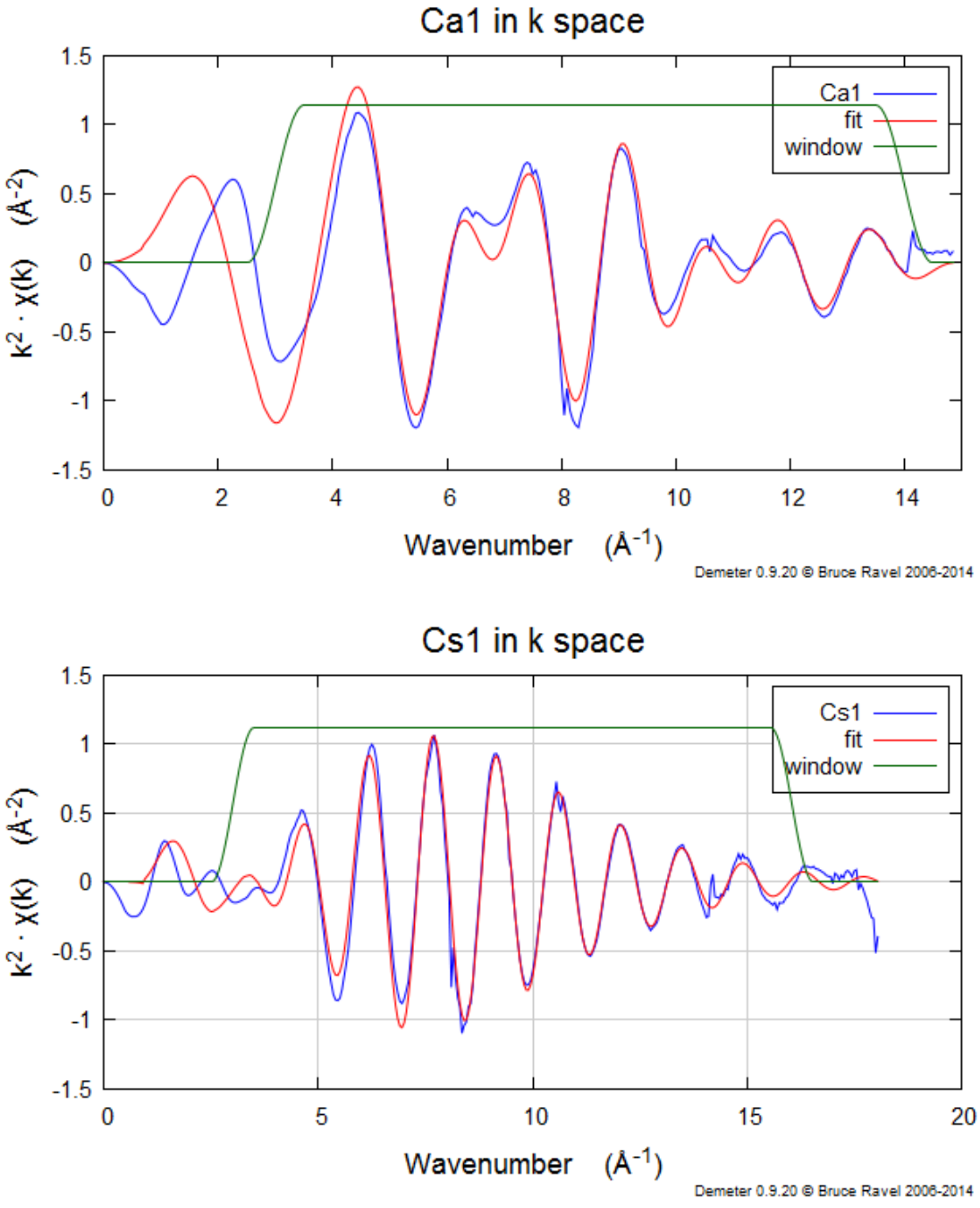

Figure 6.4: The background subtracted and fitted EXAFS spectra for Ca1 and Cs1.

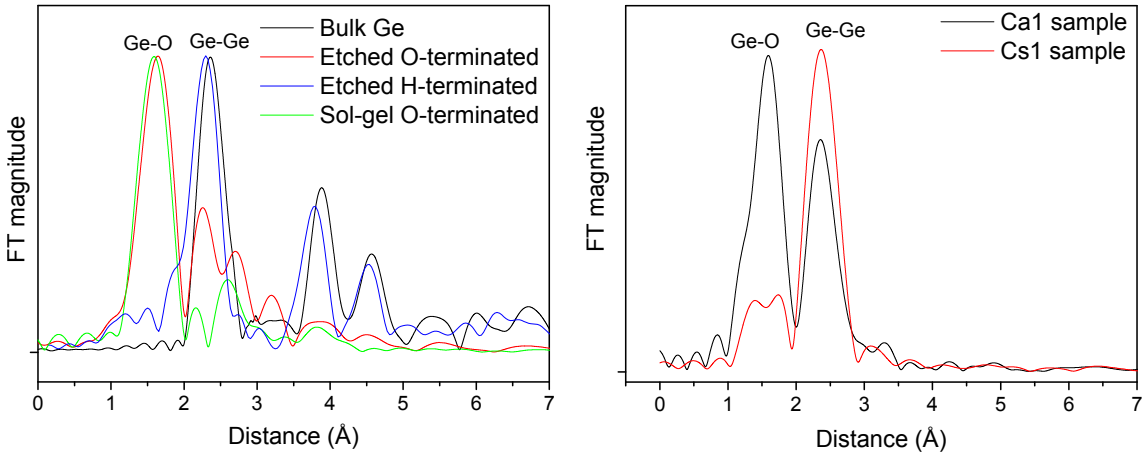

Figure 6.5: The magnitude of the Fourier transform of XAS for all samples. Bulk, etched-O and -H terminated, and sol-gel samples on the left, both colloidal samples on the right. Peaks at around $\sim$ 2.4 Å indicate Ge-Ge bonds in pure Ge, while peaks at $\sim$ 1.8 Å indicate Ge-O bonds in germanium oxide.

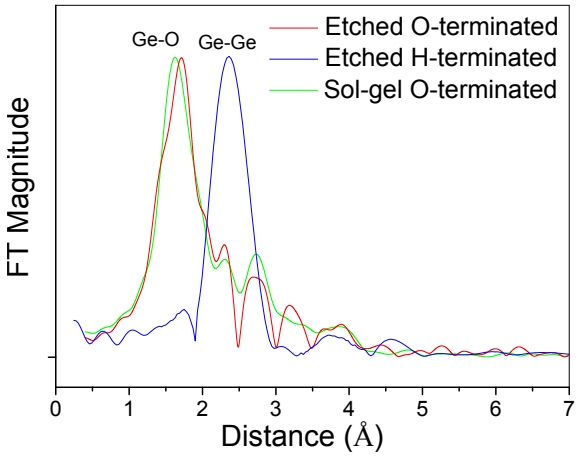

Figure 6.6: The magnitude of the Fourier transform of OD-XAS for etched and sol-gel samples. Once again, peaks at around $\sim$ 2.4 Å indicate Ge-Ge bonds in pure Ge, while peaks at $\sim$ 1.8 Å indicate Ge-O bonds in germanium oxide.

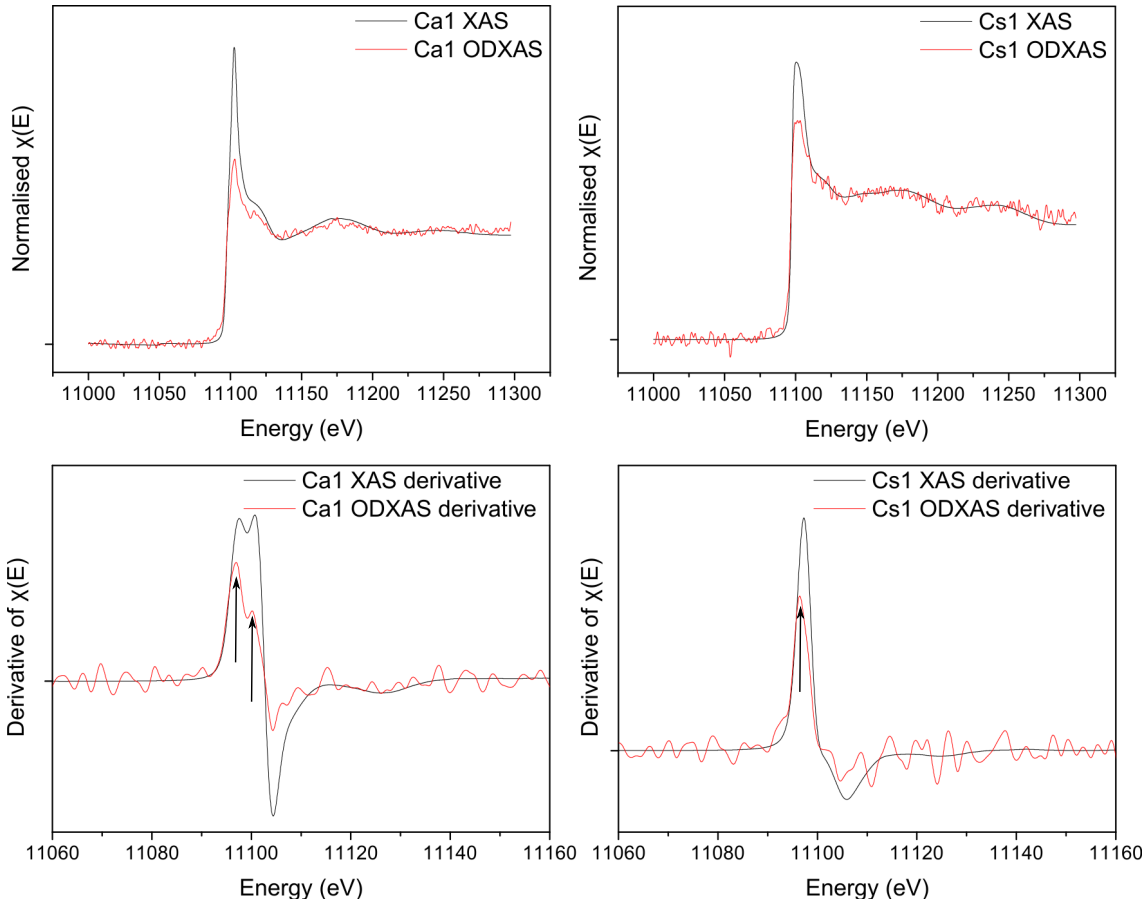

Figure 6.7: OD-XAS of the colloidal samples. The top row show the normalised spectrum, with the XAS spectrum for comparison. The bottom row shows the derivative of the OD-XAS, again with XAS for comparison. The derivative of Ca1 shows a doublet feature while the derivative of Cs1 shows a singlet feature, as indicated by the arrows.

signal between the oxygen and hydrogen terminated samples in figure 6.5. In O-terminated samples it is the oxygen-rich surface that contributes the majority of the observed light emission, and the signal from the coordination shell corresponding to Ge-Ge bonds (a coordination shell at around 2.44 Å) is significantly smaller, with the exception of Ca1. The same pattern can be seen in OD-XAS in figure 6.6.

The fact that XAS shows Ca1 and Cs1 to have such disparate oxygen content is a particularly surprising result considering their XEOL spectra (shown in figure 6.1) are very similar, essentially differing only in amplitude. However, as both spectra are normalised, amplitude comparisons are only appropriate relative to other peaks in the spectra. This is similar to the response observed in the bulk, where the oxide contribution is exaggerated by normalisation of the XEOL spectrum and not observed in the bulk XAS spectrum at all.

The XAS result strongly suggests that the colloidal sample Cs1 contains little to no oxygen as seen in the transmission data in figure 6.5. The OD-XAS for Cs1 in figure 6.7 is very similar to its transmission data. This indicates that the emission is indeed due to pure Ge. The OD-XAS of Ca1, however, differs from its equivalent transmission. Firstly, the difference in peak intensity between XAS and OD-XAS is much more pronounced in Ca1 than in Cs1, seen in figure 6.7. Secondly, for Ca1 the XAS peak is much sharper than the OD-XAS peak. To investigate this discrepancy the derivative of both spectra was taken and are shown in the bottom row of figure 6.7. The derivative of Ca1 shows a clear doublet feature at the rising edge, while Cs1 has a singlet feature. The lower energy peak in Ca1 has the same peak position as that of the singlet in Cs1, suggesting that the lower energy peak corresponds to emission from pure Ge. The higher energy peak in the doublet of Ca1 is consistent with an emission from oxidised Ge, as the energy would be expected to

shift up slightly for an oxidised sample [149]. This suggests that there is a significant contribution from both Ge and GeO_2 in the OD-XAS spectrum of Ca1, as is seen in its transmission data in figure 6.5. The conclusion then is that both samples contain oxygen, and the oxygenated Ge in Cs1 contributes only minimally to the XAS and OD-XAS spectra, which is consistent with the transmission data.

From this point on we only performed detailed OD-EXAFS analysis of the hydrogen-terminated etched sample as the data indicated that its OD-XAS is associated with a pure Ge phase rather than oxide species. This was the only sample for which OD-EXAFS with a reasonable signal to noise ratio has been collected.

The OD-XAS analysis for hydrogen terminated samples reveals a single peak at $R = 2.44 \pm 0.01$ Å from the central atom, shown in figure 6.6. This is consistent with the corresponding value for the diamond-type structure of crystalline Ge. However, the multi-shell structure, that results from the central atoms nearest neighbours, common to crystalline Ge at these temperatures, such as in the bulk example in figure 6.5 [150], is not observed in the magnitude of the Fourier transform. If it was we would expect to see additional, smaller, peaks at greater separation corresponding to the second, third, etc. nearest neighbours. The lack of a structural signal beyond the first shell is usually an indication of a topologically disordered (e.g. amorphous) structure. In small nanoparticles this can be due to the disorder at the interface between the surface and the core [46, 63, 151]. However, the lack of a multi-shell structure in the signal may also be due to the hydrogen-terminated surface where local coordination numbers can be low. In principle, the accurate value of the coordination number can help to differentiate between the two options.

We extracted a coordination number corresponding to the single peak in the

OD-EXAFS signal and obtained the value of 2.7 ± 1.2. A reduced coordination number in the first shell as compared to the bulk sample can be an indication that the measured structure is at the surface, but extracting coordination numbers from OD-XAS with a sufficiently small error margin can be a challenge due to the complex nature of the electron excitation-de-excitation processes [92, 94, 98, 152] that can affect the signal amplitude. Furthermore, the number of relevant structural parameters (e.g. atomic distances, numbers of neighbours, Debye-Waller factors) that can be reliably extracted from the data is limited by the well-known Nyquist theorem [153], which sets the limit of information that can be obtained from the experimental data. These parameters can be highly correlated leading to increased uncertainty. This makes it virtually impossible to ascertain whether the OD-XAS signal originates from the whole of the nanoparticle, from only the surface, or from the disordered interface based solely on the analysis of coordination numbers.

One way to overcome the problems presented by an excess of variables is to use an additional source of information to restrict as many parameters as possible, reducing correlations and their associated errors. A detailed model of a Ge nanoparticle enables the improvement of the precision of the structural data extracted from OD-XAS by placing constraints on the refined parameters.

To understand the effect of reduced dimensionality on the OD-EXAFS signal and to provide a source of information to restrict the structural parameters (e.g. distances and numbers of neighbours), collaborators Dr. Dima Bolmatov and Dr. Kostya Trachenko performed molecular dynamics (MD) simulations, first of bulk Ge, to test the simulation settings, and then of Ge nanoparticles. The DL POLY MD package [154] was used, and the highly successful and widely used environment-dependent Tersoff potential [155] was employed, which is particularly well suited for

surface simulations where the atomic environment is different from that of the bulk. The system size was approximately 50 Å involving about 6,000 atoms. The bulk configuration, with periodic boundary conditions, was equilibrated for 50 ps at 100 K. The simulation used a timestep of 0.001 ps. Constant pressure was simulated to let the cell relax so that surface relaxations would be visible. To simulate a finite-size Ge nanoparticle with a free surface the cell size was increased by 20 Å, a distance larger than the Tersoff potential cutoff. This resulted in atoms in the outermost layers being exposed to vacuum, and induced a surface relaxation, as in figure 6.8a. To quantify the effect of surface relaxation the radial distribution functions (RDF) for these free surface structures have been extracted as a function of the distance d from the surface towards the centre of the particle. Figure 6.8b shows the RDFs for different values of d, and demonstrates a clear bi-modal distribution of distances as d increases, moving towards the centre of the nanoparticle. Interatomic distances shift from $\sim$ 2.43 Å at a depth of $\sim$ 5 Å to $\sim$ 2.45 Å at a depth of $\sim$ 16 Å and greater. This bi-modal distribution suggests that the surface layer is structurally different from the crystalline core. This in turn would suggest a distinctive difference in the electronic and optical properties of the surface layer as compared to that of the core.

It is not possible to observe the level of structural detail obtained from MD simulations in OD-XAS spectra. This is because MD gives the positions of nuclei while XAS is sensitive to the electron density distribution. As a consequence of this, the associated mean-square relative displacements obtained from OD-XAS are far too large and the details are masked by thermal vibrations. However, if the XEOL emission is associated with surface states only, a shortening of the average interatomic distance to below 2.44 Å should be observed in the data extracted from

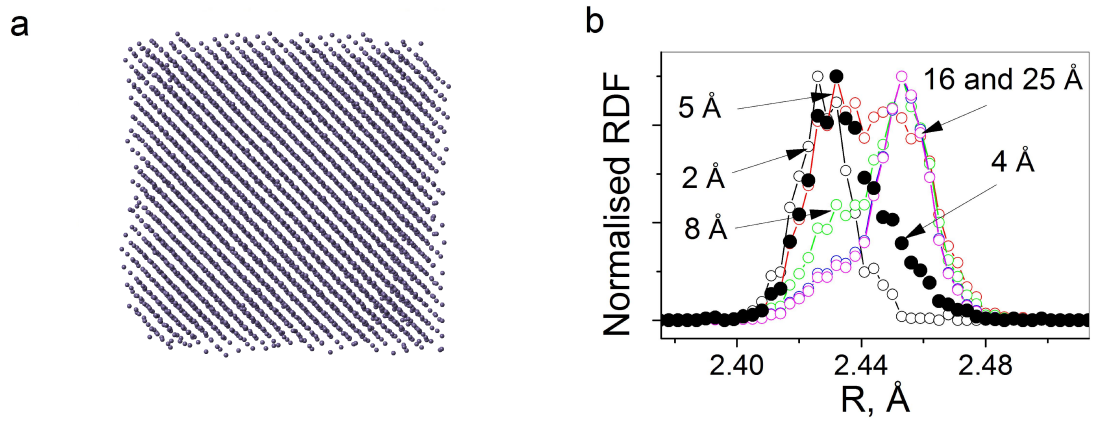

Figure 6.8: Panel (a) shows a slice of an MD simulation of a Ge nanoparticle. While the core is crystalline the surface shows the hallmarks of disorder. Panel (b) shows how the interatomic separation changes with distance from the surface of the nanoparticle. The arrows indicate the distance from the surface that the RDFs were calculated at. This forms a bimodal distribution with shorter distances at the surface and longer distances in the core, with a transitional region between.

OD-XAS as the average bond length is shorter at the surface (see figure 6.8). We observe no obvious shortening of the interatomic distance in our OD-XAS experimental data and hence conclude that the OD-XAS signal does not originate from the surface. However, cumulant analysis of the first neighbour Ge-Ge peak ($R = 2.44 \pm 0.01$ Å) in OD-XAS data indicates a non-zero value of the third cumulant (0.005 ± 0.003 Å^3, the skewness of the peak) while the third cumulant in bulk crystalline reference sample is close to zero (0.0003 ± 0.0018 Å^3). At the temperature of the experiment (T = 100 K) this peak skewness suggests that there is a static contribution to the Ge-Ge peak associated with structures with distinctly different interatomic distances. This is consistent with the bi-modal distribution of distances we observe in the RDFs obtained from the MD simulation as in figure 6.8. Information from RDFs was then used to constrain the refinement of OD-XAS data in order to investigate the origins of the peak skewness and to recover the sub-structure responsible for the observed OD-XAS signal. Specifically, the average numbers of neighbours

associated with the first peak in the RDF (corresponding to interatomic distances at the surface-core interface), the second peak (corresponding to interatomic distances in the core) and the ratio of the corresponding peaks where used as set parameters. This information was then used to generate a XAS signal and to compare the model with the experiment for a number of RDFs between $2 - 25$ Å from the surface. This allowed the number of variable parameters to be reduced to just two during a refinement: a single nearest neighbour number and a single Debye-Waller factor. The result of this comparison can be seen in figure 6.9. A clear minimum was found in the value of the fit index (which characterizes the "goodness" of a fit) for the RDF corresponding to the layer of five Å. This result suggests that the origin of the light emission can be localized to a layer extending to around five Å from the surface towards the centre of a particle within our model.

In EXAFS the goodness of a fit is determined by the fitting index, ϵ^2. The lower the value of ϵ^2 then the greater the level of agreement the calculated and experimental EXAFS data. The fitting index is given by

$$\epsilon^2 = \frac{1}{N_{ind} - p} \frac{N_{ind}}{N} \sum_{i=1}^{N} \left(\frac{\chi_i^{exp} - \chi_i^{theor}}{\sigma_i^{exp}} \right)^2, \tag{6.1}$$

where N is the total number of points, N_{ind} is the number of independent data points, p is the number of parameters being refined, χ_i^{exp} and χ_i^{theor} are the experimental data and the theoretical model respectively, and σ_i^{exp} is the standard deviation for each data point, obtained by averaging several spectra [156].

It is necessary now to examine whether such a level of localisation is achievable in OD-EXAFS, and if so, under what conditions. A detailed examination of the nature of the excitation-de-excitation processes leading to OD-EXAFS is needed.

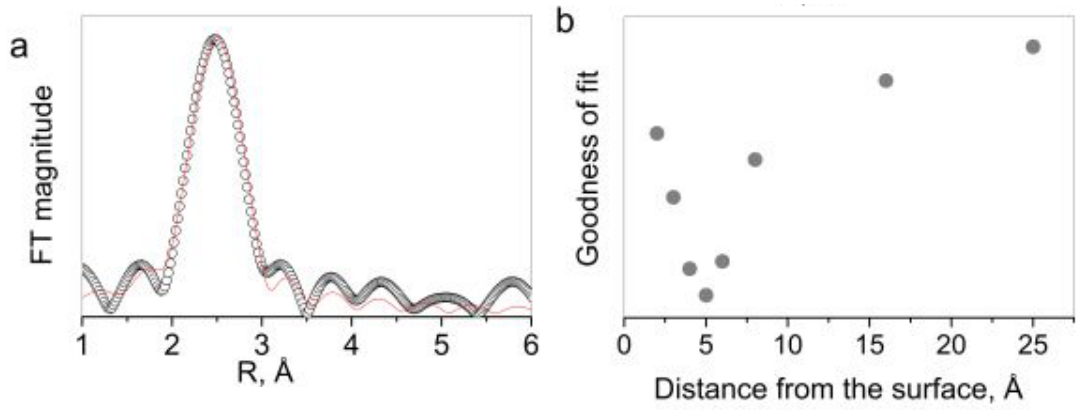

Figure 6.9: Panel (a) shows a fit of the model to data by refining two parameters, the number of nearest neighbours, and the Debye-Waller factor. Panel (b) shows that the best fit corresponds to the RDF at approximately five Å, indicating that the origin of the light emission can be localized to a layer extending to approximately five Å from the surface of the nanoparticle.

In the next section an approach from [92] and [98] is used to investigate whether it is possible in principle.

Chapter 7

The OD-XAS Model

The XEOL intensity (equation 2.14) can be expressed in terms of a sum over an arbitrary number of regions with distinct absorption coefficients. Here we consider a system composed of three regions, corresponding to the crystalline core, amorphous surface, and interfacial region between, that the studied nanoparticles are believed to consist of. Equation 2.14 can then be used to obtain the OD-XAS for a given multicomponent sample, and can be written as

$$\mathrm{d}I_{XEOL} = I_0 \sum_{i,j=1}^{3} \mu_i \eta_j \left[1 - \exp\left(-x\mu_i\right)\right] \mathrm{d}x \tag{7.1}$$

The absorption, μ, and emission, η, coefficients for each region are denoted by the subscripts i and j respectively, 1 referring to the core, 2 to the interfacial region, and 3 to the surface. In this form the model ignores the fact that the layers are sequential and that the x-ray intensity incident on the core will necessarily be lower than that incident on the surface. This is an acceptable approach to

modelling the system as the diameter of the nanoparticles it will be applied to (and probably anything that qualifies as a nanoparticle) is significantly smaller than the x-ray absorption length. In this case the attenuation length is 68.2 μ, more than a thousand times the diameter of the nanopartices. The resultant reduction in x-ray intensity incident on the core is therefore negligible and so may be ignored. It is possible that the emission (or absorption) coefficient of two regions may be the same in which case they may be assigned the same value. As described in section 2.4 and 2.5, XAS and OD-XAS experiments are concerned with measuring the EXAFS function, χ, rather than μ. The EXAFS function is defined as $\chi = (\mu - \mu_0)/(\mu_0)$, which can be rewritten as $\mu = \mu_0(1 + \chi)$ where μ_0 is the absorption coefficient minus any EXAFS affects. Making this substitution and integrating over x gives an expression for the intensity of the XEOL spectrum for the three regions in terms of their respective EXAFS functions as

$$I_{XEOL} = \sum_{i,j=1}^{3} \frac{I_0\mu_0(1+\chi_i)\eta_j}{(1+\chi_i)} \left\{1 - \exp\left[-\mu_0(1+\chi_i)d\right]\right\}. \tag{7.2}$$

As we are concerned with nanoparticles and always in the thin limit, the value of d is always small. Consequently the exponential component can be Taylor expanded up to the second term, as higher order terms are negligible. Performing both these changes results in the expression

$$I_{XEOL} = \sum_{i,j=1}^{3} \frac{I_0\mu_0(1+\chi_i)\eta_j}{\mu_0(1+\chi_i)} \left\{1 - (1 + \left[-\mu_0(1+\chi_i)d\right]\right\}. \tag{7.3}$$

The $(1 + \chi_i)$ terms are both subject to the sum and so can be cancelled. Simplifying the contents of the brackets results in

$$I_{XEOL} = \sum_{i,j=1}^{3} I_0 \mu_0 \eta_j d(1 + \chi_i), \tag{7.4}$$

When $i = j$ the process of x-ray absorption and light emission occur within the same structural region, while when $i \neq j$ the absorption and emission sites are spatially separated. Clearly, $i = j$ is preferred experimentally since it guarantees localisation, providing structural information exclusively about the region where light emission takes place. The presence of cross terms would effectively negate the effect of spectral windowing illustrated in figure 6.1 as the measured signal would contain contributions from electrons excited in different environments. This, then, would be a measure of the change in absorption characteristics of several regions, not just the region emitting. This is a consequence of the measured quantity being light yield being related to the number of excited electrons. Equation 7.4 shows that the presence of cross-terms would depend on the level of localisation of both the EXAFS signal, χ, and the light yield, η, due to electron de-excitation (thermalisation) down to the bottom of the conduction band.

Localisation of the EXAFS signal (and hence of χ) is defined by the electron mean free path (EMFP) of the x-ray excited core electrons. For bulk crystalline Ge it has been shown [157] that the EMFP is between three Å and 10 Å for electron energies in the EXAFS region. In structurally disordered systems this value can be even smaller [158] thus placing the lower limit on the accuracy of the structural localisation. This lower limit is consistent with our findings.

The light yield term, η, originates from de-excitation of high energy electrons to the bottom of the conduction band following x-ray excitation. The exact nature of the de-excitation is complex, illustrated for the case of K-shell absorption in figure

7.1. All the different processes render it effectively impossible to put a number on the value of the mean-free path associated with an emission event.

The value of the EMFP for low energy electrons produced by de-excitation to the bottom of the conduction band is often in fact relatively large (i.e. significantly more than 10 Å [157]) leading to the cross-terms in equation 7.4. Still, either (or both) η or χ in the cross-terms regularly turn out to be small (compared to the $i = j$ terms) because of the low efficiency of the corresponding emission channel or low absorption by (e.g. low mass fraction of) the specific phase in a given structural region. In such a case OD-XAS will once again provide a good level of localisation. Thus, we believe, that the level of localisation reported here may be due to a combination of relative fractions of the structural components (the core, the surface, and the interface) and of the efficiency of the associated emission channels.

Close to the bottom of the conduction band the path that an electron de-excitation takes can be influenced by the energy barriers between distinct structural regions in morphologically complex systems. For example, in a multicomponent semiconductor system one may expect excited electrons to eventually decay to the bottom of the conduction band of the structure with the lowest energy value (figure 7.2). Thus, even if the value of χ_i can be small outside a region, the $\chi_i\eta_j$ product with $i \neq j$ may not be negligible. Thus, precise localisation of the origin of light emission should only be possible if the electron de-excitation is localised to the same region from which the EXAFS signal originates, that is, when $i = j$. Furthermore, in a multi-component system with various structurally distinct regions being optically active in different wavelength ranges, spectral windowing can be used as in figure 7.2 to distinguish contributions to the signal from different regions. This was essentially the motivation for the windowing illustrated in figure 6.1.

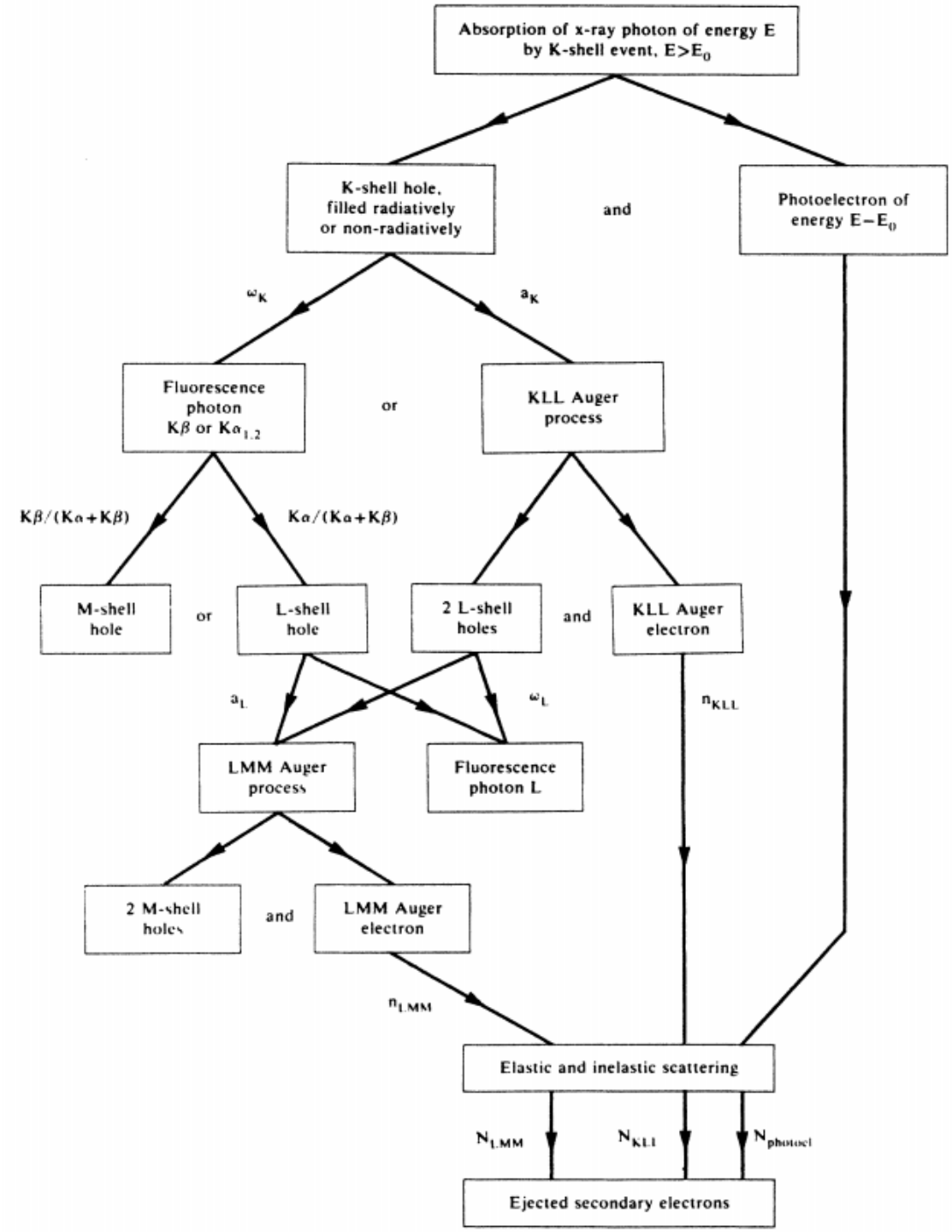

Figure 7.1: The possible de-excitation routes following x-ray absorption for K shell excitation [159].

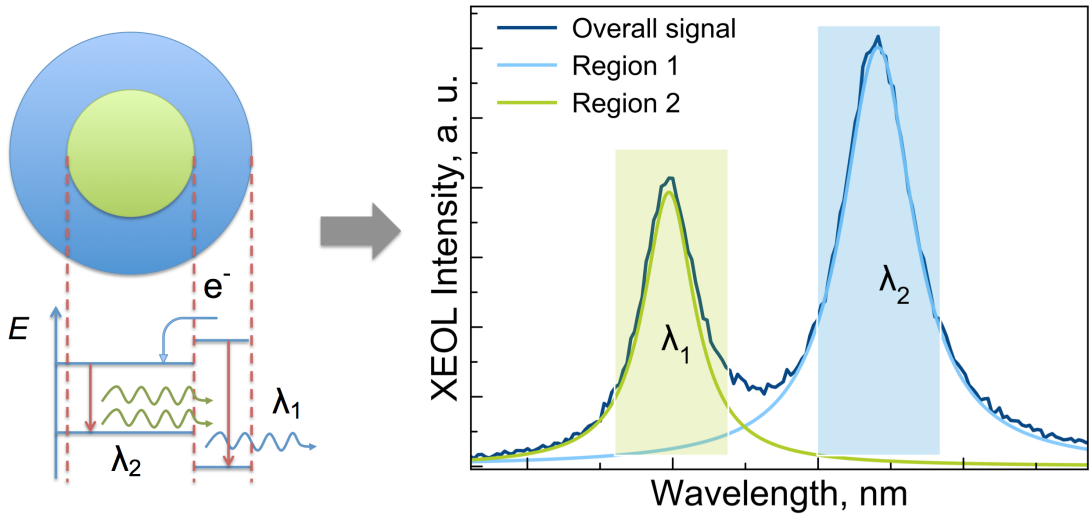

Figure 7.2: Different regions of the nanoparticle emit at different wavelengths. Here, a hypothetical nanoparticle with two distinct regions - an inner region (green), and an outer region (blue), is shown. If the regions have a different energy structure this could the location of electron de-excitation. Collecting XEOL intensity from specific peaks (i.e. windowing) may allow the structures of each to be discriminated.

The level of structural localisation of light emission reported here is based on a specific morphological model - that of a layered nanoparticle with a surface, a crystalline core and a disordered interface. However, the result has general validity beyond this model in that it is the disordered structural component at the interface between the core and the surface that contributes to the light emission. Furthermore, it is most likely that the reported level of localisation is either due to the relatively small crystalline core or the relatively high efficiency of the XEOL emission, η, of the five Å interface layer. Another important point is that MD simulations allow a detailed structural model to be obtained that can be used as a guide to constrain parameters used in EXAFS refinement thus improving the precision with which structural parameters are extracted. This model, if consistent with the experimental data, can further be used to examine the structural and optical properties of a system.

Chapter 8

Conclusion and Future Work

8.1 Conclusion

In this thesis experimental techniques sensitive to short and long range order were combined to determine the structure of matrix-free Ge nanoparticles. It has been shown that no one technique is sufficient to fully characterise a sample. Here we demonstrate that the combined use of techniques sensitive to short (EXAFS and OD-EXAFS) and long range order (Raman and XRD) can be used to great effect to characterise a sample. TEM generally found the largest measure of nanoparticle size. This is because it allows direct observation of the nanoparticles and does not require a structural model to obtain a particle size. Raman spectroscopy resulted in a smaller calculated value for the size than TEM observations. This is because Raman does have structural dependence, favouring the crystalline component that we suggest is found in the core. XRD was performed on the colloidal samples and resulted in the smallest value for the particle size. The XRD result is again due to

the structural sensitivity of the technique, which shows a stronger dependence on the crystalline structure of a sample than Raman does. PL is the least stringent technique for size analysis as light emission can be affected by not only size, but structure, morphology, and surface states as well. PL resulted in values of the average nanoparticle size greater than TEM for both colloidal samples.

The discrepancies between the sizes determined from each technique highlight the importance of combined measurements and especially those providing complementary structural information (i.e. EXAFS, XRD, Raman, TEM, etc.) Raman and XRD are too dependent on long range structural correlations, while TEM may not provide sufficient detail, giving no information on the structure. Therefore it is only through the use of all of these techniques that it was possible to suggest that the nanoparticles consist of a core-shell structure. This sets a benchmark for future studies of new nanoparticles to be characterised.

Once the above techniques were used in conjunction, the samples were determined to be either amorphous or amorphous with crystalline content. In order to distinguish between these two possibilities we used Raman spectroscopy under high pressure. This is possible because the two phases have different transition pressures, amorphous Ge transitions at $\approx$ six GPa while crystalline Ge transitions at $\approx$ 11 GPa. We observed remarkable stability of the ambient phase of Ge nanoparticles under pressures of up to at least 18 GPa. Experimental data show a strong non-linearity in the Raman peak position as the pressure is increased, which we explain by pressure induced amorphisation. We find that the Raman signal is lost above 18 GPa which correlates with decreasing optical transmission suggesting sample metallisation. Close analysis of the experimental data and of the available simulations suggests that the amorphisation is most likely driven by the surface disorder. We

demonstrated that the best model for Ge nanoparticles is a core-shell structure, with a crystalline core and disordered surface layer.

In this thesis we also show that a combination of MD simulations and OD-XAS can be used to obtain structural information about regions contributing to the light emission in Ge nanoparticles on a sub-nanoparticle scale. We show that in Ge nanoparticles the contribution to photoluminescence crucially depends on the surface termination. In samples with an oxidised surface there is a clear contribution from the oxide to the light emission. With the assistance of molecular dynamics simulations we show that in samples with a hydrogen terminated surface a disordered region located close to the surface plays a key role in the light emission.

Using XAS and OD-XAS for identifying the structural origins of light emission is not limited to Ge nanoparticles, and can in principle be applied to any nanoparticles exhibiting photoluminescence. This can prove to be of significant use to the greater community as nanoparticles are receiving ever increasing attention for their emissive properties, as described in section 1.1. Understanding the structural origins of the light emission can potentially allow for the optimisation of light emission by tuning the production techniques to maximise the structural region where the emission originates. This would enhance the efficacy of all the potential applications outlined in section 1.1 that rely on photoluminescence, rendering it a very worthwhile endeavour.

8.2 Future work

The high pressure experiments lend themselves to further investigation. Currently we do not know what happens after the phase transition. Using a direct structural technique it is possible to show how the structure is affected by pressure. To gain a thorough understanding of the process the high pressure method described herein can be combined with not only Raman, but XRD and EXAFS as well. This would be beneficial as it directly probes novel behaviour. This work is currently being undertaken, and preliminary results are consistent with our conclusion of gradual amorphisation.

OD-XAS also has scope for further development. Further work is required to fully understand the level of spacial sensitivity that is possible with this technique. Oxygen terminated Ge nanoparticles are ideal for this as they contain Ge and GeO_2 which both photoluminesce, and have emission at different wavelengths which can be distinguished. By using particles of different size and different surface thicknesses it will be possible to determine the minimum scale that is required before windowing allows them to be distinguished as independent structures. Development of the theoretical description of this is also important, particularly the localisation. This would require the localisation of η to be explicitly incorporated into the mathematics used to describe the system. There are similarities between electron migration between areas and the energy transfer utilised in Förster resonance energy transfer (FRET), in spirit if not in fine detail. In FRET absorption occurs in one molecule, energy is then transferred to another via resonance, which then emits a photon. FRET is restricted by the separation of the molecules and the details of the resonance interaction. In nanoparticles this translates to the thickness of the layers

and the electron mean free path. As such, one possible route for including the effects of the electron migration would be to use an overlap integral similar to that in FRET inserted into equation 7.1, before integration has taken place. This way, after integration, each cross term would have a multiplicative term associated with it which would modulate its contribution to the final spectrum according to how many electrons relative to the total correspond to that particular cross term. This is advantageous as it will lead to a greater understanding of the phenomenon, and allow for more systems to be investigated.

The OD-XAS is already generalised and so can be readily applied to other materials. While other analysis is required (for instance MD simulations to restrict parameters for fitting refinement), generally fairly standard techniques can be used for this. The windowing method would be particularly useful for larger nanoparticles where the mean free path is less of a potential problem. Once again, analysing more varieties of nanoparticles in this way could help determine if luminescence from the interface is common, and provide insight as to why it occurs at all.

For the Raman model an obvious useful addition to be implemented is a size distribution within the sample. Once size distributions are accounted for, the Raman model can be used to investigate other samples by changing material-specific property values from those of Ge for those of other materials. This would allow the high pressure behaviour of other materials to be similarly examined. This could then shed on light on whether a size dependent bulk modulus is common to all nanoparticles, particular types of nanoparticles, or (however improbably) Ge exclusively.

Appendix A

The Computational Model

The RWL model is most useful as a comparative tool to assist in analysing experimental data. Three main steps are required in order to determine the particle size of a sample from its Raman spectrum. Firstly, the model is used to reliably generate Raman spectra for a nanoparticle of a given size over an arbitrary frequency range. Secondly, key information must be extracted from experimental data, specifically the peak position and FWHM. Thirdly, the model is recalculated for varying sizes of nanoparticle until the key parameters from the experimental data and the calculated model agree. One parameter may be preferred over the other, typically the FWHM due to its reduced susceptibility to calibration errors and that it is easier to determine than the peak position for some experimental spectra. The size that this iterative process converges to is taken to be the average size of particles in the sample.

A.1 Calculating a Spectrum

All scripts were written using MATLAB [160].

A.1.1 Calculating Raman Intensity for an Arbitrary Wavelength

First the basic module of the fitting routine, *rampoint*, calculates the value of a single point in a Raman spectrum for a nanoparticle of a given size and material. This module can be applied to a wide range of nanoparticle sizes of Si and Ge. This can be extended to any material by inclusion of said materials phonon dispersion curve.

rampoint uses the amended RWL model [5, 112, 113]. Phonon dispersion curves are taken from [113] for Si and [6] for Ge. The calculated value is not normalised against anything and so is only meaningful when compared to other points in the spectrum, i.e. *rampoint* is used to calculate a full spectrum one point at a time. This will form the basis of the spectrum calculation module, and will be recalled when determining the FWHM.

```
function [ point ] = rampoint( mtype,w,D,p )
%rampoint: takes the input and calculates the amplitude of the the
%raman spectrum for a given wavenumber shift. Type refers to the
%material being looked at (1 for Ge, 2 for Si), w is the
%location in wavenumber shift to evaluate at, D is the nanoparticle
%size, and p is the pressure

    a = (0.564e-9)*(((4.76/74.37)*p)+1).^(-1/(3*(4.76)));
    %a=0.564e-9;
    d = D*(((4.76/74.37)*p)+1).^(-1/(3*(4.76)));
    %d=D;

%For Ge: a and d are the lattice parameter and nanoparticle
%size under pressure p, with p=0 gives ambient values
%The ambient values are present as comments so the consequences
%of their inclusion could be investigated

function g = ramg(q)
         g=(exp(-((q.*d)/(4.*pi)).^2)).*(a.*pi.*q.^2)./
            ((w-(300.1+1027*(1-(((4.76/74.36)*p+1)^(-1/(3*4.76))))-
            (104).*((q/(2.*pi/(a)))).^2)).^2+((2.5.*2.9)/2).^2);
end

%For Ge (because of the phonon dispersion curve): defines
%the function that is the essence of the model. It needed to be done this
%way in order to be able to do the integration effectively.


    as = (0.543e-9)*(((3.2/99.4)*p)+1).^(-1/(3*(3.2)));
    ds = D*(((3.2/99.4)*p)+1).^(-1/(3*(3.2)));
%For Si: a and d are the lattice parameter and the particle size
%under pressure p, with p=0 gives ambient values

    function s=rams(q)
        s = (exp(-((q.*ds)/(4.*pi)).^2)).*(as.*pi.*q.^2)./
            ((w-sqrt((1.714e5)+(1e5)*cos(q*(0.543e-9)/2)))^2+
            (2.9*3/2)^2)
    end
%For Si: function definition as above

if mtype == 1
    point = quadgk(@ramg,0,2*pi/a);
```

```
elseif mtype == 2
    point = quadgk(@rams,0,2*pi/as);

end
%An if statement  that determines which function is integrated over
%based on the input parameter "type" (1 for Ge, 2 for Si)
end
```

A.1.2 Automating Calculating a Raman Spectrum

Given that the points are not normalised in any way, they are only useful as part of a spectrum. The module *ramspecge* uses *rampoint* to calculate the value of the Raman spectrum for all integer wavelengths between a specified upper and lower bound (*wlow* and *whigh*, respectively) for a nanoparticle of a stated size. Now that the calculation of the Raman spectrum based on the RWL model has been automated it can be used as part of a script to find the particle size from data.

```
function [ fit ] = ramspecge(mtype,size, wlow, whigh, p )
%ramspecge: does the same thing as rampoint, but iterates across w
%to create a matirx of points for a model Raman spectrum for a
%particle of given material type and size between the limits of
%wavenumber wlow and whigh at pressure p


fit=zeros(whigh-wlow+1,2);
%creates an empty matrix that can be filled with the points
%calculated by the functions below, either g for Ge, or
%s for Si

fit(:,1)=wlow:whigh;
%sets the x coordinates for the fit with a lower limit of wlow
%and an upper limit of whigh and an increment of 1

w=wlow;
%define w as being wlow in preparation for the iteration from wlow
%to whigh in order to generate a spectrum. Defined here to avoid
%problems with "undefined variable" when defining ramg and rams
%below

a = (0.564e-9).*(((4.76./74.37).*p)+1).^(-1/(3.*(4.76)));
%a=0.564e-9;
d = size.*(((4.76./74.37).*p)+1).^(-1./(3.*(4.76)));
%d=size;

%for Ge: a and d are the lattice parameter and particle size
```

```
%respectively for the particle under pressure p
%The ambient pressure values are present as comments so that the
%consequences of their inclusion could be evaluated


function g = ramg(q)
         g = (exp(-((q.*d)/(4.*pi)).^2)).*(a.*pi.*q.^2)./
             ((w-(300.1+1027*(1-(((4.76/74.36)*p+1)^(-1/(3*4.76))))-
             (104).*((q/(2.*pi/(a))))).^2)).^2+((2.5.*2.9)/2).^2);
end

%for Ge: defining the function that is essentially the
%model. ramg calculates the y coordinate for a given x coordinate
%according to a set of conditions determined from the chosen
%input arguments

as = (0.543e-9)*(((4.76/74.37)*p)+1).^(-1/(3*(4.76)));
ds = size*(((4.76/74.37)*p)+1).^(-1/(3*(4.76)));
%for Si: definitions of lattice parameter (a) and size (d)
%under pressure, p, as above

    function s = rams(q)
        s = (exp(-((q.*ds)/(4.*pi)).^2)).*(as.*pi.*q.^2)./
            ((w-sqrt((1.714e5)+(1e5)*cos(q*(0.543e-9)/2)))^2+
            (2.9*3/2)^2)
    end
%for Si: defining the function that is the model, as above

if mtype == 1

    for n               = drange(wlow:whigh)
        fit(w-wlow+1,2) = quadgk(@ramg,0,2*pi/a);
        w               = w+1;
    end

elseif mtype == 2

    for  n              = drange(wlow:whigh)
        fit(w-wlow+1,2) = quadgk(@rams,0,2*pi/as);
        w               = w+1;
    end

end

%an if function to determine which function is used based on the
%input parameter "mtype" (1 for Ge, 2 for Si).The script
%then iterates round from wlow to whigh and populates the matrix
%"fit" appropriately to get a spectrum based on the model, obeying
%the input parameters.

end
```

A.1.3 Finding the Peak Position

The peak position is a key diagnostic tool for measuring the size of the particles as the shift relative to the bulk position varies with size in a predictable way. In this case however it will be used as a stepping stone in the process of finding the FWHM of the peak. Here a simple stepping function is used to check the Raman intensity at one end of the specified range of the spectrum and steps up point by point checking that the intensity increases. Once that condition is no longer met, the peak is found. As this is for the calculated spectra, which is noiseless, this is a perfectly suitable method.

```
function [ characteristics ] = findpeak( mtype, D,wlow,p )
%findpeak: finds the highest point of a spectrum calculated using
%the model for a certain particle type, size, and pressure. Returns
%a matrix containing the peak position (1,1) and peakheight (1,2)

pos  =  wlow;
double(pos);
iter = 1;
one  = 1;
two  = 2;
%defining the parameters. pos is the position to evaluate the height
%at, then set it to a double so can use decimal places rather than
%just integers. "iter" is the amount pos is increased by, set to 1 to
%begin with, gets progressively smaller. "one" and "two" are defined
%here so that the while can begin and not return an "undefined
%variables" error

while iter > 0.001

    while one < two
        one = rampoint(mtype, pos, D, p);
        two = rampoint(mtype, pos+iter, D, p);
        pos = pos+iter;
    end
    pos  = pos-2*iter;
    iter = iter/10;
    one  = 1;
    two  = 2;

end
%Nested while loop: innermost calculates the height at positions
%"pos" and "pos+iter" and compares them. While the height at pos
%is less than the height at pos+iter, then pos is increased by iter
%and the process continues. When the height at pos+iter is less
%than the height at pos the peak has been passed. pos is stepped
%back and the size of iter is reduced so the peak position can be
%found with greater accuracy. This is repeated until the peak
```

```
%position is found to 2 decimal places

ppos = pos-0.0005;
pheight=rampoint(mtype,ppos,D,p);
%finds the peak height, using the position determined to be the
%peak by the above loop

characteristics = [ppos, pheight];
end
```

A.1.4 Finding the FWHM

The FWHM is also necessary for comparison to the experimental data. The following module, *fwhmsim*, finds the FWHM for a spectrum calculated using *ramspecge*, above. For a calculated spectrum this is straightforward as it is noiseless. Once the peak position is identified it is simple to find the value, halve it, and find the x coordinates where the y coordinate has this value. The FWHM is then the separation of these two points.

```
function [ width ] = fwhmsim( mtype, D, wlow, whigh, p )
%fwhmsim: finds the full width half maximum for the spectrum
%calculated with the model for conditions based on the input
%parameters. mtype determines size (1 for Ge, 2 for
%Si), D is the particle size, wlow and whigh are the lower
%and upper limits for the calculated spectrum

simshape = findpeak(mtype, D, wlow, p);
%calls findpeak and evaluates it using the conditions from the
%input parameters. Returns the peak position and peak height for
%the calculated spectrum

peakpos = simshape(1,1);
%sets peakpos to the position of the peak

pos = peakpos;
%sets "pos" to the peak position found with findpeak so there is a
%starting point.

double(pos);
%sets it to a double so can use decimal places, which will be
%necessary for fine tuning

peakheight = rampoint(mtype, peakpos, D, p);
halfmax = peakheight/2;
%get parameter for the half maximum so the iterator has a stop
%condition
```

```
iter = 1;
%setting iter as 1 to begin with. This will be reduced as the program
%runs to increase accuracy

while iter > 0.00001
    height = peakheight;

    while height > halfmax
        height = rampoint(mtype, pos, D, p);
        pos = pos+iter;
    end

    pos  = pos-2*iter;
    iter = iter/10;
end
pos = pos+iter/2;
%nested while loops. innermost loop steps to larger values of w
%until the height is less than half the peak height. After that
%the outer loop steps w back to being the other side of the half
%max point and reduces iter by a factor of 10 so greater
%accuracy can be achieved. Cycled to 4 decimal places.

righthalfmax = pos;
%sets the found position as a new variable so that it wont be
%overwritten in the next loop.

iter = 1;
pos  = peakpos;
%resets the values of iter and pos so that the same process as
%above can be used to find the half max point on the left of
%the peak

while iter > 0.00001
    height = peakheight;

    while height > halfmax
        height = rampoint(mtype, pos, D, p);
        pos    = pos-iter;
    end

    pos  = pos+2*iter;
    iter = iter/10;
end
%nested while loops to do the same as the one above, but for the
%left hand side of the peak

pos = pos-iter/2;
%removing half of the last increase in pos to get it closer to
%the real value (there is a 75% chance that this gets it closer
%to the real value, but at 4 decimal places this is inconsequential
```

```
lefthalfmax = pos;
%setting the found position to a new variable to make what follows
%easier to understand

width = righthalfmax-lefthalfmax;
%gets a value for the width by subtracting the w value for the
%position of the half max height at the left hand side from the
%value at the right hand side.

end
```

A.2 Analysing Experimental Data

In order to facilitate comparison between the model and the experimental data, it was necessary to extract key parameters from the experimental spectrum. The FWHM and peak position were chosen as these are the most commonly accepted and widely used diagnostic characteristics.

A.2.1 Finding the Full-Width-Half-Maximum of Data

This module finds the FWHM of a normalised experimental Raman spectrum. This is achieved by interpolating a fit to the data and finding the locations where the interpolation crosses intensity = 0.5 and taking the difference.

```
function [ out ] = fwhm( spectrum ,unnec)
%Calculates the full-width-half-maximum of an experimentally
%obtained spectrum by interpolating a smoother spectrum and
%finding the fwhm of the interpolated peak. unnec is a legacy
%variable that is now redundant

x = spectrum(:,1);
y = spectrum(:,2);
%Splits the spectrum up in to two single column matrices
%consisting of the x and y coordinates.

ymax = max(y);
y    = y/max(y);
%Sets the variable ymax as the maximum value y coordinate
%and uses it to normalise the spectrum

x1 = x(1,1);
x2 = x(length(x),1);
```

```
%Creates new variables x1 and x2 which have the value of the x
%coordinates at the beginning and end of the spectrum respectively.
%They will be used as limits for the interpolated spectrum that
%will be used to find the FWHM.

if x1 < x2
    xi = [x1:0.001:x2];
else
    xi = [x2:0.001:x1];
end
%Creates a new column of x values within the same limits as the
%experimentally obtained spectrum but with many more points.
%This will be used as a base for the interpolation. The spacing of
%the points, determined by the second variable in the square
%brackets (here 0.001) can be changed to any number,
%depending on the needs of the user. The if else condition is to
%allow for the input spectrum to be either ascending or
%descending in wavenumber.

yi = interp1(x,y,xi);
%Generates an interpolated set of y coordinates based on the
%experimental spectrum with a point at every location.
%While interpolating will not improve the resolution of the data
%it can help increase the accuracy of the FWHM by reducing the
%amplitude of noise and so reducing the risk of the script
%finding an outlier and over or underestimating the FWHM

lim=find(yi>0.5);
%Finds all of the parts of the interpolated normalised spectrum
%which are greater than half the maximum, here 0.5 because of
%the previous normalisation

ind1=lim(1);
ind2=lim(length(lim));
x1=xi(ind1);
x2=xi(ind2);
%Creates variables that are assigned the values of the initial
%and final coordinates so that their x coordinates can be compared
%to find the width

width=abs(x1-x2);
%Finds the difference between the x values of the x
%coordinates of the region in the interpolated spectrum
%whose y value is grater than 0.5

out=horzcat(width,ymax);
%Concatenates the cell with the FWHM and the maximum y value
%in the unnormalised spectrum ready to be the output argument of
%the script

end
```

A.3 Comparing the Data to the Model

Using the various codes above it is now possible to do several things. Firstly, the model can be used to calculate the Raman spectrum for nanoparticles of a given size. This spectrum can then be analysed to find the peak position and the FWHM. Secondly, experimental spectra can be reliably analysed to find the FWHM and peak position that characterise it. With this information the two may be compared.

First a spectrum is calculated for a five nm particle (the starting size can be changed trivially at any time). This is a reasonable starting point for the particles we are using considering the Raman peak positions we observe, and that for particles larger than about 20 nm the shift is negligible and so the method would be largely useless, other than as a tool to rule out nanoscale. The script then finds the FWHM of the the experimental data using the FWHM module. The size parameter in the calculated spectrum is then iterated up or down until the FWHM of the calculated spectrum matches that of the experimental data.

```
function [ out ] = analysewidth( mtype,spectrum, wlow, whigh, p )
%analysewidth: takes all the other m files and uses them in
%conjunction to get an estimate for the size of the nanoparticles
%based on the experimentally obtained Raman spectrum.

size = 5;
%Set the starting size as 5nm. This is a reasonable starting point
%as generally will be interested in things from 2-10 nm.

simwidth = fwhmsim(mtype, size*1e-9, wlow, whigh, p);
%Calls fwhm to get the FWHM of the calculated spectrum for the
%chosen material type and pressure.

datashape = fwhm(spectrum, 1);
width     = datashape(1,1);
%Calls fwhm to get the FWHM and peak height of the inputted spectrum.
%assigns the value of the FWHM to variable width

iter = 1;
%Sets the initial value of iter, the amount that the size will be
%stepped by when looking for a match for the FWHM.

while iter > 0.001

    if simwidth - width < 0

        while simwidth < width

            size     = size - iter;
            simwidth = fwhmsim(mtype, size*1e-9, wlow, whigh, p);
```

```
        end

        size  = size + iter;
        check = 1;

    else

        while simwidth > width

            size     = size + iter;
            simwidth = fwhmsim(mtype,size*1e-9,wlow,whigh,p);

        end

        size  = size - iter;
        check = 2;

    end

    iter = iter / 10;

end
%if/else with nested whiles. The if loop determines if the size
%needs to be stepped up or down based on the difference between
%the fwhm of the data and that of the calculated spectrum. The
%while loops then step the size until the fwhm of the calculated
%spectrum overshoots the fwhm of the data. The last increase in
%size is then subtracted to get back on the other side of the fwhm.
%iter is then reduced by a factor of 10 and then the process is
%repeated. This process can be extended to an arbitrary number of
%significant figures determined by the condition on the first while
%loop, here to the third decimal place.
%Variable check is assigned in order to keep track of whether the
%final size increment is positive or negative.

if check == 1
    size = size - iter / 2;
else
    size = size + iter / 2;
end
%Removes half of the last size change. this step has a 75% chance
%of getting the size closer to the size that is the best match
%for the FWHM. Inside an if statement because whether iter is
%added or subtracted depends on if the size was being decreased
%or increased, as determined by check.
%This step will typically be inconsequential as it will usually be
%a change below the threshold of experimental accuracy, but
%considering that the computational cost is negligible it is worth
%including.
```

```
fiting     = ramspecge(mtype, size*1e-9, wlow, whigh, p);
%Calculates a spectra for the size determined to be the best match
%in the loop above, under the input pressure

dataheight = datashape(1,2);
%Calls the peak height of the data from the call to fwhm above for
%use in normalisation

simshape   = findpeak(mtype, size*1e-9, wlow, p);
simheight  = simshape(1,2);
%Gets the peak characteristics of the calculated spectrum deemed
%best fit for the data. Sets the height to a variable for easy use
%in normalisation.

x=spectrum(:,1);
y=spectrum(:,2)/dataheight;
%Sets up the x and y coordinates of the experimentally aquired
%spectrum for ploting the input data on the output axes. The y axis
%is divided by dataheight so that it is properly normalised.

x1=fiting(:,1);
y1=fiting(:,2)/simheight;
%Sets up the x and y coordinates of the calculated spectrum for doing
%the next part of the plotting. This is the spectrum calculated with
%the model that is deemed to be the best match to the data. It is
%divided by simheight to ensure it is properly normalised.

plot(x,y,x1,y1)
hleg1= legend('data','fit','polynomial');
%Plots the two sets to the axes and puts up the appropriate legend

size=[size,simwidth(1,1)];
out=vertcat(size,fiting);
%Sets the output for the function, made up of the input data and
%the determined size and FWHM.

end
```

A.4 The GUI for the Computational Model

In order for the model to be as convenient and easy to use as possible, a graphical user interface (GUI) has been implemented. This GUI calls the above scripts and handles them in much the same way as a user, but simplifies the input of variables, loading of data from files, and exporting the result.

A.4.1 The Code of the GUI

```
function varargout = firstgui(varargin)
%FIRSTGUI M-file for firstgui.fig
%      FIRSTGUI, by itself, creates a new FIRSTGUI or raises the existing
%      singleton*.
%
%      H = FIRSTGUI returns the handle to a new FIRSTGUI or the handle to
%      the existing singleton*.
%
%      FIRSTGUI('Property','Value',...) creates a new FIRSTGUI using the
%      given property value pairs. Unrecognized properties are passed via
%      varargin to firstgui_OpeningFcn.  This calling syntax produces a
%      warning when there is an existing singleton*.
%
%      FIRSTGUI('CALLBACK') and FIRSTGUI('CALLBACK',hObject,...) call the
%      local function named CALLBACK in FIRSTGUI.M with the given input
%      arguments.
%
%      *See GUI Options on GUIDE's Tools menu.  Choose "GUI allows only one
%      instance to run (singleton)".
%
% See also: GUIDE, GUIDATA, GUIHANDLES

% Edit the above text to modify the response to help firstgui

% Last Modified by GUIDE v2.5 11-Jun-2012 16:27:12

% Begin initialization code - DO NOT EDIT
gui_Singleton = 1;
gui_State = struct('gui_Name',       mfilename, ...
                   'gui_Singleton',  gui_Singleton, ...
                   'gui_OpeningFcn', @firstgui_OpeningFcn, ...
                   'gui_OutputFcn',  @firstgui_OutputFcn, ...
                   'gui_LayoutFcn',  [], ...
                   'gui_Callback',   []);
if nargin && ischar(varargin{1})
   gui_State.gui_Callback = str2func(varargin{1});
end

if nargout
    [varargout{1:nargout}] = gui_mainfcn(gui_State, varargin{:});
else
    gui_mainfcn(gui_State, varargin{:});
end
% End initialization code - DO NOT EDIT


% --- Executes just before firstgui is made visible.
```

```
function firstgui_OpeningFcn(hObject, eventdata, handles, varargin)
% This function has no output args, see OutputFcn.
% hObject    handle to figure
% eventdata  reserved - to be defined in a future version of MATLAB
% handles    structure with handles and user data (see GUIDATA)
% varargin   unrecognized PropertyName/PropertyValue pairs from the
%            command line (see VARARGIN)

% Choose default command line output for firstgui


set(handles.editinput,'String','Input File Name');
handles.type=1;
handles.output = hObject;
%when the function is initialised the material type is set to Ge (1)
%to match the default in the dropdown menu
%sets the edit text box for the input file name so that the field isn't
%blank

% Update handles structure
guidata(hObject, handles);

% UIWAIT makes firstgui wait for user response (see UIRESUME)
% uiwait(handles.figure1);


% --- Outputs from this function are returned to the command line.
function varargout = firstgui_OutputFcn(hObject, eventdata, handles)
% varargout  cell array for returning output args (see VARARGOUT);
% hObject    handle to figure
% eventdata  reserved - to be defined in a future version of MATLAB
% handles    structure with handles and user data (see GUIDATA)

% Get default command line output from handles structure
varargout{1} = handles.output;


% --- Executes on selection change in selecttype.
function selecttype_Callback(hObject, eventdata, handles)
% hObject    handle to selecttype (see GCBO)
% eventdata  reserved - to be defined in a future version of MATLAB
% handles    structure with handles and user data (see GUIDATA)

% Hints: contents = cellstr(get(hObject,'String')) returns selecttype
% contents as cell array
%        contents{get(hObject,'Value')} returns selected item from
%selecttype

val=get(hObject,'Value');
switch val
```

```
case 1
    handles.type=1;
    wlo=200;
    set(handles.editwlow,'String',wlo)
    whi=400;
    set(handles.editwhigh,'String',whi)
case 2
    handles.type=2;
    wlo=400;
    set(handles.editwlow,'String',wlo)
    whi=600;
    set(handles.editwhigh,'String',whi)
end
guidata(hObject, handles)
%sets the default upper and lower limit for plotting and fitting for the
%material selected with the drop down menu. Case 1 is Ge, case 2 is
%Ge. These values can be edited at any time by typing in the boxes


% --- Executes during object creation, after setting all properties.
function selecttype_CreateFcn(hObject, eventdata, handles)
% hObject    handle to selecttype (see GCBO)
% eventdata  reserved - to be defined in a future version of MATLAB
% handles    empty - handles not created until after all CreateFcns called

% Hint: popupmenu controls usually have a white background on Windows.
%       See ISPC and COMPUTER.
if ispc && isequal(get(hObject,'BackgroundColor'),
 get(0,'defaultUicontrolBackgroundColor'))
      set(hObject,'BackgroundColor','white');
end



function editwlow_Callback(hObject, eventdata, handles)
% hObject    handle to editwlow (see GCBO)
% eventdata  reserved - to be defined in a future version of MATLAB
% handles    structure with handles and user data (see GUIDATA)

% Hints: get(hObject,'String') returns contents of edit
%       wlow as text
%        str2double(get(hObject,'String')) returns contents of edit
%       wlow as a double
low=str2double(get(hObject,'String'));
set(handles.editwlow,'String',low);
guidata(hObject, handles)
%sets the lower limit for plotting/fitting according to what is typed in
%the editable text box labeled wlow
```

```
% --- Executes during object creation, after setting all properties.
function editwlow_CreateFcn(hObject, eventdata, handles)
% hObject    handle to editwlow (see GCBO)
% eventdata  reserved - to be defined in a future version of MATLAB
% handles    empty - handles not created until after all CreateFcns called

% Hint: edit controls usually have a white background on Windows.
%       See ISPC and COMPUTER.
if ispc && isequal(get(hObject,'BackgroundColor'),
get(0,'defaultUicontrolBackgroundColor'))
    set(hObject,'BackgroundColor','white');
end



function editwhigh_Callback(hObject, eventdata, handles)
% hObject    handle to editwhigh (see GCBO)
% eventdata  reserved - to be defined in a future version of MATLAB
% handles    structure with handles and user data (see GUIDATA)

% Hints: get(hObject,'String') returns contents of editwhigh as text
%        str2double(get(hObject,'String')) returns contents of edit
%   whigh as a double
high=str2double(get(hObject,'String'));
set(handles.editwhigh,'String',high);
guidata(hObject, handles)
%sets the upper limit for plotting and fitting based on the value typed in
%to the editable text box labelled wlow


% --- Executes during object creation, after setting all properties.
function editwhigh_CreateFcn(hObject, eventdata, handles)
% hObject    handle to editwhigh (see GCBO)
% eventdata  reserved - to be defined in a future version of MATLAB
% handles    empty - handles not created until after all CreateFcns called

% Hint: edit controls usually have a white background on Windows.
%       See ISPC and COMPUTER.
if ispc && isequal(get(hObject,'BackgroundColor'),
get(0,'defaultUicontrolBackgroundColor'))
    set(hObject,'BackgroundColor','white');
end



function edit7_Callback(hObject, eventdata, handles)
% hObject    handle to edit7 (see GCBO)
% eventdata  reserved - to be defined in a future version of MATLAB
% handles    structure with handles and user data (see GUIDATA)

% Hints: get(hObject,'String') returns contents of edit7 as text
```

```
%        str2double(get(hObject,'String')) returns contents of edit7
%as a double

%edit7 is the editable text box that will show the calculated ambient
%pressure particle size once it is calculated

% --- Executes during object creation, after setting all properties.
function edit7_CreateFcn(hObject, eventdata, handles)
% hObject    handle to edit7 (see GCBO)
% eventdata  reserved - to be defined in a future version of MATLAB
% handles    empty - handles not created until after all CreateFcns called

% Hint: edit controls usually have a white background on Windows.
%       See ISPC and COMPUTER.
if ispc && isequal(get(hObject,'BackgroundColor'),
get(0,'defaultUicontrolBackgroundColor'))
    set(hObject,'BackgroundColor','white');
end


% --- Executes on button press in pushbutton_import.
function pushbutton_import_Callback(hObject, eventdata, handles)
% hObject    handle to pushbutton_import (see GCBO)
% eventdata  reserved - to be defined in a future version of MATLAB
% handles    structure with handles and user data (see GUIDATA)

handles.fileName = uigetfile('*.*')

fileName=handles.fileName;
%handles.a=importdata(fileName);
comp=isstruct(importdata(fileName));
if comp==1
    stru=importdata(fileName);
    fnames=fieldnames(stru);
    handles.a=stru.(fnames{1,1});
else
    handles.a=importdata(fileName);
end
set(handles.editinput,'String',fileName);
guidata(hObject, handles)
a=handles.a;
x=a(:,1);
y=a(:,2);
axes(handles.axes1);
plot(x,y)
%opens the file import window when the import button is clicked. The
%editable text box beneth it then displays the file name. The input data is
%then split into two list matrices and plotted to the axes in the GUI
%window.
```

```
% --- Executes on button press in pushbutton_calculate.
function pushbutton_calculate_Callback(hObject, eventdata, handles)
% hObject    handle to pushbutton_calculate (see GCBO)
% eventdata  reserved - to be defined in a future version of MATLAB
% handles    structure with handles and user data (see GUIDATA)
h = waitbar(0,'Please wait...');

a=handles.a;
wlow     = get(handles.editwlow,'String');
wlow     = str2double(wlow);
whigh    = get(handles.editwhigh,'String');
whigh    = str2double(whigh);
pressure = get(handles.pressure,'String');
pressure = str2double(pressure);

type     = handles.type;
%gets all the values from the handles structrue that have been previously
%defined that are required for the calculation
waitbar(1/10);
if a(1,1)>a(2,1)
    a=flipud(a);
end
%if the matix goes from high w to low w this part flips it so the
%truncation below can be performed properly
waitbar(2/10);

locahigh=length(a);
while a(locahigh,1)>whigh+50
locahigh=locahigh-1;
end
%creates a variable that corresponds to the position in the input matrix
%that is 50 cm^-1 above the defined whigh position. This is to allow
%truncation of the data for a better polynomial fit, while avoiding edge
%effects
waitbar(1/4);
axes(handles.axes1);
localow=1;
while a(localow,1)<wlow-50
localow=localow+1;
end
handles.truncs=a(localow:locahigh,:);
%same as above but for 50 below wlow
waitbar(2/4);
out=analysewidth(type,handles.truncs,wlow,whigh,pressure);

handles.dat=out(2:length(out),:);

handles.s=out(1,1);
set(handles.edit7,'String',handles.s);
%calls the mfile analysewidth to calculate the ambient pressure size of the
%particles based on the data and stated values for the relevant variables.
```

```
%Then sets that value into the edit7 editable text box, which is labeled
%as the particle size. The plotting commands that draw the fit and the
%polynomial are inside the analysewidth mfile

close(h);
guidata(hObject, handles)



function pressure_Callback(hObject, eventdata, handles)
% hObject    handle to editpoly (see GCBO)
% eventdata  reserved - to be defined in a future version of MATLAB
% handles    structure with handles and user data (see GUIDATA)

% Hints: get(hObject,'String') returns contents of editpoly as text
%        str2double(get(hObject,'String')) returns contents of editpoly
% as a double
pressure=str2double(get(hObject,'String'));
set(handles.pressure,'String',pressure);
guidata(hObject, handles)
%sets the value of the polynomial used in the fitting for finding the width
%of the data. Can be edited by typing a new value in the box


% --- Executes during object creation, after setting all properties.
function pressure_CreateFcn(hObject, eventdata, handles)
% hObject    handle to editpoly (see GCBO)
% eventdata  reserved - to be defined in a future version of MATLAB
% handles    empty - handles not created until after all CreateFcns called

% Hint: edit controls usually have a white background on Windows.
%       See ISPC and COMPUTER.
if ispc && isequal(get(hObject,'BackgroundColor'),
get(0,'defaultUicontrolBackgroundColor'))
    set(hObject,'BackgroundColor','white');
end


% --- Executes on button press in exportbutton.
function exportbutton_Callback(hObject, eventdata, handles)
% hObject    handle to exportbutton (see GCBO)
% eventdata  reserved - to be defined in a future version of MATLAB
% handles    structure with handles and user data (see GUIDATA)
type   = handles.type;
size   = handles.s;
wlo    = get(handles.editwlow,'String');
wlo    = str2double(wlo);
whi    = get(handles.editwhigh,'String');
whi    = str2double(whi);
pressu = get(handles.pressure,'String');
```

```
pressu = str2double(pressu);
%calls all the variables used to calculate a spectrum from the model,
%including the size found from the fitting

fir=ramspecge(type,size*1e-9,wlo,whi,pressu);
fir(:,2)=fir(:,2)/max(fir(:,2));
%generates a normalised spectrum using the model based on the variables
%above

dat=handles.dat;
lengthdat=length(dat);
lengthfit=length(fir);

dif=lengthdat-lengthfit;
matcher=zeros(dif,2);
%finds the lengths of the two matrices (the data and the fit) and finds the
%difference

if dif > 0
    fir=vertcat(fir,matcher);
else
    dat=vertcat(dat,matcher);
end
%adds (0,0) to the shorter matrix untill they are the same length (only
%same size matrices can be concatenated)

fir=horzcat(dat,fir);
xlswrite(handles.fname,fir);
%concatenates the matrices and writes them to a .xls file with the name
%entered into the box next to the export button
%the truncated and normalised data is outputted as well as the fit so that
%the two can be plotted against each other in seperate plotting software
%without any manual processing of the input data being necessary


function edittitle_Callback(hObject, eventdata, handles)
% hObject    handle to edittitle (see GCBO)
% eventdata  reserved - to be defined in a future version of MATLAB
% handles    structure with handles and user data (see GUIDATA)

% Hints: get(hObject,'String') returns contents of edittitle as text
%        str2double(get(hObject,'String')) returns contents of
%edittitle as a double
handles.fname=get(hObject,'String');
set(handles.edittitle,'String',handles.fname);
guidata(hObject, handles)
%creates a variable to hold the name entered in to the output file
%name box
%so it can be assigned to the output file

% --- Executes during object creation, after setting all properties.
```

```
function edittitle_CreateFcn(hObject, eventdata, handles)
% hObject    handle to edittitle (see GCBO)
% eventdata  reserved - to be defined in a future version of MATLAB
% handles    empty - handles not created until after all CreateFcns called

% Hint: edit controls usually have a white background on Windows.
%       See ISPC and COMPUTER.
if ispc && isequal(get(hObject,'BackgroundColor'),
get(0,'defaultUicontrolBackgroundColor'))
    set(hObject,'BackgroundColor','white');
end



function editinput_Callback(hObject, eventdata, handles)
% hObject    handle to editinput (see GCBO)
% eventdata  reserved - to be defined in a future version of MATLAB
% handles    structure with handles and user data (see GUIDATA)

% Hints: get(hObject,'String') returns contents of editinput as text
%        str2double(get(hObject,'String')) returns contents of
%   editinput as a double


% --- Executes during object creation, after setting all properties.
function editinput_CreateFcn(hObject, eventdata, handles)
% hObject    handle to editinput (see GCBO)
% eventdata  reserved - to be defined in a future version of MATLAB
% handles    empty - handles not created until after all CreateFcns called

% Hint: edit controls usually have a white background on Windows.
%       See ISPC and COMPUTER.
if ispc && isequal(get(hObject,'BackgroundColor'),
get(0,'defaultUicontrolBackgroundColor'))
    set(hObject,'BackgroundColor','white');
end
```

A.4.2 The GUI Appearance and Use

An example of the GUI being used to analyse the Raman spectrum at ambient pressure of the sample produced via the sol-gel method is shown in figure A.1. Once the data has been imported and several key parameters have been provided the fit will be calculated and plotted against the experimental data, and provide an estimate of the average particle size at ambient pressure.

When the "Import" button is clicked a dialogue box opens which prompts the selection of a data file. Due to limitations at the time of scripting .xlsx files are not compatible, but .xls and .txt are. The data should be background-subtracted, but

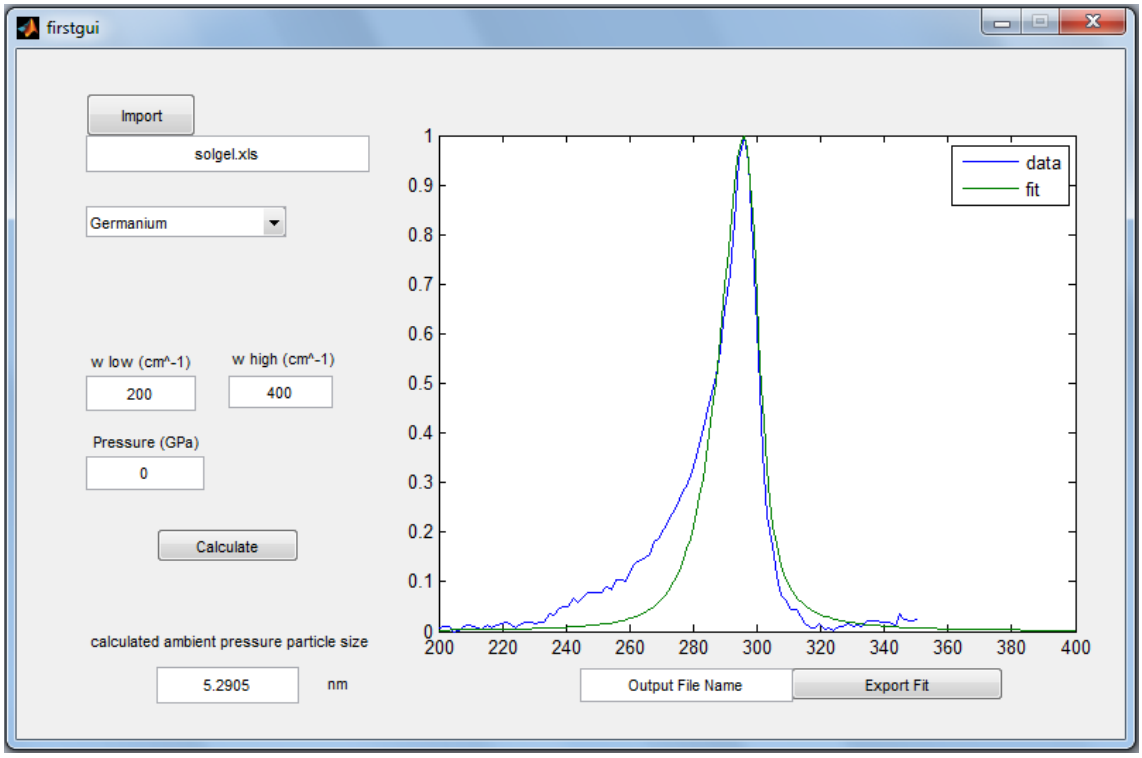

Figure A.1: The GUI being used to analyse a Raman spectrum of a sample produced by sol-gel synthesis

normalisation is not required. Once the data file has been selected and opened it is automatically plotted on the axes to the right and the file name appears in the text box below the "Import" button. The scale adjusts automatically according to the extent of the data.

Below the "Import" button and associated text box is a drop down menu where the sample material can be selected. Currently the options are limited to "Germanium" and "Silicon", where Si is not fully implemented. As mentioned previously, the scripts are sufficiently flexible that new materials can be added at any time, with minimal changes to the GUI script and the addition of key parameters for the material.

The three text boxes below are for setting the details of the fit and can be changed by the user. The "w low" and "w high" text boxes determine the limits of the fit in energy in cm^{-1}. The default settings are 200 and 400 as these are reasonable bounds for the default material, Ge. The third text box is for the pressure value in GPa. This value is to be obtained from the calibratory material present in the DAC, in our case ruby, as explained in 2.6.

Once the experimental data has been loaded and the various parameters en-

tered the fitting can be performed. The calculate button towards the bottom on the left hand side achieves this by initialising the scripts. When the calculate button is clicked a separate window reading "Please wait" is displayed for the duration of the fitting. Once the fitting is complete and the dialogue box has disappeared the calculated fit will be plotted with the experimental data on the axes to the right. The nanoparticle size which corresponds to the calculated spectrum will be displayed. The nanoparticle size is given to four decimal places but this is not intended to be representative of the degree of confidence to which the size of the nanoparticle can be determined. Four decimal places was chosen because it is likely to exceed the accuracy that would be permitted by the accuracy of any preceding experimental data. While this means it will be unlikely to be necessary for changes to be made to the scripts to achieve greater accuracy (although this is entirely possible and fairly simple), it does then require the user to determine the appropriate level of precision based on the input data. The fit is calculated to have the same FWHM of the experimentally collected data.

The calculated data from which the fit is plotted can be exported as a ".xls" file. In the bottom left text box which has the default contents "Output File Name" the desired file name should be entered. When the adjacent button labelled "Export Fit" is clicked an Excel file is created in the current MATLAB directory with the script files with the specified name. The file contains data points to reproduce the fitting plot, along with the peak position and the FWHM.

Appendix B

The Size and Lattice Parameter Pressure Dependencies

Figure B.1 shows a calculated Raman spectrum for a 2.5 nm Ge nanoparticle under a pressure of 15 GPa, calculated with neither the lattice parameter dependence nor the size dependence, each one in turn, and both together. The size of the nanoparticles used in the calculation is not important, as the same general behaviour is observed for all sizes small enough to meet the conditions for confinement. Smaller particles exhibit the change in peak shape to a greater degree, so it is useful for illustrative purposes.

When only the size change is considered to be affected by the applied pressure (i.e. the model considers the particles to be smaller from losing atoms) the linewidth is noticeably broadened towards lower wavenumbers, while the higher wavenumber side remains essentially unchanged (except for perhaps the top 10% where it leans a little so the sides meet in the right place). The peak position is also slightly shifted to lower wavenumbers. This shift is to be expected because it is predicted that for smaller particles the asymmetrical broadening increases and the peak shifts to lower wavenumbers, and with this arrangement the model considers the particles to be a set of particles with a smaller average size.

When only the lattice parameter change is considered to be affected by the applied pressure then the reverse is observed. The lineshape is asymmetrically narrowed for lower wavenumbers and the peak position is shifted slightly to higher wavenumbers. This is in line with expectations as reducing the lattice parameter in isolation results in shorter, stiffer bonds.

When both dependencies are active simultaneously the result within the model is a nanoparticle with a reduced size and the same number of atoms. The net

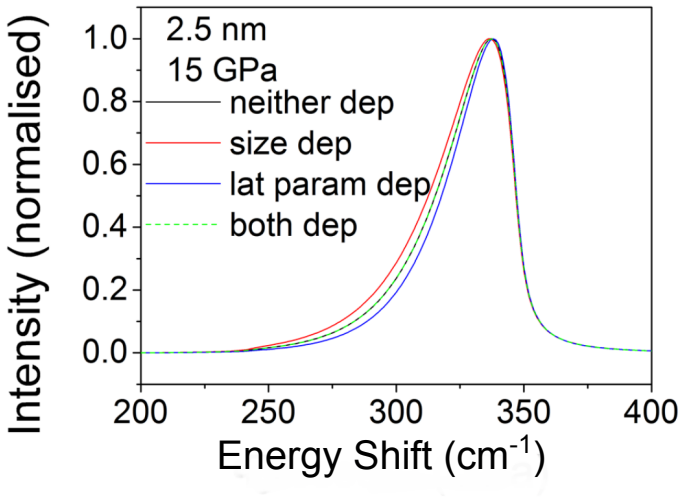

Figure B.1: The effect of the inclusion of the pressure dependence of the size, the lattice parameter, both, and neither on a Raman spectrum. The pressure dependence of the size works to broaden the lineshape, while that of the lattice parameter works to narrow it. The net effect of both is to cancel each other out. These spectra were calculated with the modified RWL model.

effect is for the Raman spectrum to be unchanged from the case where neither are considered. The data points which make up the calculated spectra for both and neither dependencies are the same to 15 decimal places, which is approaching the limit of the accuracy of the computers ability to calculate. This suggests that decreasing the lattice parameter without changing the size (i.e. putting more atoms into the nanoparticle without making it bigger) has exactly the opposite effect on the Raman spectrum as making the nanoparticle smaller by decreasing the number of atoms in it. Therefore, for the model at least, the feature of the nanoparticle that determines the lineshape of the Raman spectrum is the number of atoms that make it up. How well this represents reality will be determined by how well the model fits real world data.

Appendix C

Data Processing in EXAFS and OD-EXAFS

The software package *Athena* [161] was used to analyse XAS and OD-XAS data. *Athena* uses the *Autobk* algorithm [162] to remove the background from, and normalise the XAS spectra. The low frequency components of the Fourier transform of the spectra are optimised in order to determine the background. This can be adjusted with the R_{bkg} parameter, which determines the cutoff frequency above which the optimisation isn't performed. The spline is then refined to optimise the Fourier transform between 0 and R_{bkg}. Typically optimisation for this region means minimising it, as it was in our case.

Athena uses edge step normalisation to normalise the spectra. This is achieved by dividing the difference between $\mu(E)$ and $\mu_0(E)$ by an estimation of $\mu_0(E_0)$. Here $\mu(E)$ is the absorption coefficient of the material at x-ray energy E, $\mu_0(E)$ is the absorption coefficient of the material at energy E in the absence of EXAFS effects, and E_0 is the x-ray energy at the rising edge. The region of the spectrum that precedes the rising edge has a line regressed to it, which is then subtracted from the entire spectra. A region after the rising edge is then regressed with a polynomial which is extrapolated to E_0. The value of this polynomial at E_0 is used as the normalisation constant. Both regressions can be controlled by setting the value of the *pre-edge range* and *normalisation range* parameters. An example of this process is shown in figure C.1.

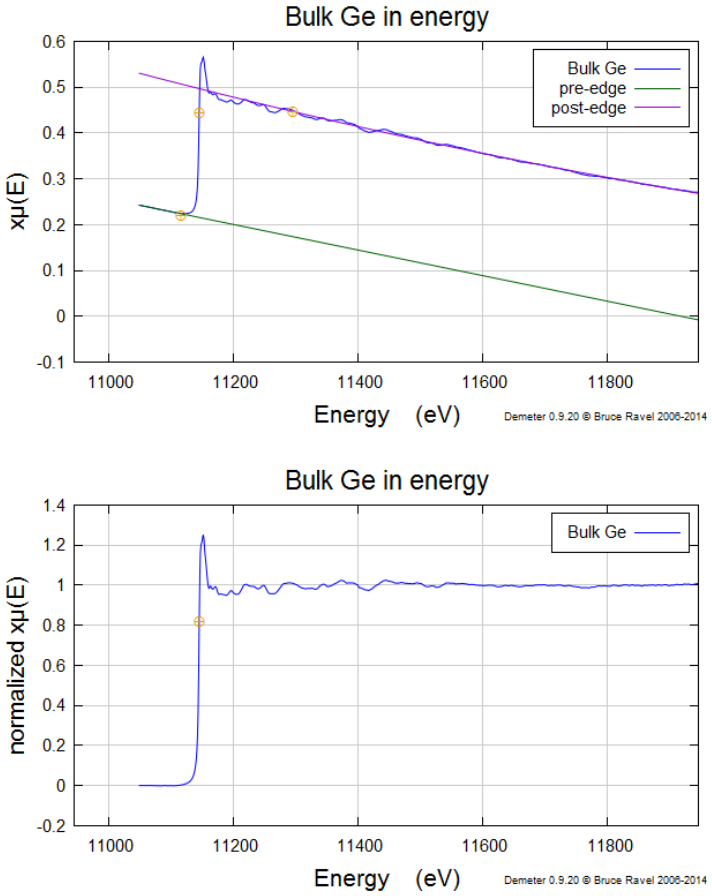

Figure C.1: The XAS spectrum for bulk Ge. Two splines are used to subtract the background and normalise the data. The initial data with splines is shown at the top of the figure, with the normalised result shown below.

Appendix D

Fitting and Refinement in *Artemis*

Once the XAS data is background-subtracted and normalised it can be compared to a model. This is performed in a piece of software called *Artemis*, which is complementary to *Athena*. An example of a fitting is shown in figure D.1 in r space and D.2 for k space. The green window indicates the region within which the fit is optimised for.

The first step involves loading a structural model and using it in conjunction with *"Atoms and Feff"* to calculate the scattering paths present in the sample so that refinement can be performed. The interface is shown in figure D.3, where the scattering paths for pure crystalline Ge have been calculated.

Once the scattering paths have been generated they can be used in the calculations for refinement. Figure D.4 shows the main interface for this process. In this case a single scattering path has been selected, a direct scattering from a first nearest neighbour. The parameters for refinement must now be considered. Here we refine the scattering amplitude attenuation, S_0^2, the energy shift, ΔE_0, the absorber-scatterer distance, ΔR, and the root mean square deviation value, σ^2, which also contributes to the Debye-Waller factor. N, the number of nearest neighbours is set to four.

Once the parameters to be refined are established they must be given initial values. Figure D.5 shows the window where initial parameters are entered. Here it is shown after refinement with the parameters as they are in the fit. Once initial parameters are entered the refinement can be run resulting in a fit as in figure D.1. The resulting parameters from the fitting refinement are listed in table D.1. The result of performing the same process for the sol-gel sample using GeO_2 as the

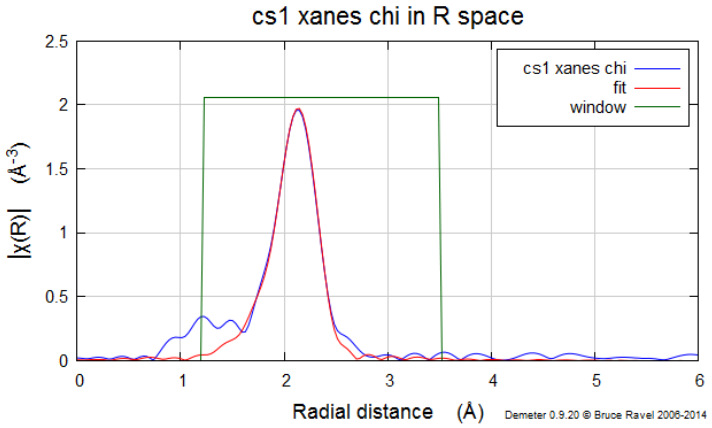

Figure D.1: The magnitude of the Fourier transform of a XAS spectrum of Cs1 fitted with *Artemis*.

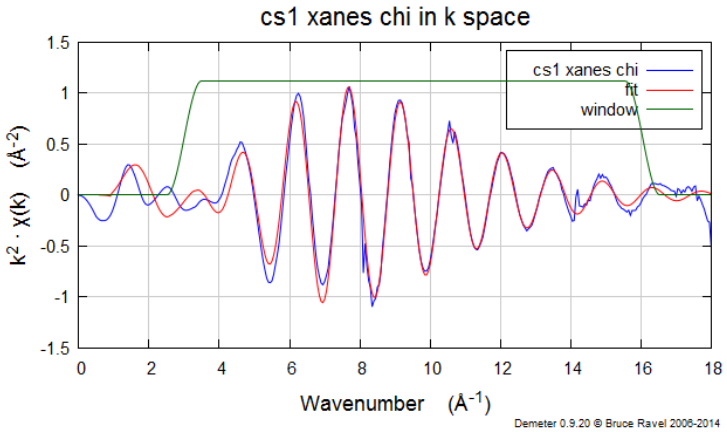

Figure D.2: The $\chi(k)$ of a XAS spectrum of Cs1 fitted with *Artemis*.

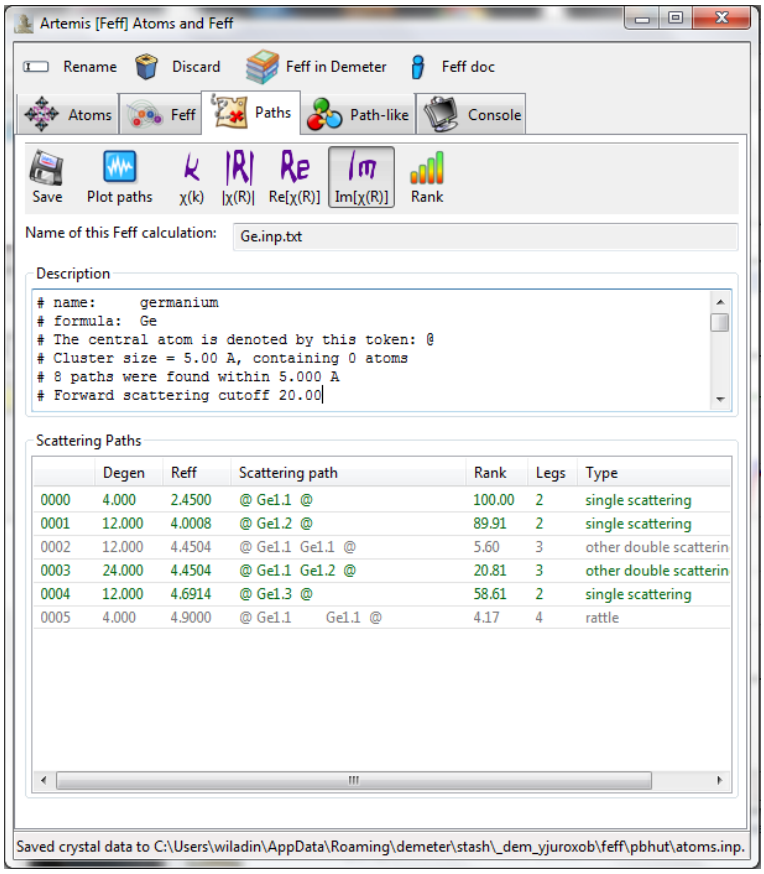

Figure D.3: *"Atoms and Feff"* is used for calculating the scattering paths.

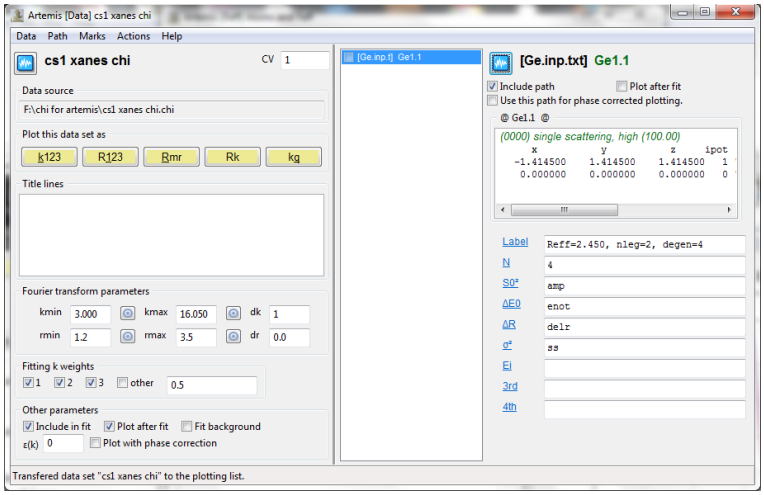

Figure D.4: The interface window where the scattering paths are defined so the parameters (scattering amplitude, etc.) can be refined.

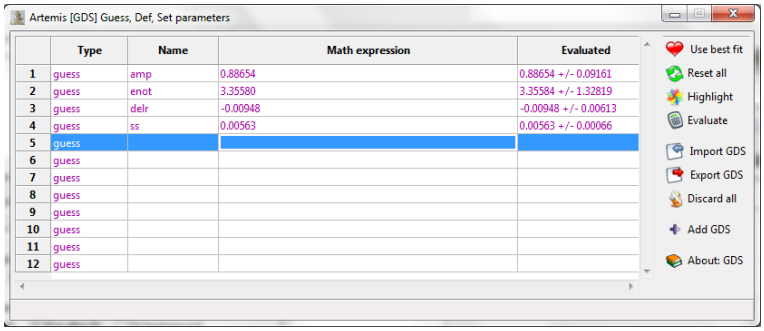

Figure D.5: Here initial values of the parameters are set, and the refined values are outputted.

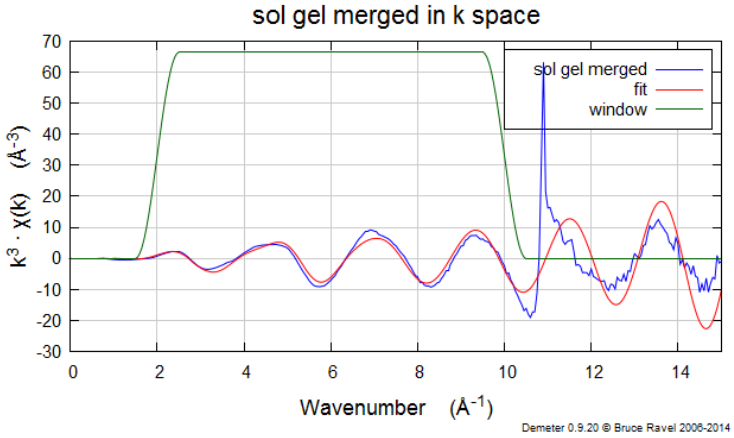

Figure D.6: The magnitude of the Fourier transform of a XAS spectrum of sol-gel fitted with *Artemis*.

structural model are shown in figures D.6 and D.7, and table D.2.

Fitting Parameters	Cs1
R-factor	0.029
N	(set) 4
S_0^2	0.886
Δ E_0	3.355 $\pm$ 1.328
σ^2	0.0056 $\pm$ 0.0061
Δ R	-0.0094 $\pm$ 0.0006

Table D.1: The fitting parameters for colloidal sample Cs1 from *Artemis*.

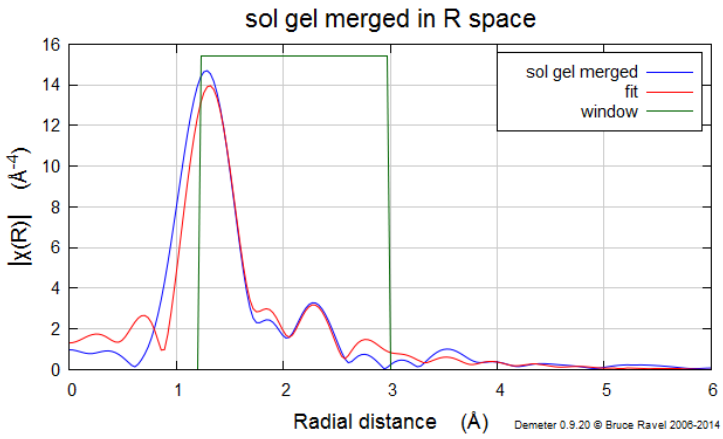

Figure D.7: The $\chi(k)$ of a XAS spectrum of Cs1 fitted with *Artemis*.

Fitting Parameters	Sol-gel
R-factor	0.018
N	(set) 2
S_0^2	(set) 0.868
Δ E_0	3.545 $\pm$ 1.468
σ^2	0.0015 $\pm$ 0.0008
Δ R	0.012 $\pm$ 0.0011
N	(set) 4
S_0^2	(set) 0.843
Δ E_0	16.005 $\pm$ 0.172
σ^2	0.0181 $\pm$ 0.0049
Δ R	0.028 $\pm$ 0.035

Table D.2: The fitting parameters for sol-gel from *Artemis*.

Fitting Parameters	XAS Refinement Bulk	Etched (O)	Etched (H)	Ca1
R-factor	0.023	0.036	0.028	0.005
N	4	2	4	2
S_0^2	0.843 ± 0.054	0.625	0.518	1.128
ΔE_0	2.095 ± 0.619	2.332 ± 0.487	2.281 ± 3.196	5.121 ± 0.880
σ^2	0.0020 ± 0.0003	0.0031 ± 0.0002	0.002 ± 0.002	0.0050 ± 0.0005
Δ R	-0.007 ± 0.002	-0.013 ± 0.009	-0.017 ± 0.013	0.025 ± 0.005
N	12	4		4
S_0^2	0.843 ± 0.054	0.633		0.413
ΔE_0	2.095 ± 0.619	2.401 ± 0.712		3.209 ± 1.387
σ^2	0.0035 ± 0.0004	0.0054 ± 0.0005		0.0032 ± 0.0006
Δ R	-0.010 ± 0.005	-0.03 ± 0.007		0.0165 ± 0.006
N	12			
S_0^2	0.843 ± 0.054			
ΔE_0	2.095 ± 0.619			
σ^2	0.0038 ± 0.0005			
Δ R	-0.016 ± 0.006			

Table D.3: The fitting parameters for bulk Ge and Ca1 from *Artemis*.

Appendix E

$\chi(k)$ Graphs for X-ray Experiments

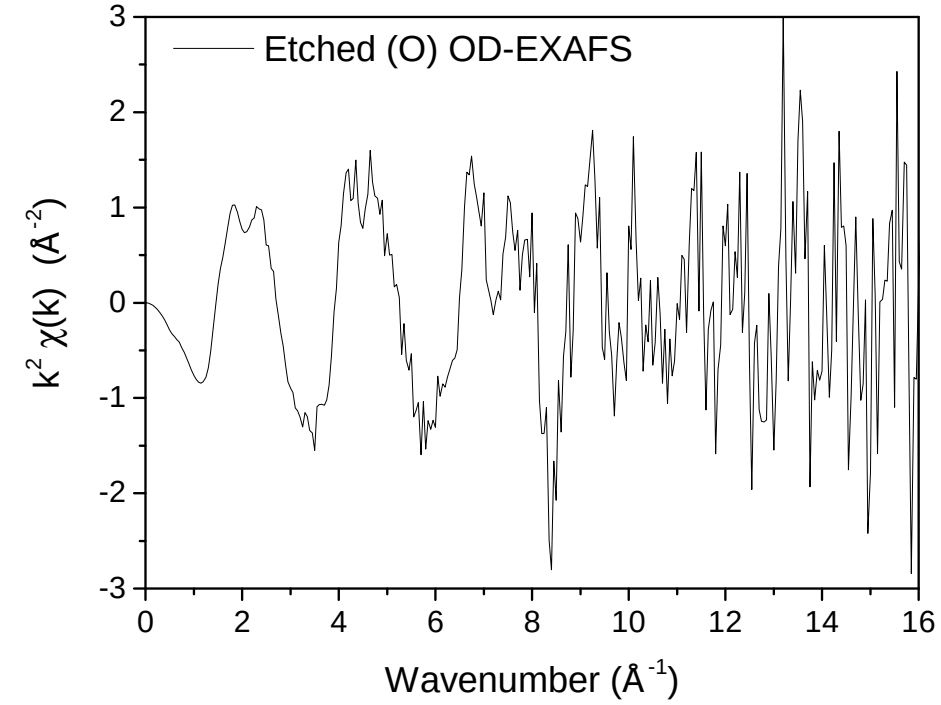
Etched (O) OD-EXAFS
k² χ(k) (Å⁻²)
Wavenumber (Å⁻¹)
3
2
1
0
-1
-2
-3
0
2
4
6
8
10
12
14
16

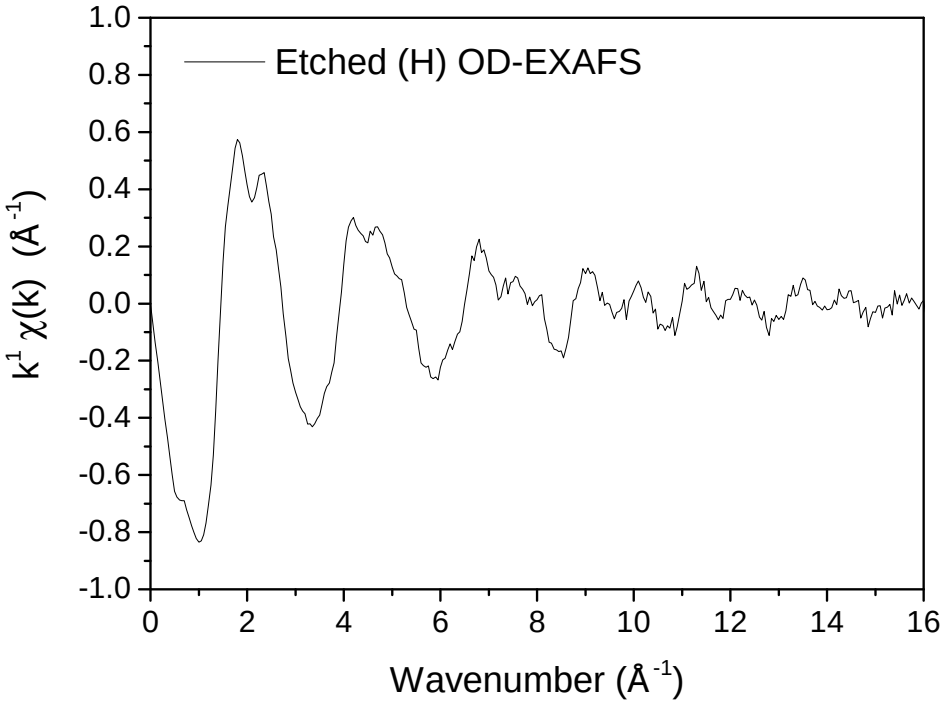
Etched (H) OD-EXAFS
k¹ χ(k) (Å⁻¹)
Wavenumber (Å⁻¹)
1.0
0.8
0.6
0.4
0.2
0.0
-0.2
-0.4
-0.6
-0.8
-1.0
0
2
4
6
8
10
12
14
16

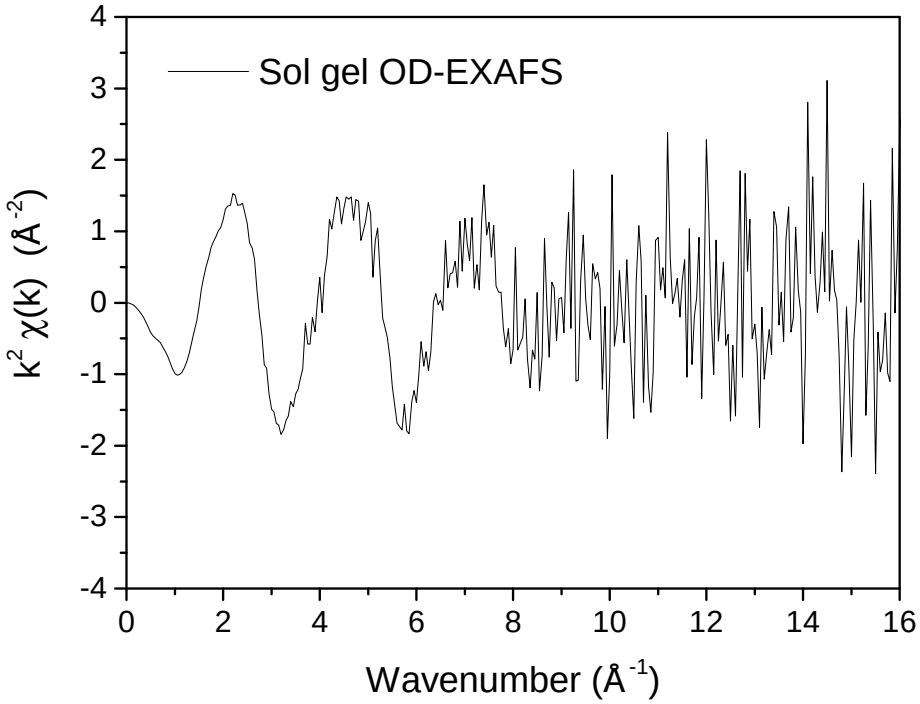
Sol gel OD-EXAFS
k² χ(k) (Å⁻²)
Wavenumber (Å⁻¹)
4
3
2
1
0
-1
-2
-3
-4
0
2
4
6
8
10
12
14
16

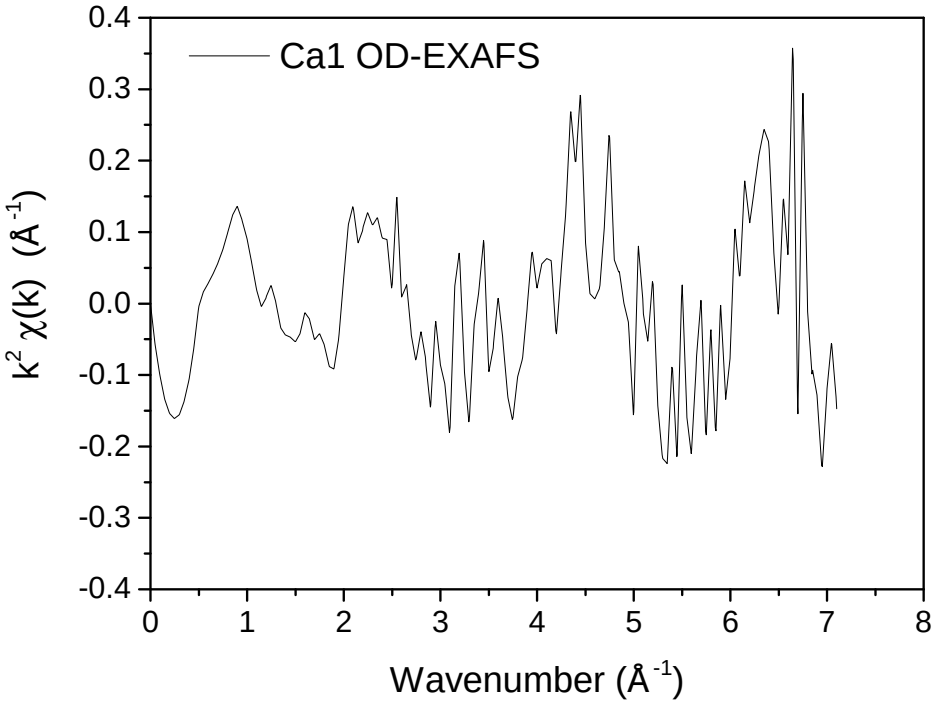
Ca1 OD-EXAFS
k² χ(k) (Å⁻¹)
Wavenumber (Å⁻¹)
0.4
0.3
0.2
0.1
0.0
-0.1
-0.2
-0.3
-0.4
0
1
2
3
4
5
6
7
8

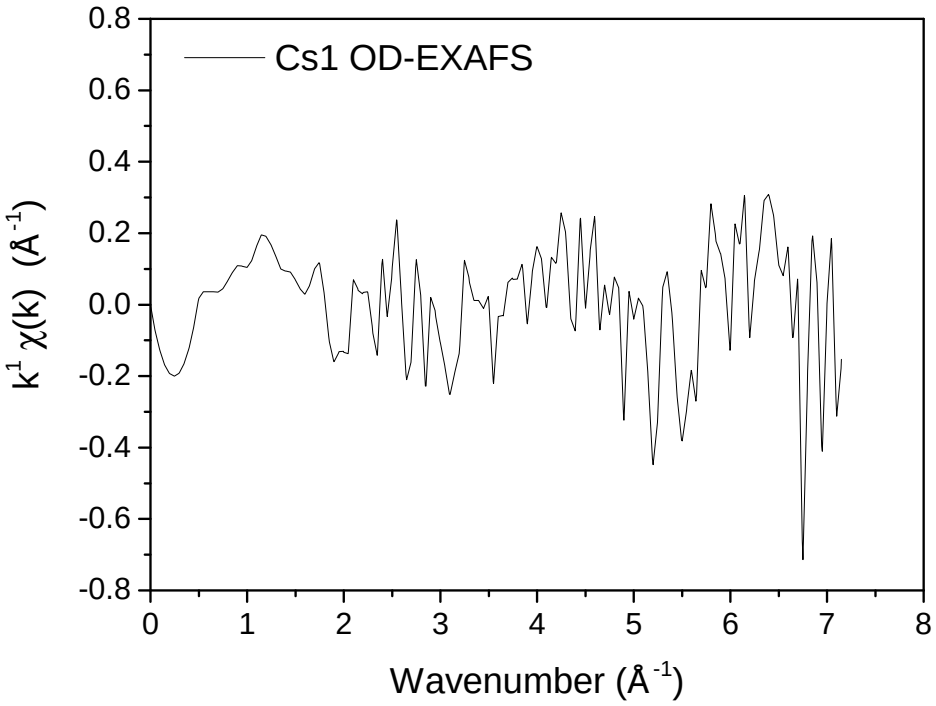
Cs1 OD-EXAFS
0.8
0.6
0.4
0.2
0.0
-0.2
-0.4
-0.6
-0.8
0
1
2
3
4
5
6
7
8
k¹ χ(k) (Å⁻¹)
Wavenumber (Å⁻¹)

Bibliography

[1] J. Perez-Arantegui, J. Molera, A. Larrea, T. Pradell, M. Vendrell-Saz, H. Borgia, B. G. Brunetti, F. Cariati, P. Fermo, M. Mellini, and Cecilia Sgamellotti, A. Viti. Luster pottery from the thirteenth century to the sixteenth century: a nanostructured thin metallic film. *Journal of the American Ceramic Society*, 84:442, 2001.

[2] I. Freestone, N. Meeks, M. Sax, and C. Higgitt. The Lycurgus cup - A Roman nanotechnology. *Gold Bulletin*, 40(4):270, 2007.

[3] C. Kittel. *Introduction to Solid State Physics*. Wiley, 2004.

[4] S. Piscanec, M. Cantoro, A. C. Ferrari, J. A. Zapien, Y. Lifshitz, S. T. Lee, S. Hofmann, and J. Robertson. Raman spectroscopy of silicon nanowires. *Physical Review B*, 68:241312, 2003.

[5] H. Richter, Z. P. Wang, and L. Ley. The one phonon Raman spectrum in microcrystalline silicon. *Solid State Communications*, 39:625, 1981.

[6] .S .K Gupta and P. K. Jha. Modified phonon confinement model for size dependent Raman shift and linewidth of silicon nanocrystals. *Solid State Communications*, 149:1989, 2009.

[7] K. W. Adu, H. R. Gutierrez, U. J. Kim, G. U. Sumanasekera, and P. C. Eklund. Confined phonons in Si nanowires. *Nano Letters*, 5:409, 2005.

[8] Marie-Lan Nguyen. Wikimedia Commons (Public Domain), 2006, accessed March 2015.

[9] P. I. Vardy. Wikimedia Commons (Public Domain), 2007, accessed March 2015.

[10] E. Stura and C. Nicolini. New nanomaterials for light weight lithium batteries. *Analytica Chimica Acta*, 568:57, 2006.

[11] E. Stathatos, P. Lianos, V. Jovanovski, and B. Orel. Dye-sensitized photoelectrochemical solar cells based on nanocomposite organic-inorganic materials. *Jornal of Photochemistry and Photobiology*, 169:57, 2005.

[12] M. Sternitzke. Structural ceramic nanocomposites. *Journal of the European Ceramic Society*, 17:1061, 1997.

[13] U. Simon and M. E. Franke. Electrical properties of nanoscaled host/guest compunds. *Microporous and Mesopourous Materials*, 41:1, 2000.

[14] J. Y. Ying, A. Tschope, and Levin D. Synergistic effects and catalytic properties tailored by nanostructure processing. *Nanostructured Materials*, 6:237, 1995.

[15] B. J. Baker, E. K. Kosmidis, D. Vucinic, C. X. Falk, L. B. Cohen, M. Djurisic, and D. Zecevic. Imaging brain activity with voltage-and calcium-sensitive dyes. *Cellular and Molecular Neurobiology*, 25(2):245, 2005.

[16] S. Antic and D Zecevic. Optical signals from neurons with internally applied voltage-sesitive dyes. *The Journal of Neuroscience*, 15(2):1392, 1995.

[17] U. Resch-Genger, M. Grabolle, S. Cavaliere-Jaricot, R. Nitschke, and T. Nann. Quantum dots versus organic dyes as fluorescent labels. *Nature Methods*, 5(9):763, 2008.

[18] A. P. Alivisatos. Semiconductor clusters, nanocrystals, and quantum dots. *Science*, 271:993, 1996.

[19] X. Peng, M. C. Schlamp, A. V. Kadavanich, and A. P. Alivisatos. Epitaxial growth of highly luminescent CdSe/Cds core/shell nanocrystals with photostability and electronic accessibility. *Journal of The American Chemical Society*, 119:7019, 1997.

[20] L. Li, J. Hu, W. Yang, and A. P. Alivisatos. Band gap variation of size- and shape-controlled colloidal CdSe quantum rods. *Nano Letters*, 1:349, 2001.

[21] J. Cox. A quantum paintbox. *Chemistry World*, page 1, 2003.

[22] T. Torchynska and Y. Vorobiev. *Advanced Biomedical Engineering*. Intech, 2011.

[23] A. K. Alivisatos, A. L. Harris, A. J. Levinos, M. L. Steigerwald, and L. E. Brus. Electronic states of semiconductor clusters: Homogeneous and inhomogeneous broadening of the optical spectrum. *The Journal of Chemical Physics*, 89:4001, 1988.

[24] V. L. Colvin, A. P. Alivisatos, and J. G. Tobin. Valence-band photoemission from a quantim-dot system. *Physical Review Letters*, 66:2786, 1991.

[25] L. E. Brus. A simple model for the ionization potential, electron affinity, and aqueous redox potentials of small semiconductor crystallites. *Journal of Chemical Physics*, 79:5566, 1983.

[26] L. T. Canham. Silicon quantum wire array fabrication by electrochemical and chemical dissolution of wafers. *Applied Physics Letters*, 57:1046–1048, 1990.

[27] A. G.Cullis, L. T. Canham, and P. D. J. Calcott. The structural and luminescence properties of porous silicon. *Journal of Applied Physics*, 82:909–965, 1997.

[28] F. Koch, V. Petrova-Koch, and T. Muschik. The luminescence of porous Si: the case for the surface state mechanism. *Journal of Luminescence*, 57:271–281, 1993.

[29] S. M. Prokes. Light emission in thermally oxidized porous silicon: Evidence for oxide-related luminescence. *Applied Physics Letters*, 62:3244–3246, 1993.

[30] M. S. Brandt, H. D. Fuchs, M. Stutzmann, J. Weber, and M. Cardona. The origin of visible luminescence from porous silicon: A new interpretation. *Solid State Communications*, 81:307–312, 1992.

[31] N. Daldosso, M. Luppi, S. Ossicini, E. Degoli, R. Magri, G. Dalba, P. Fornasini, R. Grisenti, F. Rocca, L. Pavesi, S. Boninelli, F. Priolo, C. Spinella, and F. Iacona. Role of the interface region on the optoelectronic properties of silicon nanocrystals embedded in SiO_2. *Physical Review B*, 68:085327, 2003.

[32] I. Sychugov, R. Juhasz, J. Valenta, , and J. Linnros. Narrow luminescence linewidth of a silicon quantum dot. *Physical Review Letters*, 94:087405, 2005.

[33] S. Godefroo, M. Hayne, M. Jivanescu, A. Stesmans, M. Zacharias, O. I. Lebedev, G. Van Tendeloo, and V. V. Moshchalkov. Classification and control of the origin of photoluminescence from Si nanocrystals. *Nature Nanotechnology*, 3:174–178, 2008.

[34] D. C. Hannah, J. Yang, P. Podsiadlo, M. K. Y. Chan, A. Demortière, D. J. Gosztola, V. B. Prakapenka, G. C. Schatz, U. Kortshagen, and R. D. Schaller. On the origin of photoluminescence in silicon nanocrystals: pressure-dependent structural and optical studies. *Nano Letters*, 12(8):4200, 2012.

[35] D. C. Lee, J. P. Pietryga, I. Robel, D. J. Werder, R. D. Schaller, and V. I. Klimov. Colloidal synthesis of infrared-emitting germanium nanocrystals. *Journal of the American Chemical Society*, 131:3436–3437, 2009.

[36] J. Wu, Y. Sun, R. Zou, G. Song, Z. Chen, C. Wand, and J. Hu. One-step aqueous solution synthesis of Ge nanocrystals from GeO_2 powders. *CrystEngComm*, 13:3674–3677, 2011.

[37] D. A. Ruddy, J. C. Johnson, E. R. Smith, and N. R. Neale. Size and bandgap control in the solution-phase synthesis of near-infrared-emitting germanium nanocrystals. *ACS Nano*, 4(12):7459, 2010.

[38] N. H. Chou, K. D. Oyler, N. E. Motl, and R. E. Schaak. Colloidal synthesis of germanium nanocrustals using toom-temperature bechtop chemistry. *Chemistry of Materials*, 21(18):4105, 2009.

[39] S. Hinds, S. Myrskog, L. Levina, G. Koleilat, J. Yang, S. O. Kelly, and E. H. Sargent. Nir-emitting colloidal quantum dots having 26% luminescence quantum yield in buffer solution. *Journal of the American Chemical Society*, 129:7218–7219, 2007.

[40] Y. Kanemitsu, H. Uto, Y. Masumoto, and Y. Maeda. On the origin of visible photoluminescence in nanometer-size Ge crystallites. *Applied Physics Letters*, 61:2187–2189, 1992.

[41] Y. Maeda. Visible photoluminescence from nanocrystallite Ge embedded in a glassy SiO_2 matrix: Evidence in support of the quantum-confinement. *Physical Review B*, 51(3):1658–1670, 1995.

[42] M. Zacharias and P. M. Fauchet. Blue luminescence in films containing Ge and GeO_2 nanocrystals: The role of defects. *Applied Physics Letters*, 71:380–382, 1997.

[43] G. Kartopu, V. A. Karavanskii, U. Serincan, R. Turan, Hummel R. E., Y. Ekinci, A Gunnaes, and T. G. Finstad. Can chemically etched germanium or germanium nanocrystals emit visible photoluminescence. *Physical Status Solidi*, 202:1472, 2005.

[44] K. S. Min, K. V. Shcheglov, C. M. Yang, H. A. Atwater, M. L. Brongersma, and A. Polman. The role of quantum-confined excitons vs defects in the visible luminescence of SiO_2 films containing Ge nanocrystals. *Applied Physics Letters*, 68(18):2511–2513, 1996.

[45] C. Jing, C. Zhang, X. Zang, W. Zhou, W. Bai, T. Lin, and J. Chu. Fabrication and characteristics of porous germanium films. *Science and Technology of Advanced Materials*, 10:065001, 2009.

[46] L. L. Araujo, P. Kluth, G. de M. Azevedo, and M. C. Ridgway. Vibrational properties of Ge nanocrystals determined by EXAFS. *Physical Review B*, 74:184102, 2006.

[47] D. D. Vaughn II and R. E. Schaak. Synthesis, properties and applications of colloidal germanium and germanium-based nanomaterials. *Chemical Society Reviews*, 42:2861–2879, 2013.

[48] G. Kartopu, S. C. Bayliss, V. A. Karavanskii, R. J. Curry, R. Turan, and A. V. Sapelkin. On the origin of the 2.2–2.3 eV photoluminescence from chemically etched germanium. *Journal of Luminescence*, 101:275–283, 2003.

[49] G. Kartopu, A. V. Sapelkin, V. A. Karavanskii, U. Serincan, and R. Turan. Structural and optical properties of porous nanocrystalline Ge. *Journal of Applied Physics*, 103:113518, 2008.

[50] E. Muthuswamy, A. S. Iskandar, M. M. Amador, and S. M. Kauzlarich. Facile synthesis of germanium nanoparticles with size control: microwave *versus* conventional heating. *Chemistry of Materials*, 25(8):1416, 2013.

[51] V. Paillard, P. Puech, M. A. Laguna, R. Carles, B. Kohn, and F. Huisken. Improved one-phonon confinement model for an accurate size determination of silicon nanocrystals. *Journal of Applied Physics*, 86(4), 1999.

[52] A. Bar-Lev. *Semiconductors and Electronic Devices*. Prentice-Hall International, 1984.

[53] P. Hofman. Chemical bonding in solids. Online, http://bsclarified.wordpress.com/2011/09/20/would-you-wear-a-graphite-ring/, accessed March 2015.

[54] F. A. Reboredo and A. Zunger. Surface-passivation-induced optical changes in Ge quantum dots. *Physical Review B*, 63:235314, 2001.

[55] F. A. Reboredo and A. Zunger. *L*-to-*X* crossover in the conduction-band minimum of Ge quantum dots. *Physical Review B*, 62(4):R2275, 2000.

[56] W. Weber. Computer generation of structural models of amorphous Si and Ge. *Physical Review B*, 15:4789, 1977.

[57] Band structure of germanium. http://www.globalsino.com/micro/1/1micro9970.html, accessed March 2015.

[58] J. D. Joannopoulos and M. L. Cohen. Electronic properties of complex crystalline and amorphous phases of Ge and Si. I. Density of states and band structures. *Physical Review B*, 7:2644, 1973.

[59] J. D. Joannopoulos and M. L. Cohen. Electronic properties of complex crystalline and amorphous phases of Ge and Si. II. Band structure and optical properties. *Physical Review B*, 8:2733, 1973.

[60] B. D. Malone and M. L. Cohen. Electronic structure, equation of state, and lattice dynamics of low-pressure Ge polymorphs. *Physical Review B*, 86:054101, 2012.

[61] D. Selli, I. A. Baburin, R. Martoňák, and S. Leoni. Novel metastable metallic and semiconducting germaniums. *Scientific Reports*, 3:1466, 2013.

[62] D. J. Oliver. *Nanoindentation-induced Deformation Mechanisms in Germanium*. PhD thesis, The Australian National University, 2008.

[63] L. Pizzagalli, G. Galli, J. E. Klepeis, and F. Gygi. Structure and stability of germanium nanoparticles. *Physical Review B*, 63:165324, 2001.

[64] A. Mujica and R. J. Needs. First-principles calculations of the structural properties, stability, and band structure of complex tetrahedral phases of germanium: ST12 and BC8. *Physical Review B*, 48:17010, 1993.

[65] R. Cherian, C. Gerard, P. Mahadevan, N. T. Cuong, and R. Maezono. Size dependence of the bulk modulus of semiconductor nanocrystals from first-principles calculations. *Physical Review B*, 82(23):235321, 2010.

[66] H. Wang, J. F. Liu, Y. He, Y. Wang, W. Chen, J. Z. Jiang, J. Staun Olsen, and L. Gerward. High-pressure structural behaviour of nanocrystalline Ge. *Journal of Physics: Condensed Matter*, 19(15):156217, 2007.

[67] C. Bulutay. Interband, intraband, and excited-state direct photon absorption of silicon and germanium nanocrystals embedded in a wide band-gap lattice. *Physical Review B*, 76:205321, 2007.

[68] L. Brus. Electronic wave functions in semiconductor clusters: experiment and theory. *Journal of Physical Chemistry*, 90:2555, 1986.

[69] D. Jurbergs, E. Rogojina, L. Mangolini, and U. Kortshagen. Silicon nanocrystals with ensemble quantum yields exceedding 60%. *Applied Physics Letters*, 88(23):233116, 2006.

[70] C. Bostedt. *Electronic Structure of Germanium Nanocrystal Films Probed with Synchrotron Radiation*. PhD thesis, Lawrence Livermore National Laboratory, 2002.

[71] T. van Buuren, L. N. Dinh, L. L. Chase, S. W. J., and L. J. Terminello. Changes in the electronic properties of Si nanocrystals as a function of particle size. *Physical Review Letters*, 80:3803, 1998.

[72] A. Smekal. Zur quantentheorie der dispersion. *Naturwissenschaften*, 11(43):873–875, 1923.

[73] D. J. Gardiner. *Practical Raman Spectroscopy*. Springer-Verlag, 1989.

[74] N. Begum, A. S. Bhatti, F. Jabeen, S. Rubini, and F. Martelli. *Nanowires*. Intech, 2010.

[75] B. R. Puri, L. R. Sharma, and M.S. Pathania. *Principles of Physical Chemistry*. Vishal Publishing, 2008.

[76] R. Gupta, Q. Xiong, C. K. Adu, U. J. Kim, and P. C. Eklund. Laser-induced fano resonance scattering in silicon. *Nano Letters*, 3:627, 2003.

[77] Moxfyre. Wikimedia Commons (Creative Commons), 2009, accessed March 2015.

[78] A. Paul and G. Luisier, M. Klimeck. Modified valence force field approach for phonon dispersion: from zinc-blende bulk to nanowires. *Journal of Computational Electronics*, 9:160, 2010.

[79] G. Goudec and P. H. Colomban. Raman spectroscopy of nanomaterials: How spectra relate to disorder, particle size and mechanical properties. *Prog. Cryst. Growth Charact. Mater.*, 2007.

[80] R. Alben, D. Weaire, J. E. Smith, and M. H. Brodsky. Vibrational properties of amorphous Si and Ge. *Physical Review B*, 11(6), 1975.

[81] M. Fujii, S. Hayashi, and K. Yamamoto. Growth of Ge microcrystals in SiO_2 thin film matrices: a Raman and electron microscopic study. *Journal of Applied Physics*, 30:687, 1991.

[82] R. F. Egerton, P. Li, and M. Malac. Radiation damage in the TEM and SEM. *International Wuhan Symposium on Advanced Electron Microscopy*, 35(6):399, 2004.

[83] S. Giorgio, C. R. Henry, C. Chapon, and C. Roucau. A high-resolution TEM study of the annealing of Pd particles supported on MgO. *Journal of Catalysis*, 148:534, 1994.

[84] R. L. Jacobson and G. K. Wehner. Study of ion-bombardment damage on a Ge (111) surface by low-energy electron diffraction. *Journal of Applied Physics*, 36:2674, 1965.

[85] N. W. Ashcroft and N. D. Mermin. *Solid State Physics*. Saunders College Publishing, 1976.

[86] A. L. Patterson. The scherrer formula for X-ray particle size determination. *Physical Review*, 56(10), 1939.

[87] R. A. Medjo. Characterisation of carbon nanotubes. Intech open (Creative Commons), accessed March 2015.

[88] E. Stern, D. Sayers, and F. Lytle. Extended X-ray-absorption fine-structure technique. III. Determination of physical parameters. *Physical Review B*, 11(12):4836–4846, 1975.

[89] A. L. Ankudinov, J. J. Rehr, and S. D. Conradson. Real-space multiple-scattering calculation and interpretation of X-ray-absorption near-edge structure. *Physical Review B*, 58(12):7565, 1998.

[90] M. Newville. IFEFFIT: interactive XAFS analysis and FEFF fitting. *Journal of Synchrotron Radiation*, 8(2):322, 2001.

[91] B. Ravel and M. Newville. Athena, Artemis, Hephaestus: data analysis for X-ray absorption spectroscopy using IFEFFIT. *Journal of Synchrotron Radiation*, 12(4):537, 2005.

[92] S. Emura, T. Moriga, J. Takizawa, M. Nomura, K. R. Bauchspiess, T. Murata, K. Harada, and H. Maeda. Optical-luminescence yield spectra produced by X-ray excitation. *Physical Review B*, 47(12):6918, 1993.

[93] A. Bianconi, D. Jackson, and K. Monahan. Intrinsic luminescence excitation spectrum and extended X-ray absorption fine structure above the K edge in CaF_2. *Physical Review B*, 17(4):2021, 1978.

[94] R. F. Pettifer, A. Glanfield, S. Gardelis, B. Hamilton, P. Dawson, and A. D. Smith. X-ray excited optical luminescence (XEOL) study of porous silicon. *Physica B*, 208 & 209:484–486, 1995.

[95] G. Dalba, P. Fornasini, R. Grisenti, N. Daldosso, and F. Rocca. On the sensitivity of the X-ray excited optical luminescence to the local structure of the luminescent Si sites of porous silicon. *Applied Physics Letters*, 74:1454–1456, 1999.

[96] N. Daldosso, G. Dalba, P. Fornasini, R. Grisenti, and F. Rocca. Size and surface effects in porous silicon studied by X-ray absorption spectroscopy. *Physica Status Solidi A*, 197:98–102, 2003.

[97] C. M. Hessel, E. J. Henderson, J. A. Kelly, R. G. Cavell, T. K. Sham, and J. G. C. Veinot. The origin of luminescence from silicon nanocrystals: A near edge X-ray absorption fine structure (NEXAFS) and X-ray excited optical luminescence (XEOL) study of oxide-embedded and freestanding systems. *The Journal of Physical Chemistry C*, 112:14247–14254, 2008.

[98] J. Goulon, P. Tola, M. Lemonnier, and J. Dexpert-Ghys. On a site-selective EXAFS experiment using optical emission. *Chemical Physics*, 78(3):347, 1983.

[99] O. Shimomura, S. Minomura, N. Sakai, K. Asaumi, K. Tamura, J. Fukushima, and H. Endo. Pressure-induced semiconductor-metal transitions in amorphous Si and Ge. *Philosophical Magazine*, 29(3), 1974.

[100] C. S. Menoni, J. Z. Hu, and I. L. Spain. Germanium at high pressures. *Physical Review B*, 34:362, 1986.

[101] D. J. Dunstan. Theory of the gasket in diamond anvil high pressure cells. *Review of Scientific Instruments*, 60(12), 1989.

[102] Tobias1984. *Wikimedia Commons*, 2012, accessed March 2015.

[103] J. A. Xu, H. K. Mao, and P. M. Bell. High-pressure ruby and diamond fluorescence: observations at 0.21 to 0.55 terapascal. *Science*, 232:1404, 1986.

[104] P. I. Dorogokupets and A. R. Oganov. Equations of state of Cu and Ag and revised ruby pressure scale. *Doklady Earth Sciences*, 391A(6):854, 2003.

[105] A. Karatutlu. *Structure and Light Emission in Germanium Nanoparticles*. PhD thesis, Queen Mary University of London, 2014.

[106] V. A. Karavanskii, A. A. Lomov, A. G. Sutyrin, V. A. Bushuev, N. N. Loikho, N. N Melnik, T. N. Zavaritskaya, and S. Bayliss. Raman and X-rays studies of nanocrystals in porous stain-etched germanium. *Thin Solid Films*, 437(1-2):290, 2003.

[107] D. R Turner. On the mechanism of chemically etching germanium and silicon. *Journal of The Electrochemical Society*, 107(10):810, 1960.

[108] E. J. Henderson, C. M. Hessel, and G. C. Cavell, R. G. Veinot. How processing atmosphere influences the evolution of GeO_2-embedded germanium nanocrystals obtained from the thermolysis of phenyl trichlorogermane-derived polymers. *Chemistry of Materials*, 22(8):2653, 2010.

[109] M. Nogami and Y. Abe. Sol-gel synthesis of Ge nanocrystals-doped glass and its photoluminescence. *Journal of Sol-Gel Science and Technology*, 9(2):139, 1997.

[110] D. D Vaughn, J. F. Bondi, and R. E. Schaak. Colloidal synthesis of air-stable crystalline germanium nanoparticles with tunable sizes and shapes. *Chemistry of Materials*, 22(22):6103, 2010.

[111] G. Viera, S. Huet, and Boufendi. Crystal size and temperature measurements in nanostructured silicon using Raman spectroscopy. *Journal of Applied Physics*, 90:4175, 2001.

[112] I. H. Campbell and P. M. Fauchet. The effects of microcrystal size and shape on the one phonon Raman spectra of crystalline semiconductors. *Solid State Communications*, 58:739, 1986.

[113] G. Faraci, Gibilico S., P. Russo, A. R. Pennisi, and S. La Rosa. Modified Raman confinement model for Si nanocrystals. *Physical Review B*, 73:033307, 2006.

[114] A. Diéguez, A. Romano-Rodriguez, a Vilà, and J. R. Morante. The complete Raman spectrum of nanometric SnO_2 particles. *Journal of Applied Physics*, 90:1550, 2001.

[115] B. Li, D. Yu, and S. Zhang. Raman spectral study of silicon nanowires. *Physical Review B*, 59:1645, 1999.

[116] Y. Du, M. S. Zhang, J. Hong, Y. Shen, Q. Chen, and Z. Yin. Structural and optical properties of nanophase zinc oxide. *Applied Physics A*, 76:171, 2003.

[117] W. H. Weber, Hass K. C., and McBride. Raman study of CeO_2: second-order scattering, lattice dynamics, and particle-size effects. *Physical Review B*, 48:178, 1993.

[118] R. Carles, A. Mlayah, M. B. Amjoud, A. Reynes, and R. Morancho. Structural characterization of Ge microcrystals in Ge_xC_{1-x} films. *Journal of Applied Physics*, 31:3511, 1992.

[119] F. Liu, L. Liao, G. Wang, G. Cheng, and X. Bao. Experimental observation of surface modes of quasifree clusters. *Physical Review Letters*, 76:604, 1996.

[120] E. Duval, A. Boukenter, and B. Champagnon. Vibration eigenmodes and size of microcrystallites in glass: observation by very-low-frequency Raman scattering. *Physical Review Letters*, 56:2052, 1986.

[121] M. Fujii, S. Hayashi, and K. Yamamoto. Growth of Ge microcrystals in SiO_2 thin film matrices: A Raman and electron microscopic study. *Japanese Journal of Applied Physics*, 30(4), 1991.

[122] J. E. Spanier, R. D. Robinson, F. Zhang, S. W. Chan, and I. P. Herman. Size-dependent properties of CeO_{2-y} nanoparticles as studied by Raman scattering. *Physical Review B*, 64:245407, 2001.

[123] V. I. Korepanov, H. Witek, H. Okajima, E. Ōsawa, and H. Hamaguchi. Communication: Three-dimensional model for phonon confinement in small particles: Quantitative bandshape analysis of size-dependent Raman spectra of nanodiamonds. *The Journal of Chemical Physics*, 140(4):041107, 2014.

[124] Renishaw 1000 documentation. http://www.renishaw.com/en/invia-raman-microscope–6260, accessed March 2015.

[125] Paginazero. Wikimedia Commons (Public Domain), 2003, accessed March 2015.

[126] Y. Maeda, N Tsukamoto, Y. Yazawa, Y. Kanemitsu, and Y. Masumoto. *Applied Physics Letters*, 59(24):3168, 1991.

[127] LLC Magicplot Systems. Magicplot. http://magicplot.com/, June 2013, accessed March 2015.

[128] I. Vasiliev, J. R. Chelikowsky, and R. M. Martin. Surface oxidation effects on the optical properties of silicon nanocrystals. *Physical Review B*, 65(12):121302, 2002.

[129] X. Han, S. Mao, Q. Wei, Y. Zhang, and Z Zhang. *In-Situ* TEM study of the thickness impact on the crystallization features of a near equal-atomic tini thin film prepared by planar magnetron sputtering. *Materials Transactions*, 47(3):536, 2006.

[130] A. F. Khan, M. Mehmood, M Aslam, and S. I. Shah. Nanostructured multilayer TiO_2-Ge films with quantum confinement effects for photovoltaic applications. *Journal of Colloid and Interface Science*, 343(1):271, 2010.

[131] J. H. Parker, D. W. Feldman, and M. Ashkin. Raman scattering by silicon and germanium. *Physical Review*, 155:712, 1967.

[132] L. B. Kiss, J. Söderlund, G. A. Niklasson, and C. G. Granqvist. New approach to the origin of lognormal size distributions of nanoparticles. *Nanotechnology*, 10:25, 1999.

[133] S. Elazzouzi-Hafraoui, Y. Nishiyama, J. L. Putaux, L. Heux, F. Dubreuil, and C. Rochas. The shape and size distribution of crystalline nanoparticles prepared by acid hydrolysis of native cellulose. *Biomacromolecules*, 9(1):57, 2007.

[134] L. B. Kiss, J. Söderlund, G. A. Niklasson, and C. G. Granqvist. The real origin of lognormal size distributions of nanoparticles in vapor growth processes. *Nanostructured Materials*, 12:327, 1999.

[135] J. Fouquet, M. Minsky, and S. J. Rosner. *HPL*, 93(92), 1993.

[136] S. Kim, S. J. Rhee, X. Li, J. J. Coleman, and S. G. Bishop. *Physical Review B*, 57(23):14 588, 1998.

[137] R. A. Meyers. *Encyclopedia of Analytical Chemistry*, page 9209, 2000.

[138] C. M. Sung, C. Goetze, and H. O. Mao. Pressure distribution in the diamond anvil press and the shear strength of fayalite. *Review of Scientific Instruments*, 48(11):1386, 1977.

[139] K. E. Brister, Y. K. Vohra, and A. L Ruoff. Pressure profiles at multimegabar pressures in a diamond anvil cell using X-ray diffraction. *Review of Scientific Instruments*, 59(2):318, 1988.

[140] J. W. Otto, J. K. Vassiliou, and G. Frommeyer. Nonhydrostatic compression of elastically anisotropic polycrystals. I. hydrostatic limits of 4:1 methanol-ethanol and parafin oil. *Physical Review B*, 57(6):3253, 1998.

[141] F. Birch. Finite elastic strain of cubic crystals. *Physical Review*, 71:809, 1947.

[142] D Olego and M Cardona. Pressure dependence of Raman phonons of Ge and 3C-SiC. *Physical Review B*, 25:1151, 1981.

[143] A. K. Das, S. K. Ghose, B. N. Dev, G. Kuri, and T. R. Yang. Spontaneous nanostructural island formation and layer-to-island mass transport in Ge layers on Si (111) surface. *Applied Surface Science*, 165:260, 2000.

[144] D. Olego and M. Cardona. Pressure dependence of Raman phonons of Ge and 3 C-SiC. *Physical Review B*, 25:1151, 1982.

[145] A. Debernardi, C. Ulrich, M. Cardona, and K. Syassen. Pressure dependence of Raman linewidth in semiconductors. *Physica Status Solidi*, 223:213, 2001.

[146] N. R. C. Corsini, A. Greco, N. D. M. Hine, C. Molteni, and P.D. Haynes. Simulations of nanocrystals under pressure: combining electronic enthalpy and linear-scaling density-functional theory. *The Journal of Chemical Physics*, 139:084117, 2013.

[147] R. R. Lieten, K. Bustillo, T. Smets, E. Simoen, J. W. Ager, E. E. Haller, and J.-P. Locquet. Photoluminescence of bulk germanium. *Physical Review B*, 86(3):035204, 2012.

[148] S. Miyazaki, K. Sakamoto, K. Shiba, and M. Hirose. Photoluminescence from anodized and thermally oxidized porous germanium. *Thin Solid Films*, 255(12):99, 1995.

[149] L.A. Grunes. Study of the K edges of $3d$ transition metals in pure and oxide form by X-ray-absorption spectroscopy. *Physical Review B*, 27(4):2111, 1983.

[150] A. V. Sapelkin and S. C. Bayliss. Distance dependence of mean-square relative displacements in EXAFS. *Physical Review B*, 65:172104, 2002.

[151] A. J. Williamson, C. Bostedt, T. van Buuren, T. M. Willey, L. J. Terminello, G. Galli, and L. Pizzagalli. Probing the electronic density of states of germanium nanoparticles: A method for determining atomic structure. *Nano Letters*, 4:1041–1045, 2004.

[152] R.F. Pettifer and A.J. Bourdillon. Site-selective EXAFS via optical deexcitation. *Journal of Physics C*, 20:329–335, 1987.

[153] E. A. Stern. Number of relevant independent points in X-ray-absorption fine-structure spectra. *Physical Review B*, 48:9825–9827, 1993.

[154] I. T. Todorov, B. Smith, M. T. Dove, and K. Trachenko. Dl_POLY_3: new dimensions in molecular dynamics simulations *via* massive parallelism. *Journal of Materials Chemistry*, 16:1911–1918, 2006.

[155] J. Tersoff. Modeling solid-state chemistry: Interatomic potentials for multicomponent systems. *Physical Review B*, 39:5566–5568, 1989.

[156] F. W. Lyttle, D. F. Sayers, and E. A. Stern. Report of the international workshop on standards and criteria in X-ray absorption-spectroscopy. *Physica B*, 158:701, 1989.

[157] S. Tanuma, C. J. Powell, and D. R. Penn. Calculations of electron inelastic mean free paths. *Surface and Interface Analysis*, 36:1, 2004.

[158] N. F. Mott and E. A. Davis. *Electronic Processes in Non-Crystalline Materials*. Oxford University Press, 2012.

[159] A. Erbil, G. S. Cargill III, R. Frahm, and R. F. Boehme. Total-electron-yield current measurements for near-surface extended X-ray-absorption fine structure. *Physical Review B*, 37(5):2450, 1988.

[160] MATLAB. *version R2010a*. The MathWorks Inc., Natick, Massachusetts, 2014.

[161] B. Ravel. Ifeffit. http://bruceravel.github.io/demeter/, accessed March 2015.

[162] M Newville, P Līviņš, Y. Yacoby, J. J. Rehr, and E. A. Stern. Near-edge X-ray-absorption fine structure of Pb: A comparison of theory and experiment. *Physical Review B*, 47:14126, 1993.